
**ISAS - INTERNATIONAL SCHOOL FOR ADVANCED STUDIES**


# "Hot Spot" Model and Short Term X-ray Variability of Active Galactic Nuclei

Thesis submitted for the degree of

"Doctor Philosophiæ"


CANDIDATE

Bao Gang

SUPERVISORS

Prof. M. Abramowicz

Prof. A. Treves



October 1992

**TRIESTE**



**SISSA - SCUOLA INTERNAZIONALE SUPERIORE DI STUDI AVANZATI**

TRIESTE

Strada Costiera 11

# "Hot Spot" Model and Short Term X-ray Variability of Active Galactic Nuclei

Thesis submitted for the degree of

"Doctor Philosophiæ"


CANDIDATE

Bao Gang

SUPERVISORS

Prof. M. Abramowicz

Prof. A. Treves


October 1992

# Index

# Acknowledgements

My acknowledgements are due, in the first place, to all of my tutors in SISSA, whose teaching has made direct and indirect contribution to the present dissertation.

I am particularly grateful to Professor D. Sciama, the director of the SISSA Astrophysics sector, for his acceptance of me as a SISSA student, erecting an important signpost in my life that directs me into a new route of my academic career. I wish to express my sincere gratitude to Professor M. Abramowicz for having brought me to the understanding of the topic of "hot spot", and for having offered me constant and enlightening guidance and encouragement, particularly during the first two fundamental years of my study in SISSA. With his help, I succeeded in switching my field of research from 'Quantum Mechanics in Curved Space Time' to 'Variability of AGN', without too much effort. I am also greatly indebted to Professor A. Treves, one of my supervisors, particularly for exposing me, ignorant as I am, to the study of the observational data, for specifically introducing me to some of the approaches to data analysis which have directly enabled me to make initial progress in the area and for his strong support for my participation in the academic activities outside SISSA which undoubtedly have contributed greatly to my understanding of the subject.

I owe a separate debt of thanks to Dr A.Lanza, Dr X.H.Zhang, Dr V.Karas and Professor Z.Stuchlik for their collaboration with me in tackling specific issues

related to the basic properties of the "hot spot" model, to Dr. G.Tagliaferri, Dr L.Stella and Dr L.Ghiappetti for improving my knowledge of observational data, and to Professor G.C. Perola and Professor E. Massaro for their hospitality in Rome and for the exciting discussions.

Again, I would like to thank Professor M.Abramowicz, Professor A.Treves, Dr.A. Lanza for the insightful discussions in the course of writing the present dissertation and for having supplied valuable criticisms and detailed suggestions for improving the work. I am extremely grateful to Z.H. Han, my wife, Dr M.Smith, and Dr P.Haines for their careful reading and editing of the manuscript.

Finally, to the SISSA secretaries, particularly to A.Poretti and C. Parma, for having devoted their time and patience to the solution of my various problems, I offer my sincere thanks.

I assume full responsibility for possible errors of any sort in the dissertation.

# Introduction

A few years ago Professor M. Abramowicz initiated a new research project devoted to the short term X-ray variability of the active galactic nuclei. The new approach adopted in the project was based on the assumption that a significant part of observed variability should be directly influenced by the rotation of the accretion disk.

Accretion disks around black holes are the most serious possible explanation of the active galactic nuclei phenomenon, yet despite a lot of theoretical and observational efforts no direct proof of their existence has been found. It has been a traditional approach to prove the existence of accretion disks in active galactic nuclei by fitting the observed electromagnetic spectra (e.g. George, Nandra and Fabian 1990) and by fitting the shape of the observed emission line (e.g. Fabian, Rees, Stella and White, 1989) to those calculated from the theory. The new approach, however, fits the observed light curve and its variability power spectrum to the theoretical predictions. It is directed to the rotation of the central engine and based on the well understood (although in practice not easy to calculate) effects of light propagation in curved spacetime. The main underlying assumption is that the central part of an accretion disk cannot be smooth and steady. Instabilities (Wallinder *et al.*, 1992) and presence of vortices and magnetic flux tubes (Abramowicz *et al.*, 1992) make the inner region of accretion disks patchy and

noisy. The non axialysymmetric, non steady distribution of the surface brightness in the innermost region may be described as a distribution of some "hot spots".

When a spot moves on its orbit, the spot observed intensity is modulated by the Doppler effect and, when some conditions are met, by the gravitational lensing. The spot may be also eclipsed by the outer parts of the disk. Knowing the intrinsic luminosity of the spot, the radius of the orbit, the inclination of the disk with respect to the line of sight and the shape of the disk, one may calculate the theoretical, periodic, light curve. A distribution of many spots with different intrinsic intensities, sizes and lifetimes located at a range of radii gives aperiodic light curve. The variability timescale due to the orbital motion of the spots is related to the orbital periods. For an extreme Kerr black hole ($a = M$), the innermost stable orbit is at $r = M$ (units of $G = c = 1$ are used), thus the variability timescale could exist down to

$$T_K = 4\pi M = 6.3 \times 10^3 m_8 \qquad sec$$

where $m_8$ is the mass of the central black hole in the unit of $10^8 M_\odot$. For a Schwarzschild black hole ($a = 0$), the innermost stable orbit of a thin disk goes up to $6M$ corresponding to a period of

$$T_S = 3\sqrt{6} T_K .$$

According to the above formulae, active galactic nuclei with $10^6 \sim 10^9 M_\odot$ shows variability down to the timescale of minutes to hours.

It is quite natural to explain the observed power-law spectrum (in most of active galactic nuclei) and multi-peaked variability spectrum (say, NGC 6814) as due to the orbital motion of spots. The light curve of a single spot will produce a single line (or lines) in the variability power spectrum corresponding to the orbital

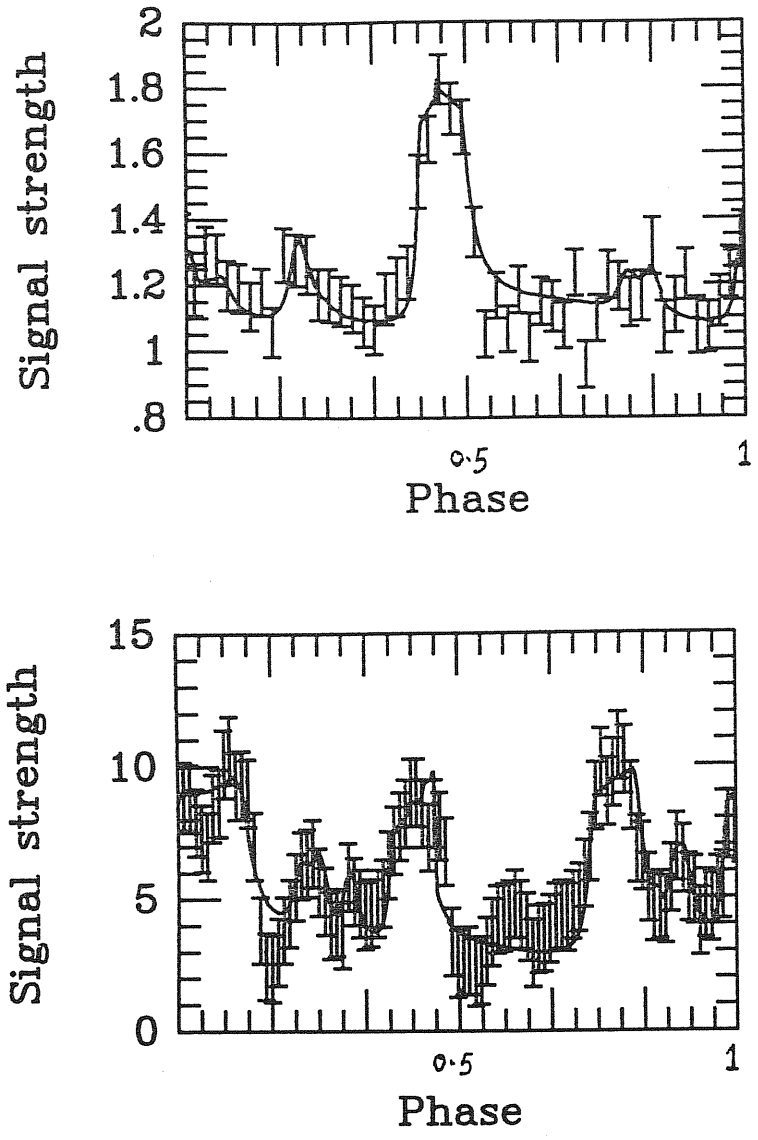


**Figure 1:** Fitting the theoretical light curve (broken lines) to those observed (points with error bars) for the Seyfert galaxy NGC 6814. The fit to EXOSAT data is shown in the upper panel, and to Ginga data in the lower panel. The $\chi^2$ test for the fits is very good, with $\chi^2 = 1.5$ for the EXOSAT fit, and $\chi^2 = 0.87$ for the Ginga fit.

frequency ( or its higher harmonics). Spots distributed at a large range of radii

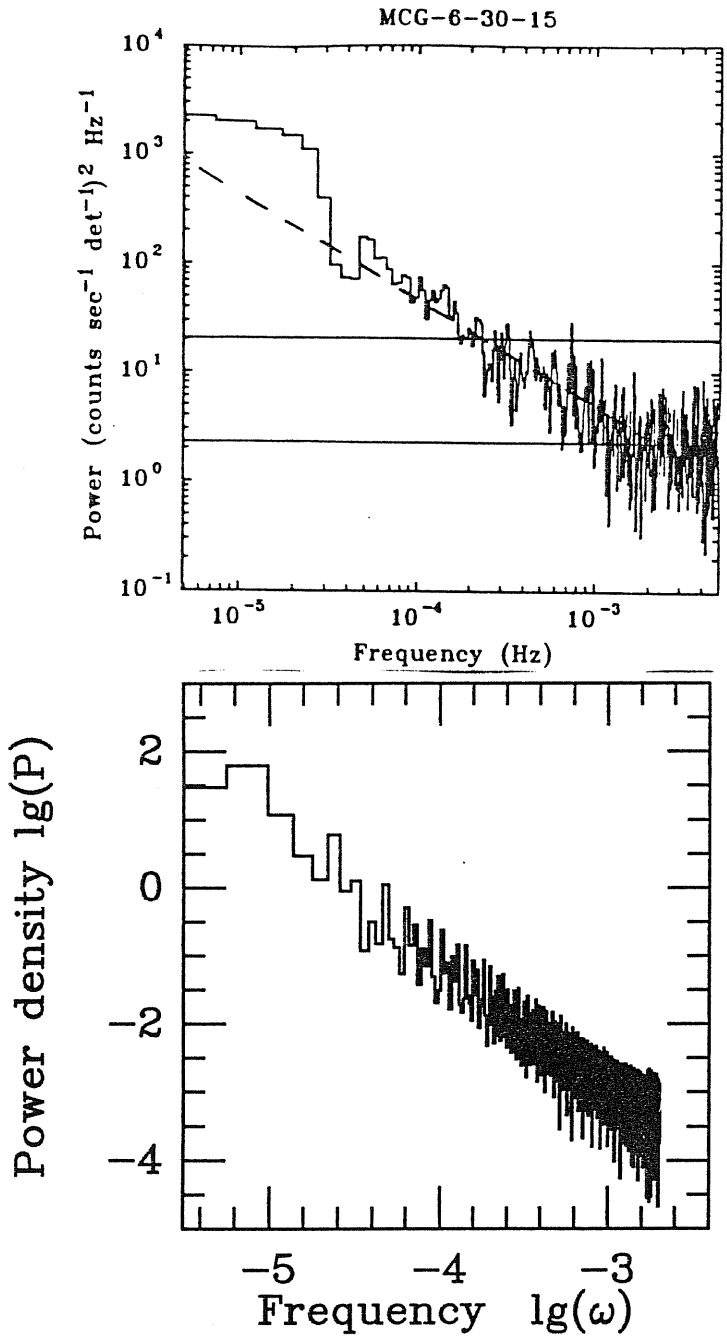


**Figure 2:** Featureless variability power spectra in the timescale ranging from $10^3$ sec to $10^5$ are characteristic of the majority of the active galactic nuclei. The upper panel shows variability power spectrum observed for the active galaxy MCG6-30-15, and the lower panel the variability power spectrum calculated with the use of my code.

produce many lines and overlaps to form a power law power spectrum. The slope of the variability power spectra depends on the statistics of spots, the inclination angle of the system, and the rotation law of the accretion disk. When a long life time spot (or spots) appears in a narrow range of an accretion disk, the light curve displays periodic flares. If the periodic flares are non-sinusoidal, the corresponding variability power spectrum will be multi-peaked with each peak being harmonically related to the other. The relative height of the peaks depends on the radius and the inclination angle of the orbit. Therefore, the comparison of the observed spectrum with that derived from the model supplies physical information on the central engine of active galactic nuclei.

As an important part of the project, I have been engaged in developing a practical (efficient and general) numerical code to calculate theoretical light curves in the whole range of relevant parameters and their variability power spectra with all the relativistic effects included, and in fitting the observed light curves and variability power spectra to the theoretic prediction of the model. The code has been used as the principal tool in all the work done so far on the subject by the project team. Figures 1 and 2 help to illustrate some of the possibilities of the code. Figure 1 shows the fit of the (Abramowicz, Bao, Fiore, Lanza, Massaro, Perola, Spiegel, Szuszkiewicz) "bright spot" model to the observed, periodic X-ray light curve of the Seyfert galaxy NGC 6814. Figure 2 is an example of theoretical simulation of the featureless variability power spectra, very typical for the active galactic nuclei.

Simultaneous to the production of the code, other related study has been carried out, for example, the behavior of photons emitted by a spot near a black hole, the gravitational lensing of the black hole. In the study of the gravitational lens-

ing, a special analytic method is developed for calculating the impact parameter of photons emitted by a spot at various positions on the disk. Such effects as the geometry of the disk and disk self-eclipse are considered. Variability power spectra in various situations, e.g with/without eclipse, spots distributed in a narrow/wide range etc, have also been examined. Consonant with the study of the variability of active galactic nuclei, some data analyses have also been performed. The analyses are preliminary, concentrating only on the cross correlation of the variability in different energy bands.

This dissertation presents a quantitative study of the "hot spot" model, making a focus on examining how the X-ray photons behave when emitted by a single spot moving around a black hole and how the orbital motion of the spots introduces apparent variabilities in the X-ray light curve. Such a study is founded on the assumption that the central black hole is a Schwarzschild black hole. The results due to this assumption are similar to those due to rotating black hole when only direct images of photons (photons do not cross the equatorial plane) are considered. In the study of the variability power spectrum, the classical treatment (vs. fully relativistic treatment) is sometimes necessary. This is because the approximation is reasonable for small inclination angles, and what is more important, can provide us with a direct knowledge of the structure of the variability power spectrum.

The dissertation is thus organized: Chapter I briefly reviews and discusses the observational data; Chapter II examines the general relativistic effects due to one spot moving around a black hole, with different geometry of the disks considered; Chapter III presents a detailed study of the variability power spectrum from spots; Chapter IV describes a quantitative model for NGC 6814 and gives a comparison

of different related models; and Chapter V shows some of the data analyses and concludes the whole dissertation with a general discussion of the afore-mentioned issues.

The research on variability of active galactic nuclei is far from being exhaustive. Experts are divided over the importance of basic observational facts and their theoretical interpretations. The ideas expounded in the present dissertation do not pretend to solve the problem, or they may be later proved to be inconsistent with the new observational data. In any case, they can be taken as a point of departure to further research on the physical conditions deep in the central engine of active galactic nuclei.

# Chapter 1

# Short Term X-ray Time Variability Of AGN

The X-ray variability of AGN, especially the short term (minutes to days) variability, is expected to provide information on the central region of the accretion disk, such as the accretion mechanism, the efficiency of the energy emission and the mass of the central black hole.

A number of deductions may be drawn from variability observation. The shortest X-ray variability timescale is believed to associate with the size of the emission region. For a simple isotropic model where the X-rays are emitted around a black hole, the intrinsic variability timescale is expected to be greater than the light travel time across a distance equal to the Schwarzschild radius of a black hole (Elliot and Shapiro 1974)

$$\Delta t_{min} > \frac{2GM}{c^3} \sim 1000 M_8 sec,$$

where $M_8$ is the black hole mass in unit of $10^8$ solar masses. This crossing time scales with the mass of the central black hole. One therefore expects that large central black hole mass exhibit large intrinsic variability timescale and small black hole show small intrinsic variability timescale. The variability timescale may also shed light on the efficiency $\eta$ with which mass is converted to energy. If a spherically symmetric, homogenous cloud of stationary matter is converted into radiation

with efficiency $\eta$ the shortest intrinsic timescale for the conversion occurs when the optical depth of the cloud is unity (Cavallo and Rees 1978, Fabian 1979). This relation is given as

$$\eta \geq \frac{5\Delta L_{43}}{\Delta t},$$

where $\Delta L_{43}$ is the change of the luminosity in unit of $10^{43}$ erg $s^{-1}$. It is the total luminosity that changes in the time interval $\Delta t$. The 2–10 KeV is thus an underestimate by a factor of perhaps 10 or more (McHardy 1989). Values of $\eta$ larger than 10% require non-isotropic or rotating models, or some degree of relativistic beaming. Simple isotropic models only allow for $\eta$ smaller than 10%.

Moreover, the X-ray variability pattern, e.g. the periodic flares, the dips in the light curves due to the orbital motion of the accreting matter, may offer insights into the geometry of the system and the mass of the central black hole. If we assume a Keplerian disk, the mass is

$$M_8 \sim 1.1 \times 10^{-4} P_o R^{-\frac{3}{2}},$$

where $P_o$ is the period of the observed periodic flares/dips, $R$ is the the orbit radius of the object which causes the periodic flares/dips in unit of Schwarzschild radius, and M is in unit of $10^8 M_\odot$.

## 1.1 A brief description of long timescale (months–years) variability

One of the best examples of long time variability is the object B21218+305 (Wilson et al. 1979), which shows long term variability in its light curve spanning four years as well as some possible outbursts. The X-ray outburst took place at the beginning of 1974 and the optical one a hundred days later.

The object Cen A in the radio galaxy is another good example (e.g. Lawrence, Pye, Elvis 1977; Terrell 1984). This low-luminosity X-ray source ($L_{2-10KeV} \sim 5 \times 10^{41}$ erg sec$^{-1}$ in its low state ) increased in its brightness by a factor of more than five from 1970 – 1973 and returned to a low state by 1977 where it remained until 1979 when it again brightened by $\sim$ factor of five. Superimposed on these gradual variations were more rapid variations with the timescale of $\sim$ 10 days.

In order to find a typical long timescale, McHardy (1989), Roberto and McHardy (1989) investigated variability power spectra of NGC 5506, NGC 4151 at low frequency, trying to find a characteristic timescale, in analogy with the low frequency roll–over observed in the X-ray variability power spectrum in galactic black hole candidate Cyg X-1. For NGC 4151, they constructed long timescale medium energy light curves (spanning $\sim$ 10 years), using data primarily from EXOSAT, Einstein HEAO-1 and Ariel V. They argued that in addition to the high frequency roll-over in AGNs' power spectra which avoid divergence of variability power, there should exist another roll-over (flattening) at low frequency end. This low-frequency roll-over may well correspond to some sort of viscous timescale, which indicates very little about the central black hole, yet something about the physics of the surrounding accretion disk. They found that the power spectrum of NGC 4151 is similar to $\frac{1}{f}$ on long timescales, and that $\frac{1}{f^2}$ noise best describes the short timescale variability. However, they did not see the sharp turn-over observed in Cyg X-1. For the power spectrum of NGC 5506 they found a steady flattening off towards lower frequencies. Possibly the 'knee' frequency is near few$\times 10^{-7}$Hz.

It seems that the long timescale variability is not directly related to any fundamental parameters associated with the central black hole, such as the mass. It might be associated with the change of fueling rate, which could be attributed

to the instabilities in the cooling flow.

## 1.2 Short timescale (minutes–days) variability

Prior to the launch of the EXOSAT, the low sensitivity of the X-ray detectors and short continuous observation afforded by the low-earth-orbit satellites had given a rather poor picture of X-ray variability of AGN in its short trend. X-ray variability of AGN on timescales less than $\sim$ 12 hrs was generally thought to be rare. The results of the first large and systematic HEAO-1 A2 study of some 38 AGNs were summarized by Tennant and Mushotzky (1983). Only one of the 38 AGNs, NGC 6814, shows rapid variability with timescale smaller than one hour. However, the realization that rapid variability was not so rare had led to the allocation of several long continuous EXOSAT observations. Gradually encouraging signs turned up.

The first clear example of rapid X-ray variability from EXOSAT observation was the low luminosity Seyfert NGC 4051 (Lawrence et al. 1985). During the 8.5 hour observation a large amplitude variability on timescale of $\leq$ 1 hour was detected, which confirmed as well as considerably extended a similar result from one of the five Einstein Observatory IPC observations that found a doubling timescale of 2000s (Marshall et al 1983). This was the second well-documented example of rapid variability at the time. The first one had been the low luminosity Seyfert galaxy NGC 6814 where rapid variability with timescale $\sim$ 100 sec was found by HEAO-1 (Tennant et al 1981). In the later operation, EXOSAT performed a number of long looks at AGNs, e.g. NGC 6-30-15 ( Pounds and Turner 1987), NGC 4151 (Pounds et al, 1986, Perola et al, 1986), NGC 6814 (Branduardi–Raymount

and Mittaz 1989, Fiore et al, 1992), which updates our view of the short term variability.

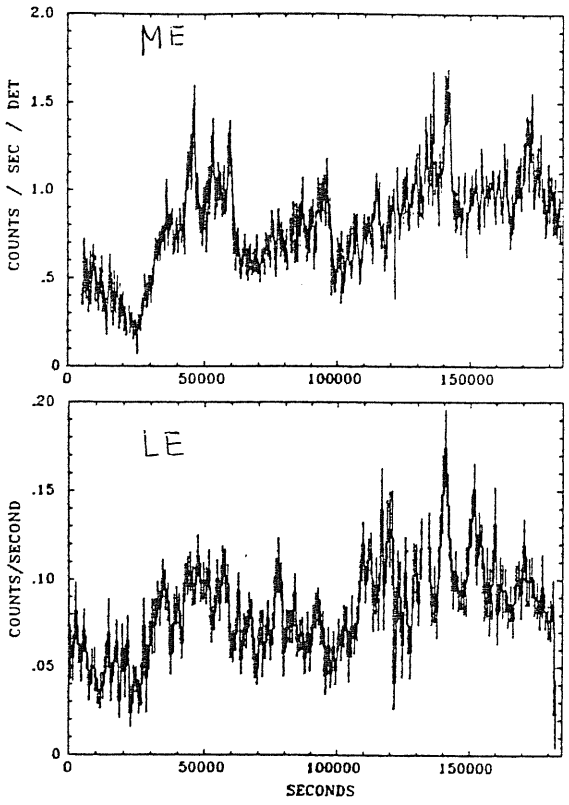


**Figure 1.1** Background subtracted ME and LE light curves of MCG-6-30-15 during 29-31 January 1986 (taken from Pounds and Turner, 1986).

### 1.2.1 The variability patterns

The X-ray variability of the light curve sees a great variety. Some sources show rapid variability with large amplitude, such as NGC 4051, MCG 6-30-15, while others vary with small amplitude, e.g. NGC 4151. There are still other special

sources, for example, the low luminosity QSO III ZW2. In the ME observation of November, 1985, a large flare was seen: after $\sim$ 4000$s$ observation the ME flux of III ZW2 began to rise and increased by a factor of 3 in about 1500 s and then reached a relatively quiet level, where it remained for the rest of $\sim$ 18000 sec observation (Pounds and Turner 1986). The scope of the present dissertation, however, confines us to a description of a few representative cases.

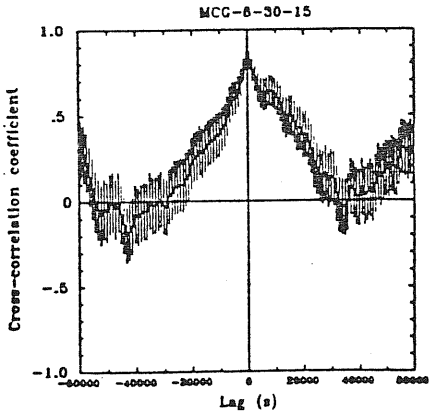


**Figure 1.2** The cross correlation function of ME/LE light curves of MGC-6-30-15 for the observation 1986 (taken from Pounds and Turner, 1986).

One of the best detections of variability of AGN is MCG-6-30-15, a typical Seyfert galaxy with moderate luminosity $L_{2-10KeV} \sim 10^{43}$ erg s$^{-1}$. A relatively

short (9 hr) EXOSAT observation in July 1984 revealed continuous variability, well-correlated in both ME and LE detectors on a timescale down to one hour ( Pound, Turner and Warwick 1986). The source was pointed at again by EXOSAT in January 1986 for over two days, and was bright again and strongly variable (Pounds and Turner 1986). Figure 1.1 shows the ME (2-6kev) and LE (0.15-1.5kev) light curves of this observation with the background subtracted.

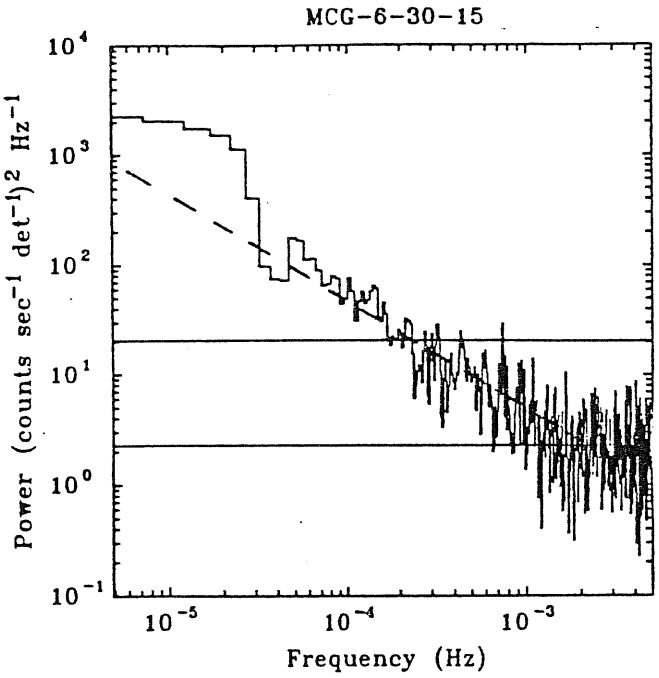


**Figure 1.3** Power spectrum of 2-6kev light curve of MCG -6-30-15. The dashed line is for $f^{-1}$ and the horizontal lines for power levels of white noise and this plus $5\sigma$ (taken from Pounds and Turner, 1986).

Two particular strong flares were seen with $9 \times 10^4 s$ apart. A close exam-

ination has shown factor-of-two changes in $< 1000s$. Figure 1.1b displays the independent LE lightcurve whose visual comparison with Figure 1.1a shows a strong but less than perfect correlation. Fig 1.2 is the cross-correlation function of ME/LE light curves for the observation in 1986.

No delay between variations of hard and soft X-rays are found. Figure 1.3 is the variability power spectrum of MCG 6-30-15 for the observation 1986. The power spectrum is well-fitted by a *power-law* with a slope about $-1$ representing this kind of variability.

Another good example is the low luminosity ($\sim 10^{41}$ erg $s^{-1}$) Seyfert galaxy NGC 4051 (Lawrence et al 1985, McHardy 1985, Lawrence 1986). Fig. 1.4 shows the EXOSAT LE light curve and its variability power spectrum. The observation was performed on December 3, 1985 and lasted about 62 hr. The eyes can easily pick out the large amplitude flares. The corresponding variability power spectrum has a slope $-1$ which reflects this kind of variation. The ME light curve of this observation is highly correlated with LE light curve and shows no noticeable lag (Lawrence 1986). Another relatively short (8.5 hr) observation (Lawrence 1985) in April 1984 also shows large amplitude variation. 4 *regular flares* are clearly visible in its LE light curve with a timescale of $\sim$ 4000 s (McHardy 1985). Cross correlation of ME and LE light curves reveals a strong correlation with no lag ($<$ 200sec) between ME and LE fluxes, but the LE flux varies more than the ME flux.

Unlike MCG 6-30-15 and NGC 4051, NGC 4151, a famous Seyfert galaxy with luminosity similar to MCG 6-30-15, shows a remarkably different behaviour.

Figure 1.5 illustrates two of the longest EXOSAT observations in which the most evident variability is slow trended, upward or downward, superimposed with

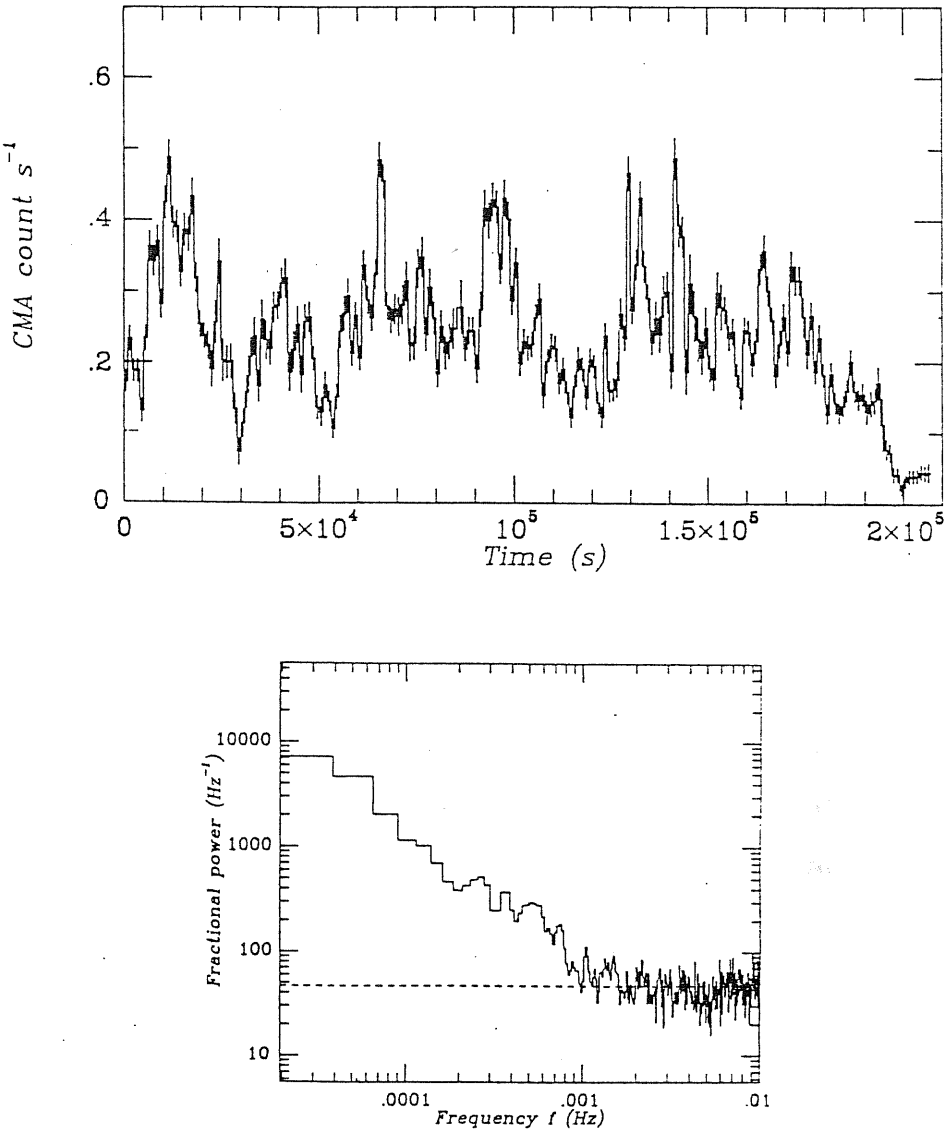


**Figure 1.4** The EXOSAT LE light curve of NGC 4051 of observation December 1985 and its variability power spectrum (taken from McHardy 1989).

small amplitude rapid variation (Perola, et al 1986). Its power spectrum (Figure 1.6) exhibits this character. It is of the slope of -2 and has little power with

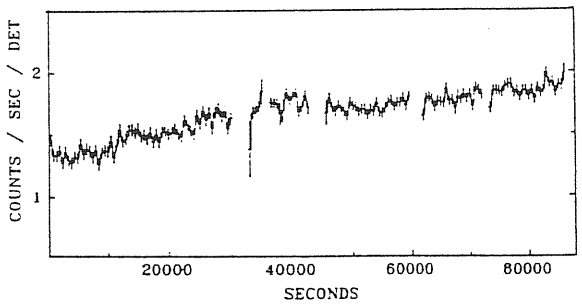


**Figure 1.5** Background subtracted of 2-6kev light curve of NGC 4151 during July, 1983 (taken form Pounds and Turner, 1986)

frequencies higher than $f\ 10^{-4}$ Hz. The "sluggish" behaviour is intrinsic to the source. A number of AGNs have shown this behaviour, for example, NGC4593 (Barr et al 1986), 3C273 (Mchardy 1989).

In addition, some sources exhibit periodic flares in their X-ray light curves. Take the low luminosity Seyfert galaxy NGC 6814 (Mittaz and Branduardi-Raymont 1989, Fiore, Massaro and Barone 1992) as an example. Quasi-periodic flares with a period $\sim$ 12000 sec are visible in the ME light curve. Various models of analysis (Autocorrelation function, power spectra, fractals,folded light curve,

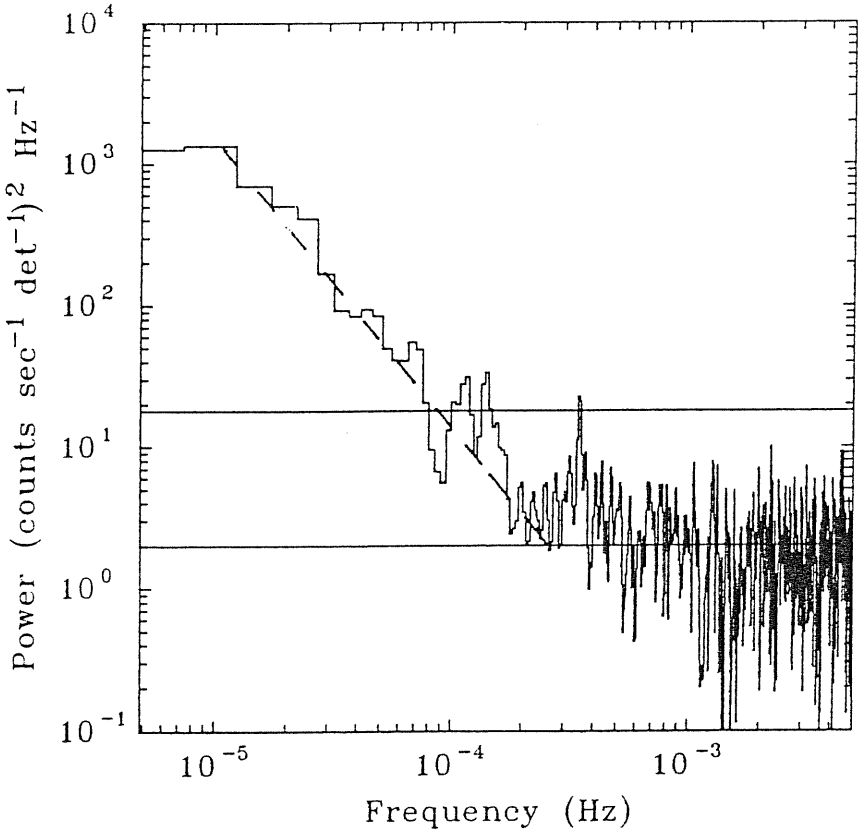


**Figure 1.6** The power spectrum of 1983 observation of NGC 4151. The dashed line is for $f^{-2}$ slope (taken from Pounds and Turner 1986)

etc.) and different observations by different satellites, i.e. EXOSAT and Ginga, all pick out a $\sim$ 12000 second quasi periodicity. This behavior is believed to be intrinsic to the source. The variability power spectrum of the source has two components: the power-law component due to the chaotic variation of the source and the multi-peaked component due to the periodic flares. Another example is NGC4151 which shows small–amplitude coherent signal in its X-ray emission at frequency $7.9 \times 10^{-5}$Hz (corresponds to the period 12600 s) (Fiore, et. al, 1989).

Since the discovery of characteristic timescales, which might be linked with

some important parameters of AGN, enables the determining of the black hole mass, the periodicity observation becomes extremely important. The variability of this type will be discussed in detail in chapter 4 where a quantitative model for NGC 6814 is presented.

### 1.2.2 The variability power spectrum

Examining the variability power spectra of AGN, we find that in most cases, the power spectra of short timescale of AGNs can be well-fitted by a power-law, i.e. $\mathrm{p}(\omega) \sim \omega^{-\beta}$, with power index ranging from 1 to 2 from frequency $10^{-5}$–$10^{-3}$ Hz (Pounds and McHardy 1988). This suggests that there is no preferred timescale. The variability is self similar, namely, it occurs scale-invariantly. If we fit the power spectrum at high frequency $10^{-4}$–$10^{-3}$, the power spectrum of AGN will be steeper than $-1$ ( McHardy 1989), which indicates that the integrated power converges. Up to now, none of the power spectra shows evidence of very rapid steepening at the highest observable frequency, down to a timescale of 300 sec where the noise is dominant (Done et al 1992). This implies that there is no "fastest variability" timescale detected to date. Some sources maintain the same slope to the low frequencies, while others gradually flatten in the observed frequency range.

Note that even for the same source, different observations at different times sometimes give a different power spectrum slope. For example, the two observations of NGC 4593 by EXOSAT showed that the source varied more rapidly when it was weak (flatter-sloped) in the observation of 1985 than in the observation of 1986 when it was bright (steep-sloped)(Barr et al 1986).

An exception of the power law class is NGC 6814 in which one of the compo-

nents of variability power spectrum is characterised by a number of harmonically related peaks. Table 1 shows the power index $\beta$ and the variability amplitude taken from McHardy (1989) for several sources.

Table 1. ME power Spectral Slopes and the variability amplitude

| Source | Power spectra slope | Variability amplitude |
|---|---|---|
| NGC6814 | -1.0 | 6.6 |
| NGC5506 | -1.0 | |
| NGC6-30-15 | -1.0 | 6.8 |
| Mkn335 | -1.0 | 5.0 |
| NGC4051 | -1.0 | 9.1 |
| Mkn766 | -1.5 | |
| NGC4151 | -2.0 | 1.6 |
| NGC4593 | -2.0 | 2.1 |

* The empty space means that the amplitude is not given.

### 1.2.3 Correlations of the variability amplitude and the luminosity

It is found that for Seyfert galaxies, the two-folding timescale (i.e., the time for the source intensity to change by a factor of two) correlates strongly with the luminosity, that is, the more luminous the sources are, the more slowly they vary (Barr, Mushotzky 1986, Bassani et al 1983). This has been verified by McHardy et

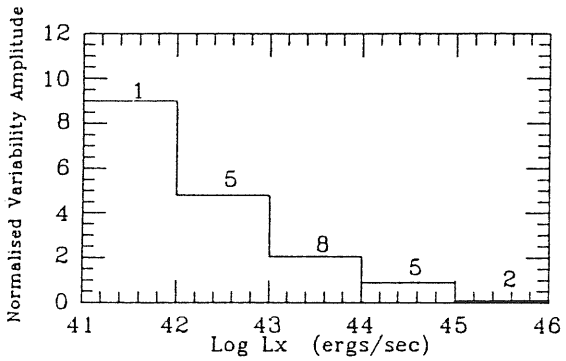


**Figure 1.7** The average normalized variability amplitude at $10^{-4}Hz$ plotted as a function of 2-10 kev luminosity. Note that the average normalized variability amplitude in the range $10^{45} - 10^{46}$ erg sec$^{-1}$ is zero (taken from McHardy, 1989).

al (1989). Since "long looks" have been performed only on a small number of well-known bright AGNs, McHardy et al defined the power spectrum normalization as the variability amplitude at $2 \times 10^{-4}$ which corresponds to the typical length ME observation of EXOSAT. The variability amplitude is simply the root of the power spectrum at $2 \times 10^{-4}$ Hz then normalized by dividing the average ME count rate. Fig. 1.7 shows how the normalized variability amplitude correlates with the luminosity. Note that IIIZW2 is an exception. It is bright enough ($L_x \sim 10^{45}$ erg

$s^{-1}$), but has a large variability amplitude.

### 1.2.4 The correlated variability of hard and soft X-rays

The long and relatively continuous observations and wide energy range 0.05 – 10 KeV) make the EXOSAT data particularly suitable for the search of lags between the hard and soft X-ray variations.

In some sources, the EXOSAT ME and LE light curves show substantial correlation, while in others, the variation is sometimes strong in one band and only marginary in the other.

In a small number of sources, the LE count rates are high enough to allow calculation of cross-correlation function of ME/LE lightcurve, e.g. MCG6-30-15 ( Pounds and Turner 1985), NGC 4051 (Lawrence et al.1985), NGC4593 (Barr et al,1987), NGC 5548 (Kaastra and Barr 1889) and PKS 2155-304 (Tagliaferri et al 1991). In the analysis of NGC4593 and NGC5548 a delay of hard X-ray for several thousands sec was found, but the result awaits further confirmation, since some spurious effects in the cross correlation analysis could be caused by the systematic uncertainties of the ME detector of EXOSAT (Tagliaferri et al 1991, see also chapter 5).

## 1.3 Variability of galactic X-ray sources

The X-ray variability of galactic X-ray sources is not the major concern of the present dissertation, nevertheless, it merits our attention because of the resemblance of the sources to AGN.

Fig. 1.8 and Fig. 1.9 illustrate the variability power spectra for galactic X-ray sources Cyg X-1 and LMXB Gx 339-4. They are similar to those of AGNs in that their power spectra are in the shape of power-law.

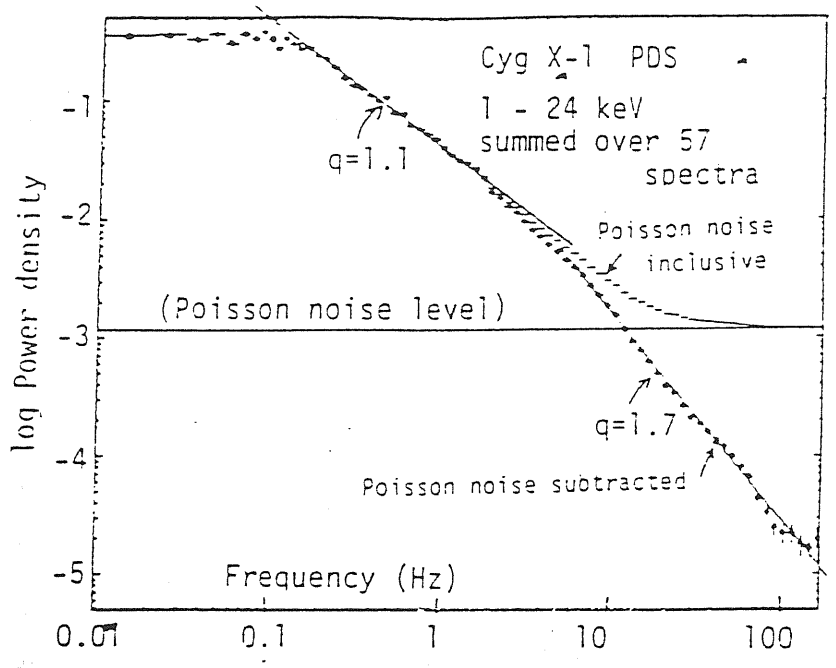


**Figure 1.8** The X-ray variability power spectrum of Cyg X-1 (taken from Makishima 1989)

A"knee" frequency is seen in the power spectrum of galactic black hole candidate Cyg X-1 (Nolan et al 1981), and the knee point is about 0.1 Hz which corresponds to a timescale much larger than the light travel time associated with a black hole of several solar masses (< millisecond). Nolan et al (1983) suggested that the knee frequency may be related to clumps in the accreting material which

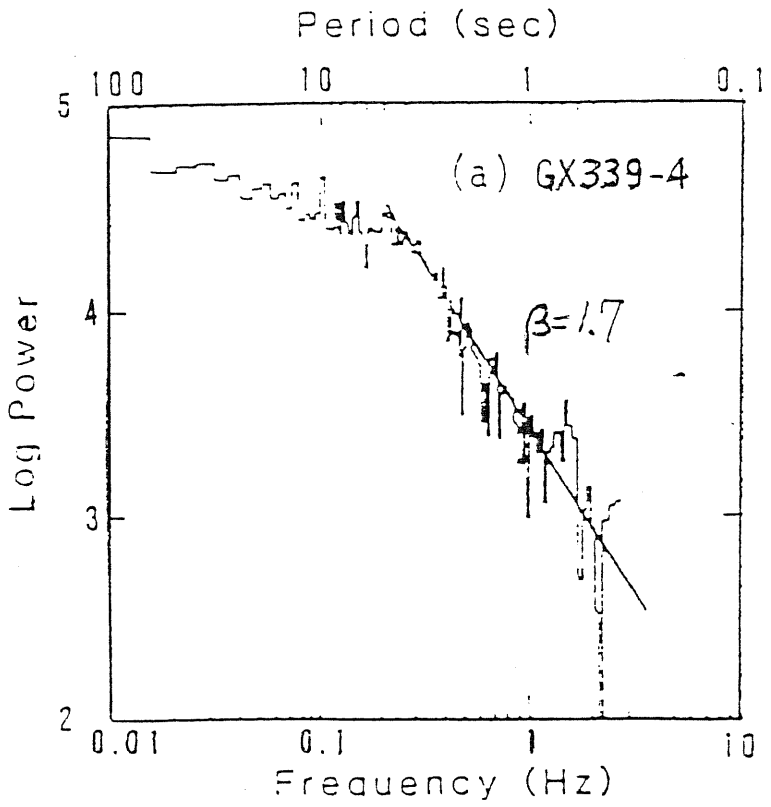


**Figure 1.9** The X-ray variability power spectrum of Gx 339-4 (taken from Makishima 1989)

are produced by the instabilities of the accretion disk, and that the disk is unstable only inside a certain radius.

The self-similar variation has also been observed in some other galactic X-ray sources. Power spectra for several LMXBs observed with Tenma and Ginga together with EXOSAT measurements of many LMXBs are in the range of $1 < \beta < 2$. Typically, $\beta$ takes the value of $1.4 - 1.5$ in the frequency range of $0.1 -$ a few $\times$10Hz. Fig. 1.10 sums up the power spectra slope measurement of Tenma and Ginga.

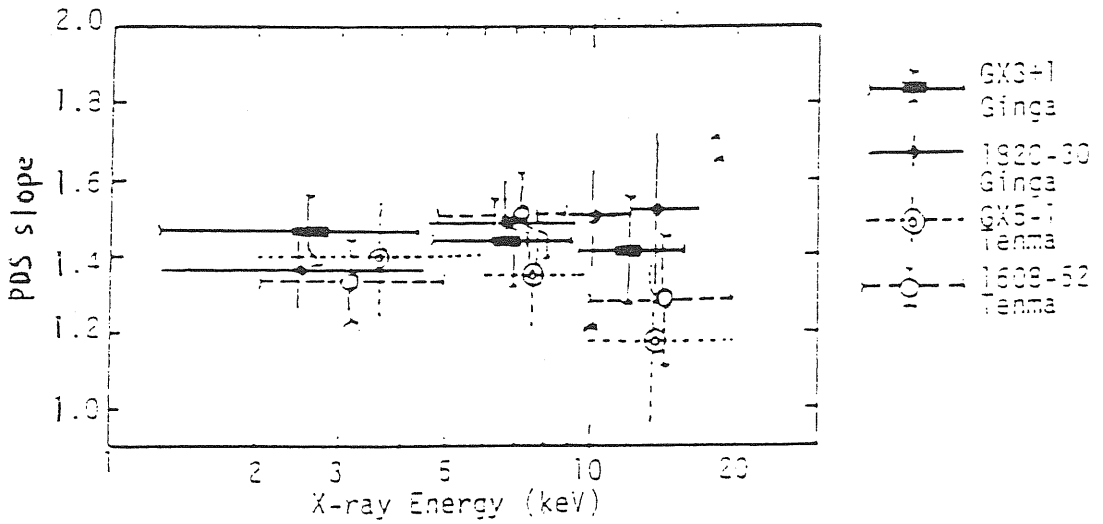


**Figure 1.10** Values of power spectrum slope $\beta$ measured with Tenma and Ginga, plotted against X-ray photon energy (taken from Makishima 1989).

Unlike Cyg X-1, the power spectrum of LMXB does not show noticeable low frequency flattening at least down to a few mHz. However, the flattening should eventually take place at some low frequencies, as their integrated power would otherwise diverge. Results from long uninterrupted EXOSAT observation suggest that flattening occurs at $< 1$ mHz. If so, the knee point frequency for LMXBs is at least two orders of magnitude longer than that of Cyg X-1, GX339-4 and X0331+53. However, this difference is still not clear. Above a few Hz, the self-similar behavior of LMXB often ends up with quasi-periodic oscillations (QPO)

at 5 – 30 Hz (Makishima 1989).

## 1.4 Discussion

Like the energy spectrum, the study of variability power spectrum should be taken seriously. It involves the searching of characteristic timescales and may reveal certain intrinsic properties of the central engine, e.g. the emissivity of the disk, the inclination of the system.

No doubt that the self-similar variability pattern may provide valuable information on AGN. Although we are still unable to derive any well–defined variability timescales, yet from the variability power spectrum slope, we may gain insights into some essential properties of the source. The fact that the variability power spectra of AGN have different slopes instead of one constant suggests that the physical and geometry conditions of the sources are different.

At this point, it should be quite interesting to discuss different variability patterns mentioned in the last section. All the patterns of the X-ray flux are basically chaotic, which implies that the X-ray emission region is far from smooth, instead, it is asymmetric and contains numerous small " clumps". The chaotic variability can be attributed to the discrete properties of the accreting matter resulting from the instability. For the variability characterized by flares, Pounds and Turner (1986) in the discussion of the observed flares in MCG 6-30-15 indicated that the short term flares in the light curve may be "associated with clumps of accreting/radiating material, moving chaotically around the central hole and being periodically Doppler boosted....". We should add, however, another important effect to this picture: the radiating material may be also periodically lensed by

the black hole. The difference between the periodic and non-periodic flares could reside in the lifetime of the radiating matter. Long lifetime clumps may flare many orbits and the flux therefore shows periodic flares, whereas short lifetime clumps may flare once or twice before their extinction, constantly followed by the birth of new clumps. Why do the variability patterns of AGN show both small amplitude and large amplitude ? One possible explanation is that the electrons scattering in an extended atmosphere around the nuclei could wash out the rapid variability in X-ray variation (McHardy 1989). The inclination angle may also channel an answer(Pounds and Turner 1986). It is obvious that, as long as the geometry of the system is not face-on, the non-axisymmetric feature will be amplified by the Doppler and lensing effects if the disk rotates around the black hole. This is to suggest that for a large inclination we expect to observe large fluctuation in the light curve. The inclination angle in this sense is a "magnifier" that amplifies the fluctuation ( through the Doppler effect and lensing effects).The "magnifying effect" is always unidirectional, that is, it never reduces the amplitude of the fluctuation. Nonetheless, we can not thus jump to the conclusion that the light curve with small variability amplitude always has a face-on geometry. This is because the "magnifying effect" is amenable to the degree of the asymmetry of the sources. For symmetric sources even with a large inclination, we cannot perceive the "magnifying effect".

A strong correlation is found between the X-ray luminosity and its variability amplitude. When the source is brighter, its variability amplitude is smaller, and vice versa for a faint object. A traditional explanation is that smaller objects ( and also presumably less luminous) take less time to vary than large ones. But it should be also born in mind that some of the variations have hardly any connection with

the central sources. For example, a shock in the relativistic beam does not tell us much about the sources. In fact, the "magnifying effect" yields more information about the inclination of the system than about the central mass. If we admit that the system of face-on geometry looks brighter (when the system is optically thick), we expect the variability amplitude of the flux in this situation to be small ( the Doppler and lensing effects are minimized). This is to suggest that the inclination angle of the inner system plays an essential role in the observed variability.

The variability of galactic X-ray sources exemplifies great similarities to AGN in the aspect of variability power spectrum. This should be apparent when one realizes that the corresponding timescales must differ by a factor of $\sim 10^8$ because of the mass difference, which indicates that both AGN and galactic sources have a very similar physical mechanism of variability.

A theoretical model of AGN to explain the observed variability must at least incorporate the parameters of disk geometry, for instance, the inclination of the disk, which could be crucial for generating variability patterns.

The short term correlated soft and hard X-ray variability places very strong constraints on the emission region and geometry configuration of AGNs, which has not been well-defined yet.

If the hard ($2-10$ KeV) and soft (below 2 KeV) X-rays are two different components, then the finding of any delay between the hard and soft X-ray variations will back up the model within which soft seed photons are supposed to scatter around by the hot corona above or below the accretion disk, with a result in ME lag relative to LE. Otherwise, the "clumpy" disk model could be more plausible, i.e. the X-ray emitting medium may be embedded inside the magnetically confined blobs of dense and cool gas (Fabian and George 1991, Clavel et al 1992).

Both the finding of the correlated variations (not 100% prefect) and that of no obvious delay between the soft and hard X-rays in a number of AGNs, e.g., MCG 6-30-15, NGC 4051 (lawrence 1986), indicate that the two components of X-ray undergo an interactive process and that the primary X-ray source is extremely close to the disk. In this sense, the "clumpy" disk may be more realistic.

## 1.5 Conclusion

- Chaotic light curve suggests that there exist many small "clumps" on the surface of the accretion disk.
- Relativistic effects such as the Doppler effect and the gravitational lensing may be responsible for the observed flares displayed in the light curves of some AGNs.
- It might be the inclination angle of AGN that underlies different variability patterns.
- The presence of similar variability in AGN and galactic X-ray sources implies that the two kinds of sources might share the same variability mechanism.

# Chapter 2

# The Relativistic Effects of a Corotating Spot in Accretion Disks

## 2.1 Introduction

As previously mentioned, the X-ray producing region (the inner part of accretion disk), is subject to thermal and viscous instabilities (Shakura and Sunyaev 1976 ; Lightman and Eardley 1974; Lightman 1974; Pringle et al. 1973, see Treves,et al 1988 for a review). The perturbations will grow fast enough to destroy the stationary, axisymmetric state which is generally assumed, although they are subsequently saturated to give a stable state. Under typical conditions, the inner part of an accretion disk resemble a collection of clumps, orbiting around a central black hole. Many observed phenomena may be accounted for in terms of a "clumpy" disk. Fabian and George (1990) suggest that the primary X-ray sources may be carried by clumps in accretion disks which could explain why small lags or no lags are seen between the X-ray continuum and iron line variations in NGC 6814, and small lags between variations of hard and soft X-rays in a number of

AGNs.

Because of the huge local shear of the orbital motion, any relatively large clump produced by instabilities will be smeared out very quickly or may even be prevented from growing to a large scale, and only small ones can exist for a relatively long time. However, even the latter will be destroyed on a long thermal timescale (Pringle 1981). Apart from the clumps, we also have other types of local non-uniform objects like magnetic flares, shocks or convective cell, in this part of the accretion disk. Due to the lack of theoretical modeling of temporal and spatial evolution of the inner regions of the accretion disk, it seems reasonable to adopt a phenomenological approach at the present stage. Instead of introducing another model for this non-stationary, non-axisymmetric property of the disk, we approximate the non-uniform feature of the inner part of the accretion disk as a group of independent spots distributed on the surface of the accretion disk and corotating with the disk, with certain prescribed distribution function such as lifetime $\tau$, brightness $I_o$ and surface number density, all of which are a function of radius. When a spot orbits a central black hole, three effects will modulate the X-ray intensity emitted by the spot:

(I) Doppler effect due to the relativistic motion of the spot;

(II) Gravitational lensing due to the strong gravitational field around the black hole;

(III) Occultation due to the thicker part of the disk.

These effects will introduce periodicities corresponding to the orbital periods of the spots and produce apparent variability in the X-ray intensity. Thus although the behavior of a spot itself is very essential to interpreting the short term X-ray variability of AGN and galactic X-ray sources (Lehto 1990; Begeman 1990), the

orbital motion should also be included in the study of the variability.

Since X-rays come from the the region very close to the black hole, the gravitational effect could be important in understanding the observed X-ray variability. The discovery of a black hole, on the other hand, would rely very much on the influence of its gravitational field on the surrounding matter or the emission behavior of the matter. In this chapter, we investigate the gravitational effect of a single spot corotating with a disk around a black hole ( a similar consideration with a charged black hole is presented in Appendix B). The disk geometry is considered, although it is not well defined yet. Once a good knowledge of the behavior of a single spot is gained, the collective behavior can be obtained through summation of all spots. The spot in question can be a vortex (Abramowicz et al 1992), a star, or a black hole (Syer, Clarke and Rees 1991) or something else.

## 2.2 A spot rotating around a Schwarzschild black hole

In this section, we take advantage of the spherical symmetry of a Schwarzschild black hole, using the simple geometry and geodesic equations to find the impact parameters of photons emitted by the spot and therefore the observed flux from a spot.

### 2.2.1 The model

Let us consider a small spot with a finite size which moves around a Schwarzschild black hole. The gravitational effect of the surrounding matter can be neglected in comparison with the black hole. We shall treat the spot as a tiny sphere radiating

isotropically in its own rest frame. The accretion disk is so thin that it can be considered to be lying in the equatorial plane of the Schwarzschild black hole, as in Figure 2.1.

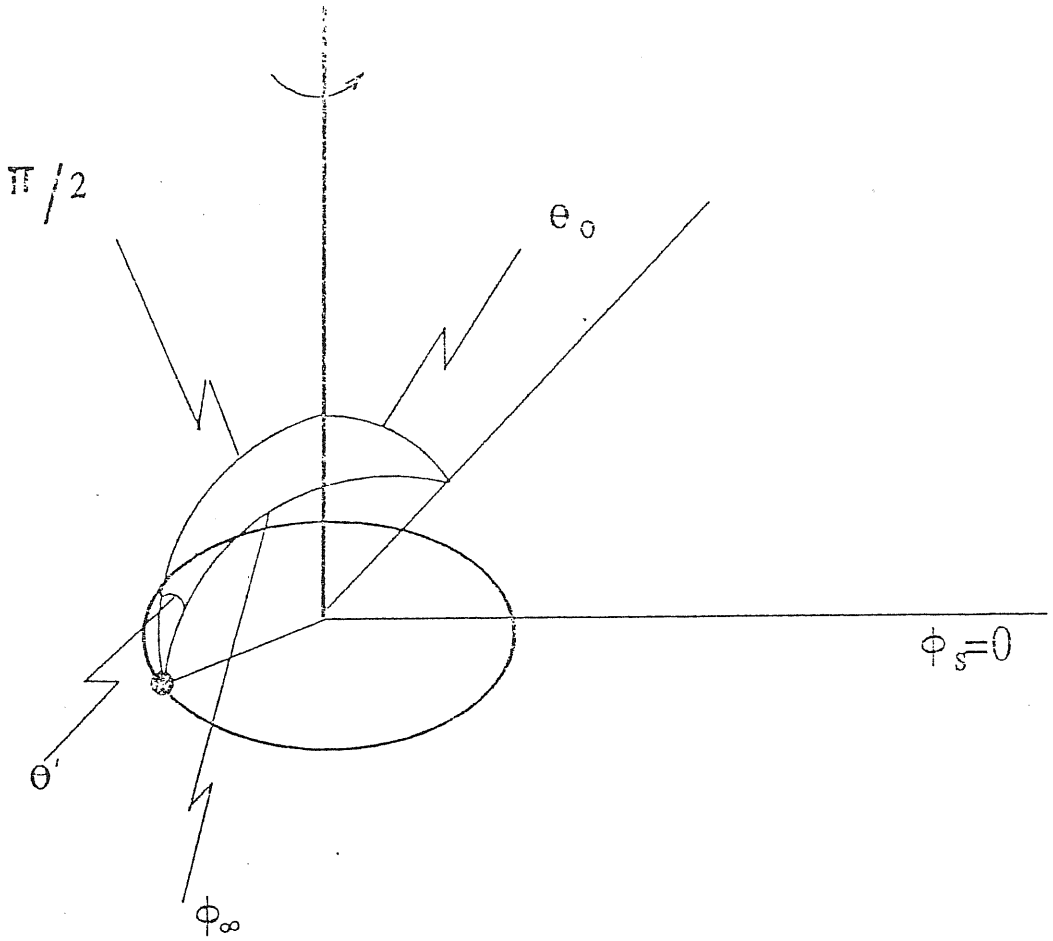


**Figure 2.1.** The spot rotates around the black hole with angular velocity $\Omega$, and the observer is at rest at infinity and located at $\phi_s = 0$ with the viewing angle $\theta_o$.

The spot rotates around the black hole with angular velocity $\Omega$, and the observer is at rest at infinity and located at angular position $\phi_s = 0$ with viewing angle $\theta_o$. The deflection angle of the photon emitted by the spot is $\phi_\infty$. As the

photon motion is planar in Schwarzschild space time, when the spot is at position 1(Fig. 2.2), its emitted photon which can reach the observer must move in plane 1; when the spot is at position 2, its motion should be in plane 2, and so on. $S$ is the photographic plate of the observer. The X-ray emitted from the spot is deflected by the black hole and intersects the photographic plate of the observer. The distance between $c$ and the point at which the photon reaches the plate should be the magnitude of the impact parameter for this special photon, which we call the special impact parameter $B$. The plane which contains the line connecting the black hole and the spot rotates around the line of sight as the spot moves around the black hole.

### 2.2.2 Calculating the impact parameter

A spot with observed intensity $I_{obs}$ which occupies a solid angle $\triangle\Pi$ has the observed energy flux

$$F_{obs} = I_{obs} \triangle \Pi. \tag{2.1}$$

It is well known (see, e.g., Misner, Thorne and Wheeler, 1973) that the volume in phase space, $V$, (measured in any local Lorentz frame) is conserved along the photon trajectory (the Liouville theorem in curved space time) though the phase space region it occupies changes. This leads to the Collisionless Boltzmann equation,

$$I_\nu/\nu^3 = \text{constant},$$

where $I_\nu$ is the specific intensity of radiation at given frequency $\nu$ measured in a specified local Lorentz frame. The intensity of a light source, integrated over its effective frequency range, is proportional to the fourth power of the redshift factor,

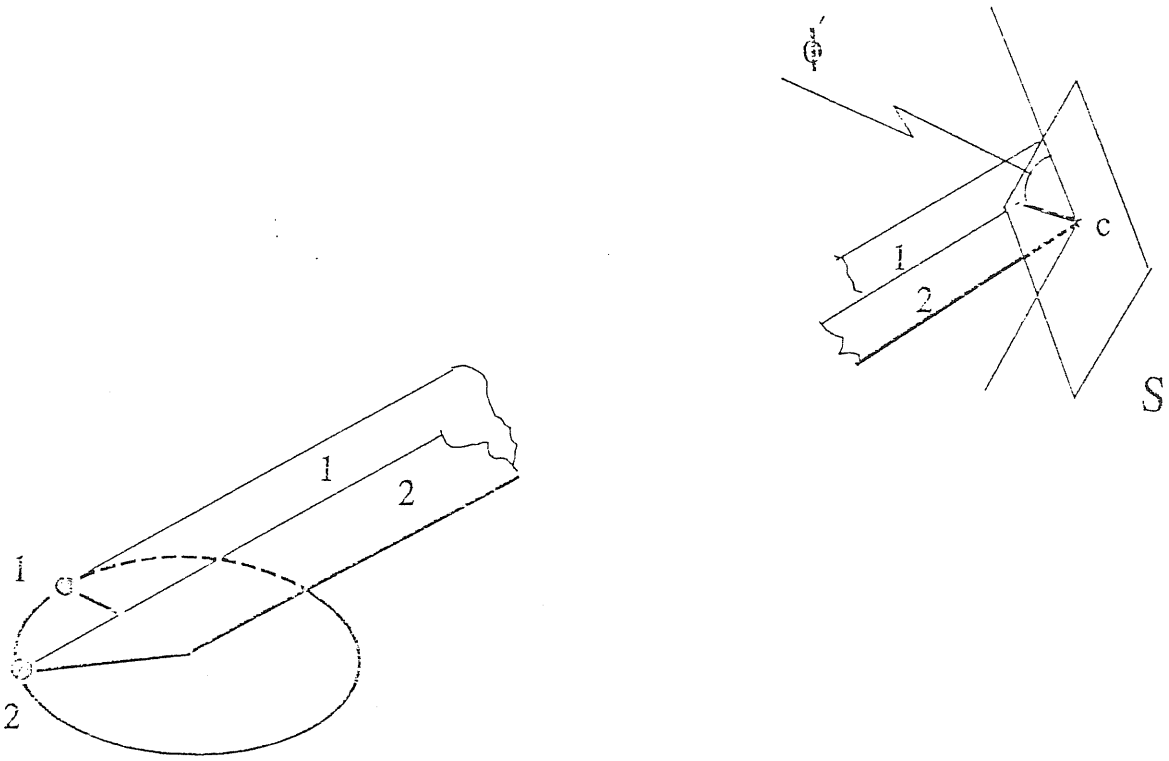


**Figure 2.2.** Photon motion is planar in Schwarzschild space time. Photon emitted at position 1 should move in plane 1, photon from position 2 should move in plane 2.... $S$ is the observer's photographic plate.

$g$

$$I_{obs} = g^4 I_{em}, \tag{2.2}$$

$I_{em}$ is the intensity measured at the rest frame of the spot.

The redshift factor is, by definition, the ratio of the observed energy of a photon, $E_{obs}$, to the energy of the photon in its source's rest frame, $E_{em}$,

$$g = E_{obs}/E_{em}. \tag{2.3}$$

The observed photon energy in terms of the four-momentum $\vec{P}$ of the photon

is

$$E_{obs} = -\vec{u}_{obs} \cdot \vec{P} = -P_t$$

where $\vec{u}_{obs}$ is the four-velocity of the observer. The energy measured in the rest frame of the spot is

$$E_{em} = -\vec{u}_{em} \cdot \vec{P}$$

where $\vec{u}_{em}$ is the four-velocity of the spot.

The Schwarzschild metric can be written as

$$ds^2 = -\left(1 - \frac{2M}{r}\right) dt^2 + \left(1 - \frac{2M}{r}\right)^{-1} dr^2 + r^2(d\theta^2 + \sin\theta^2 d\phi^2).$$

Here and in the following, the spherical coordinate and geometric units in which $G = c = 1$ will be used.

We now set up an orbiting orthonormal tetrad on the considered spot,

$$\vec{e}_{(\mu)} = \gamma^{\alpha}_{(\mu)} e_{\alpha}, \qquad \mu, \alpha = t, r, \theta, \phi$$

which comoves with the accretion disk. The time lag of the tetrad is the four-velocity of the spot, so its components can be expressed as

$$\gamma^{t}_{(t)} = \frac{1}{\sqrt{(1 - \frac{2M}{r})(1 - v_s^2)}}, \tag{2.4}$$

and

$$\gamma^{\phi}_{(t)} = \frac{\Omega}{\sqrt{(1 - \frac{2M}{r})(1 - v_s^2)}}, \tag{2.5}$$

where

$$v_s = \frac{\Omega r_s}{\sqrt{1 - \frac{2M}{r}}}$$

is the velocity of the spot measured in a local non-rotating frame and

$$\Omega = \left(\frac{M}{r}\right)^{3/2}$$

is its angular velocity. Choosing $\vec{e}_{(\phi)}$ to be orthonormal to $\vec{e}_{(t)}$, with $\vec{e}_{(\phi)}$ pointing in the $\phi$ direction in the comoving frame, and under the condition that the vector is unity, we obtain

$$\gamma_{(\phi)\phi} = \frac{r_s}{\sqrt{1-v_s^2}}, \tag{2.6}$$

$$\gamma_{(\phi)t} = -\Omega\gamma_{\phi(\phi)}. \tag{2.7}$$

The remaining two space-axes are chosen to be in the $r$ and $\theta$ directions and their components are

$$\gamma_{(r)r} = \frac{1}{\sqrt{1-\frac{2M}{r}}}, \tag{2.8}$$

$$\gamma_{(\theta)\theta} = r. \tag{2.9}$$

The energy of the emitted photon in the rest frame of the spot can therefore be written as

$$E_{em} = -\vec{u}_{em} \cdot \vec{P} = P^{(t)},$$

so $g$, the redshift factor, is found to be

$$g = -\frac{P_t}{\gamma_\mu^{(t)} P^\mu}.$$

Using the above equations we can find

$$g = \frac{\sqrt{(1-v_s^2)(1-\frac{2M}{r})}}{1-\Omega L}, \tag{2.10}$$

where $L$ is the impact parameter of the photons relative to the symmetry-axis. $L$ can be written as

$$L = -\frac{P_\phi}{P_t}.$$

The redshift factor is independent of both the energy $P_t$ and the angular momentum $P_\phi$ of the photon and only relies on their ratio, i.e. the direction in which the photon is emitted. This should be obvious if we write it in the following form:

$$L = \frac{\gamma_{\phi(t)} + \gamma_{\phi(\phi)} \cos\psi}{\gamma^t_{(t)} + \gamma^t_{(\phi)} \cos\psi}. \tag{2.11}$$

Substituting formula (2.4)–(2.9)and (2.11) into (2.10), we then obtain

$$g = \frac{\sqrt{1 - \frac{2M}{r}}}{\sqrt{1 - v_s^2}}(1 + \cos\psi v_s), \tag{2.12}$$

where $\psi$ is the angle between the beaming and the moving direction of the emitting matter. The absolute value of $\psi$ should be in the range of $0 \leq \psi \leq \pi$(under the assumption that the disk is optically thick, and that, once it crosses the disk, the photon will be absorbed).

It is obvious that $L$ is a constant for a special photon and a variable on the whole. This quantity changes periodically as the spot moves around the black hole. When the spot moves towards the observer, $g$ is amplified and the measured frequency of the photon is blueshifted, whereas when the spot recedes from the observer, the measured frequency is redshifted.

Now we calculate the redshift factor and the solid angle. Let us take advantage of the spherical symmetry to choose the "equatorial " plane $\theta = \frac{\pi}{2}$ for each particular photon which can reach the observer so that it includes photon trajectory considered. This means that the "equatorial" plane is different for different photons.

The deflection angle of the photon can be calculated from the geodesic equation for a photon (in the plane where the photon moves):

$$\frac{du}{d\phi} = 2u^3 - u^2 + \frac{1}{B^2},$$

where

$$u = \frac{1}{R},$$

$$R = \frac{r}{M},$$

and

$$u_s = \frac{1}{R_s},$$

and

$$\phi_\infty = \int_0^{u_s} \frac{B\,du}{\sqrt{2u^3B^2 - u^2B^2 + 1}}. \tag{2.13}$$

( For simplicity, here and in the following we will express physical quantities as dimensionless ones).

When the considered photon trajectory has a periastron, the formula (2.13) can be expressed in terms of the Jacobian elliptic integrals. When integrating equation (2.13), we must consider the turning point in the trajectory at which

$$2u^3B^2 - u^2B^2 + 1 = 0.$$

Fig. 2.3 shows the effective-potential for a photon. The concrete cases can be determined from the effective potential of the photon.

i.) When photon trajectory has no turning point, the deflection angle of the photon is

$$\phi_\infty = 2\left(\frac{p}{q}\right)^{1/2}\left[F(\chi_R/2,k) - F(\chi_\infty/2,k)\right]. \tag{2.14}$$

ii.) When the photon trajectory has a turning point, the deflection angle of the photon is

$$\phi_\infty = 2\left(\frac{p}{q}\right)^{1/2}\left[2K(k) - F(\chi_R/2,k) - F(\chi_\infty/2,k)\right], \tag{2.15}$$

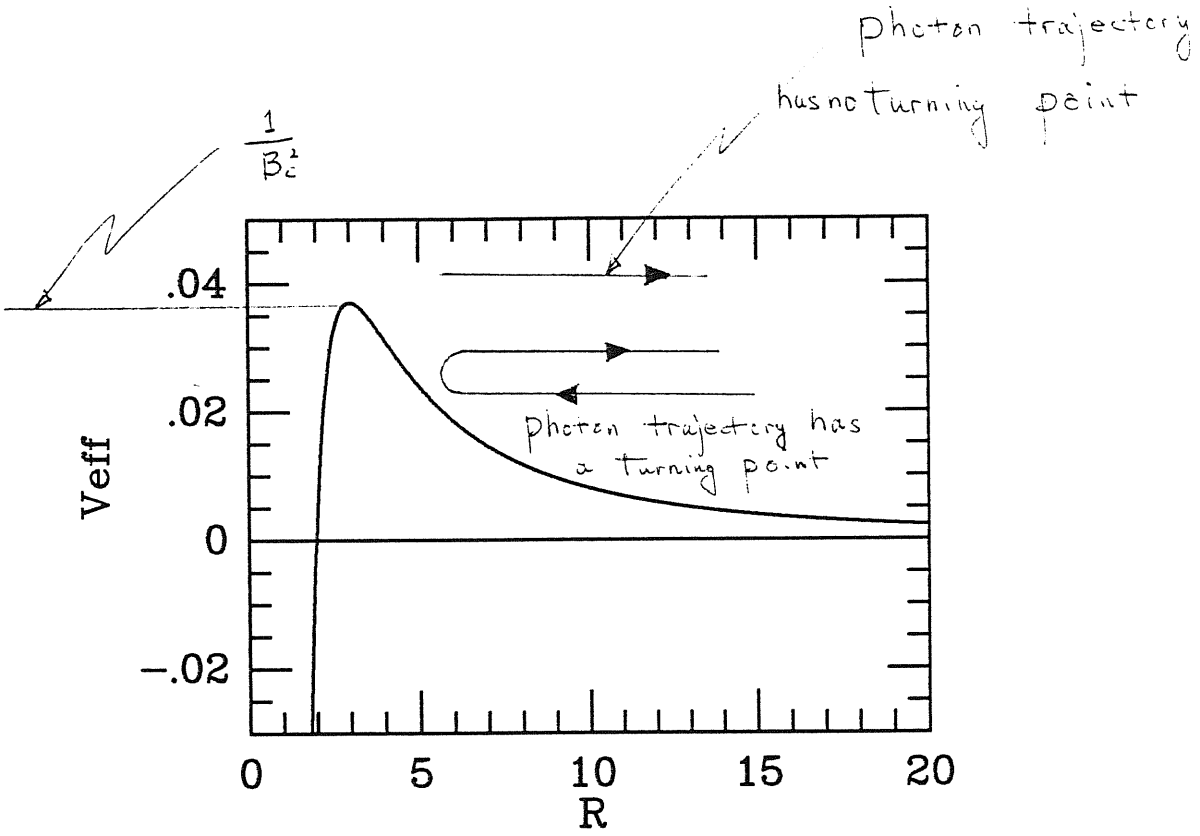


**Fig. 2.3** The effective-potential diagram for photon.

where

$$
\begin{aligned}
q^2 &= (p-2)(p+6), \\
k^2 &= \frac{1}{2q}(q-p+6), \\
\sin^2(\chi_R/2) &= \frac{\frac{4p}{R}+q-p+2}{q-p+6}, \\
\sin^2(\chi_\infty/2) &= \frac{q-p+2}{q-p+6}, \\
B^2 &= \frac{p^3}{p-2},
\end{aligned}
\tag{2.16}
$$

where $p$ refers to perihelion distance. The above formulae are obtained given the following two conditions:

(1) Only the direct images of photons are considered, that is, we only consider those photons whose trajectories do not cross the disk plane, since the photons which do cross this plane will be absorbed by the optically thick accretion disk;

(2) The spot is inside the accretion disk, i.e., $Rs \geq 6$.

From the geometry (Fig. 2.1), we can also find

$$\cos\phi_\infty = \sin\theta_o \cos\phi_s. \tag{2.17}$$

For a given observer ($\theta_o$ is given) through equations (2.14)– (2.16) and (2.17), we can solve the $B(\phi_s, R_s)$ relation and therefore find $L(\phi_s, R_s)$:

$$L = B\sin\theta' = -\frac{B\sin\phi_s\tan\theta_o}{\sqrt{1+\sin^2\phi_s\tan^2\theta_o}}.$$

### 2.2.3 Calculating the solid angle

Next we calculate the observed solid angle $\Delta\Pi$ subtended by the spot at the observer. This quantity can be expressed in terms of the special impact parameter,

$$\Delta\Pi = \frac{BdBd\phi'}{d^2},$$

with $\phi'$ expressed in Fig. 2.2 and can be calculated through

$$\sin\phi' = \frac{\sin\phi_s}{\sqrt{1-\cos^2\phi_s\sin^2\theta_o}}, \tag{2.18}$$

where $d$ is the distance between the observer and the emitting matter. The solid angle can also be rewritten in terms of the coordinates of the disk $R_s$ and $\phi_s$,

$$\Delta\Pi = \frac{B}{d^2}\left|\frac{\partial(B,\phi')}{\partial(R_s,\phi_s)}\right| dR_s d\phi_s.$$

Since the photon motion is planar, the Jacobian contains only $\frac{\partial B}{\partial R}$ and $\frac{\partial \phi'}{\partial \phi_s}$ terms. $\frac{\partial \phi'}{\partial \phi}$ is found to be

$$\frac{\partial \phi'}{\partial \phi} = \frac{\cos\theta_o}{1 - \sin\theta_o^2 \cos\phi_s^2} \tag{2.19}$$

and $\frac{\partial R}{\partial B}$ can be evaluated by perturbing the photon geodesic equation. This perturbation is done under the condition of fixing one end of the photon trajectory and varying the spot position $R_s$ and the special impact parameter of the photon $B$,

$$\frac{\partial R}{\partial B} = \frac{\sqrt{2u_s^3 - u_s^2 + \frac{1}{B^2}}}{u_s^2 B^3} \int_0^{u_s} \frac{du}{\sqrt{(2u^3 - u^2 + \frac{1}{B^2})^3}}. \tag{2.20}$$

The photon arrival time $\tau(B)$, which should be a function of $\phi_s$ for given $R_s$, is found to be the spot travel time plus the elapsing time $\Delta\tau$ of the photon from the spot to the observer, which can be obtained through the null geodesic equation of the photon,

$$\left(\frac{du}{d\tau}\right)^2 = u^4(1-2u)^2\left(1 - B^2u^2(1-2u)\right).$$

Therefore

$$\triangle\tau = \int_0^{u_s} \frac{du}{u^2(1-2u)\sqrt{1 - B^2u^2(1-2u)}}, \tag{2.21}$$

where

$$\tau = \frac{t}{M}.$$

Note that turning point should also be considered in the calculation of photon arrival time. Thus with the relation $B(\phi_s, R_s)$ we can calculate the solid angle $\Delta\Pi(\phi_s)$, the redshift factor $g(\phi_s)$, and therefore the flux $F(\tau)$.

### 2.2.4 The results

The calculation of $B(\phi_s, R_s)$ is done numerically and the calculation of $F(\tau)$ from a finite spot is obtained through the integration of equation (2.1). During the calculation we have to distinguish between several concrete cases, i.e. whether the photon trajectory has a turning point or not, and whether or not the special impact parameter of the photon is smaller than its critical value $B_c = 3\sqrt{3}$.

Fig. 2.4 shows the special impact parameter $B$ as a function of $\phi_s$ for three periods for different viewing angles $\theta_o = 80^o, 70^o$ and the different position of the spot, $r = 10r_g, 50r_g$. In each period, there exists a minimum between two maximums, which correspond to the two symmetry points of the orbit around $\phi_s = \pi/2$ and $\phi_s = 3\pi/2$. The minimum appears at position $\phi_s = \pi$, which corresponds to the maximum gravitational effects on the photon trajectory. Unlike the position $\phi_s = 0$ from which the observed photon can have impact parameter even much smaller than the critical value $3\sqrt{3}$, the photon emitted at position $\phi_s = \pi$ must have impact parameter larger than this critical value, otherwise it will be trapped by the black hole. It is shown that, as $R_s$ decreases, the relative difference of the impact parameter of the photon from $\phi_s = \pi$ and $\phi_s = \pi/2(or 3\pi/2)$ becomes smaller, which reflects the changes of the gravitational strength. The impact parameter of the photon from position $\phi_s = \pi$ must be larger than the critical value to avoid being captured by the black hole, while the closer radius position of the spot makes the impact parameter smaller. When the viewing angle increases, the minimum impact parameter decreases, the reason being that the larger viewing angle of the observer requires that the the observed photons have smaller impact parameter $B$.

Fig. 2.5 shows $\Delta\Pi$, the solid angle, as a function of $\phi_s$. In the flat space time, it is treated as a constant, whereas in general relativity it is a function of the

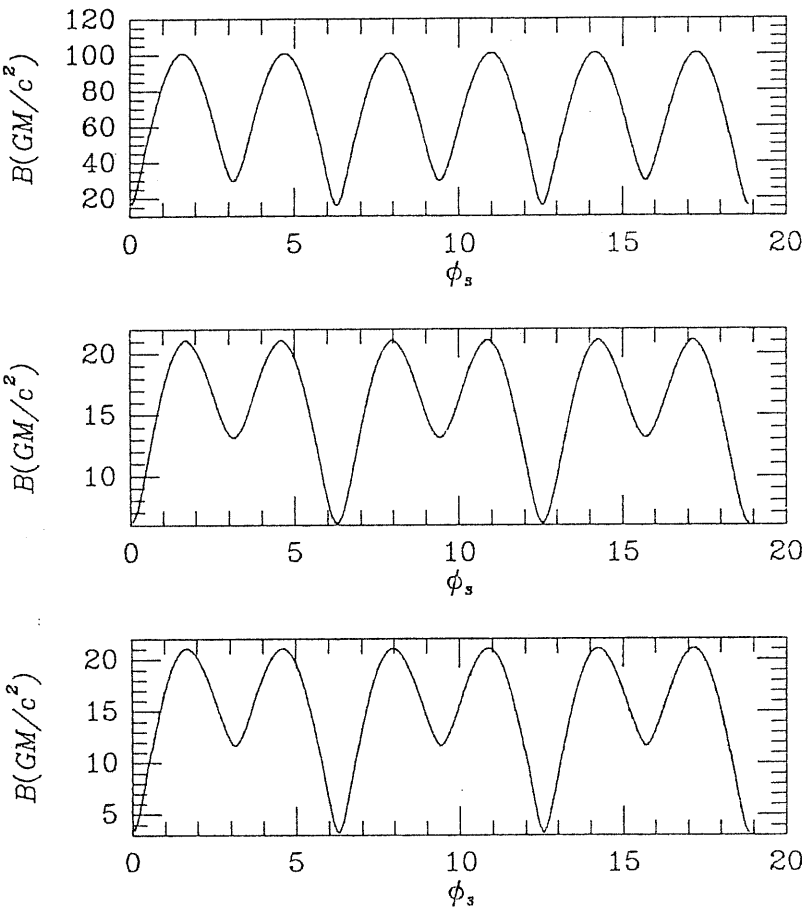


**Fig. 2.4** The $B$–$\phi_s$ relation for viewing angle $\theta = 80^o, 70^o$ and for different spot radial location $r = 10r_s$ and $r = 50r_s$.

impact parameter of the photon, the viewing angle of the observer and the position of the spots. The effective emission area of a spot changes as it moves around the black hole. There is a distinct peak at position $\phi_s = \pi$, as the photon emitted from

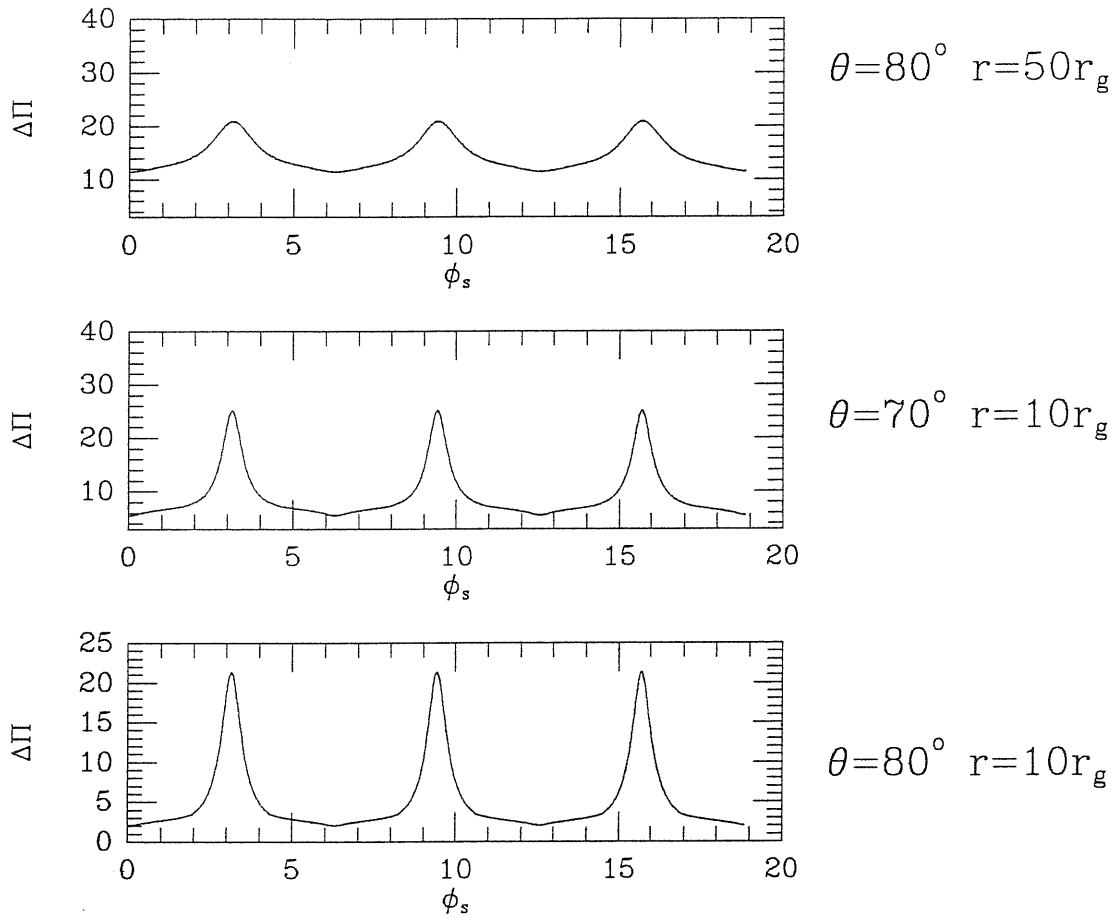


**Figure 2.5.** The solid angle $\Delta\Pi$ as a function of the spot position for the spot at $r = 10r_g, r = 50r_g$ and viewing angles $\theta_o = 80^o, 70^o$. The units for solid angle are arbitrary.

that position has to pass the black hole in order to reach the observer. Therefore, the gravitational lensing has the strongest effect on the photon when the spot is

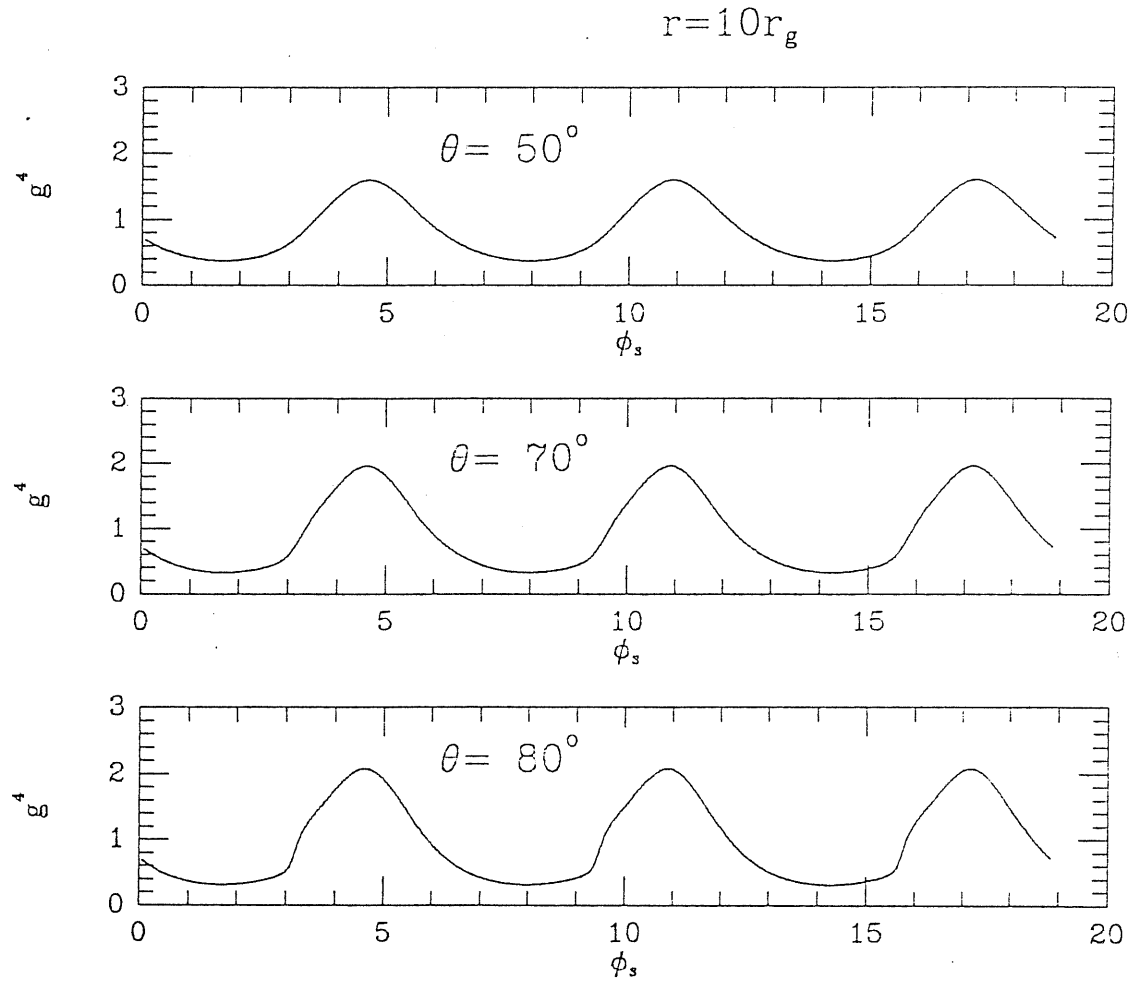


**Figure 2.6.** $g^4$ as a function of spot position $\phi_s$ for a spot at $r = 10r_g$ and viewing angle $\theta_o = 80^o, 70^o, 50^o$. The units for $g$ are arbitrary.

right behind the black hole. Fig. 2.6 shows $g^4$ as a function of $\phi_s$. When $\theta_o = 80^o$, there is a little upward tendency at the position $\phi_s = \pi$. This reveals that the Doppler effect dominates the $g^4$ while the gravitational lensing exerts less influence

on it. We also notice that the variation amplitude becomes larger as the viewing angle increases.

Fig. 2.7 shows a set of light curves for different spot position $r = 4r_g, 10r_g$ and different viewing angles of the observer $\theta_o = 80^o, 70^o, 50^0$. The flux can be expressed by the product of $g^4$ and solid angle $\Delta\Pi$ when $I_{em}$ is a constant (we assume that the radiation from the spot is isotropic). It is clear that the strong peaks are introduced by the solid angle of the spot, i.e. the gravitational lensing. In the flat space time the flux reaches its maximum and minimum at the position $\pi/2$ and $3\pi/2$ when the spot moves towards or recedes from the observer, while in general relativity the gravitational lensing occurs at orbital position $\pi$. Another peak thus appears between $\pi/2$ and $3\pi/2$ when we consider the combination effect. Because the peaks become weaker as the radius of the spot increases and the viewing angle decreases, the shape of each light curve is close to the result we get in the flat space time. It is worth noticing that the variation amplitude gets larger as the viewing angle increases. As the spot goes inwards, the absolute amplitude is reduced due to the gravitation. This can be understood from formula (2.10) where $\sqrt{(1-v_s^2)(1-\frac{2}{R_s})}$ shows that the Doppler shift and gravitational redshift factor both control the absolute strength.

### 2.2.5 Conclusions

- The gravitational lensing and the Doppler effect produce sharp flares in the light curve when the spot orbit has a large inclination angle.
- The strength and the width of the flare are strong functions of the viewing angle of the observer and the location of the spot.
- The gravitational effect is mainly seen in the solid angle of the spot subtending

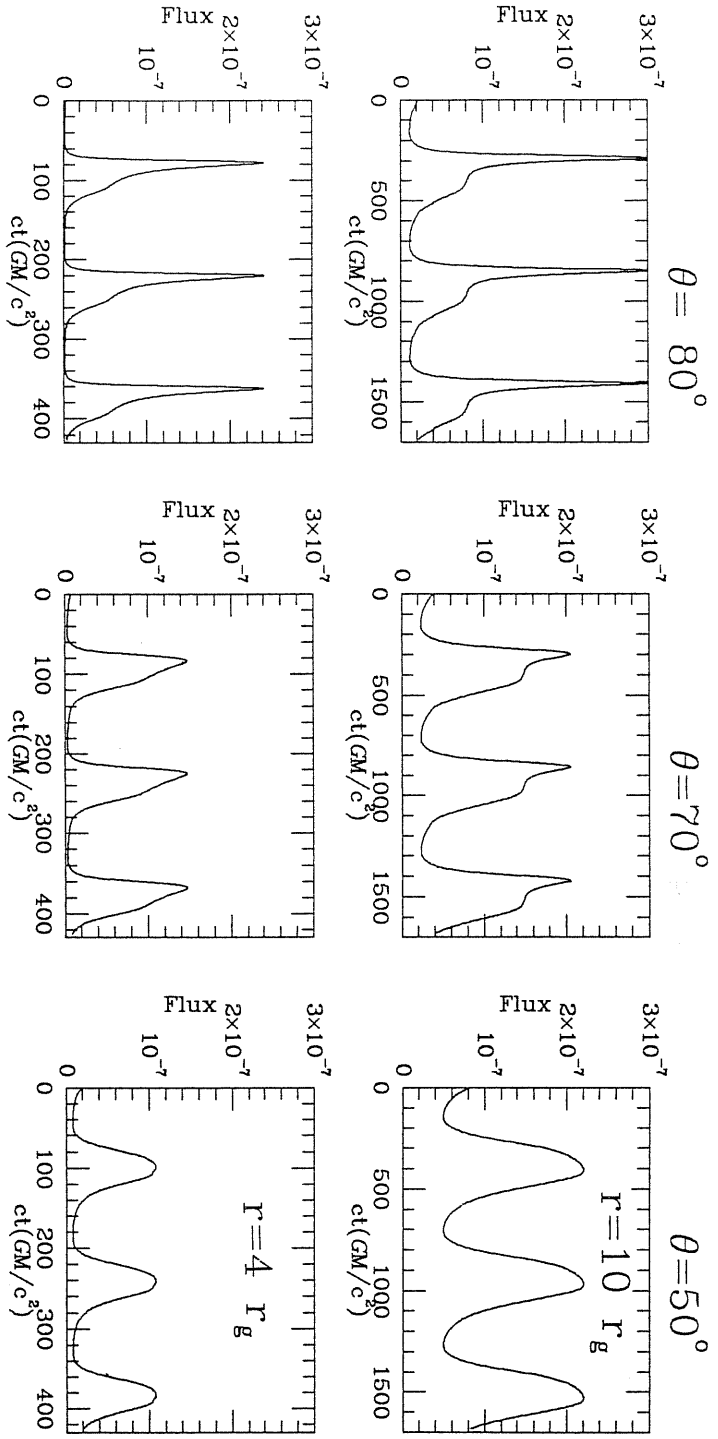


**Figure 2.7**. The light curves of the spots for different viewing angles $\theta_o$ = $80^o, 70^o, 50^o$ and different spot position $r = 4r_g, 10r_g$. The units for flux are arbitrary, $ct$ is in the unit of $\frac{GM}{c^2}$, where $c$ is the speed of light and $t$ is photon arrival time.

at the observer, while its minor effect is revealed in the redshift factor.

- The shape of the light curve of a single spot is far from sinusoidal when the gravitational effect is very strong.

## 2.3 Some properties of the gravitational lensing

To know how the lensing effect depends on the free parameters quantitatively, e.g., the radial location of $r$ and the inclination of the orbit, we fit the solid angle with a gaussian function. The fitting is done through the whole parameter space of inclination angle $\theta_o$ and the inner region of the disk $r \leq 100M$. The signal calculated from a Keplerian disk around a Schwarzschild black hole is used.

According to Fig. 2.5, we use the gaussian function plus a constant to fit the solid angle the spot subtended at the observer, which reads

$$\Delta\Pi = g_n \times e^{-\frac{1}{2}\left(\frac{t-g_c}{g_w}\right)^2} + c_o, \tag{2.22}$$

where $g_n$ refers to the amplitude of Gaussian peak representing the strength of the lensing, $g_w$ the Gaussian width representing the width of the peak due to the lensing in the light curve, $g_c$ the center of the peak, and $c_o$ the constant used in the fitting. It is expected that $g_n, g_w, c_o$ be a function of both the inclination angle and the radial location of a spot, $g_c$ only a function of radius $r$ where the spot is located, since it is only related to the orbital period of the spot. The difference between the fitting and the theoretical value is found to be less than 5%. The relativistic signal is calculated for different inclination angle $\theta_o$ and different radial location $r$ Fig. 2.9 shows the fitted $g_w$ as a function of the inclination angle for a spot at different radius. (a), (b), (c), (d), (e) and (f) refer to the cases of $r = 4r_s, 6r_s, 8r_s, 10r_s, 15r_s, 20r_s$. The width of the flare due to the lensing is

almost a liner function of the inclination angle $\theta_o$ for a fixed $r$. As the inclination angle increases, the width of the flare decreases, which implies that at a large inclination angle the peak due to the lensing in the light curve is sharper.

Fig. 2.8 shows the fitted $g_n$ as a function of the inclination angle for a spot at different radius. (a), (b), (c), (d), (e) and (f) refer to the cases of $r = 4r_s, 6r_s, 8r_s, 10r_s, 15r_s, 20r_s$. For $\theta_o \leq 80^o$, the amplitude of the lensing rises almost linearly as the inclination angle $\theta_o$ increases. After $\theta_o = 80^o$, it goes up extremely faster, which shows that $80^o$ (or some value around it) is a critical value for lensing. The dependence of the $g_n$ on the radial location of the spot is not that obvious. This does not mean that the lensing is not sensitive to the radial coordinate. First, the relative amplitude (the relative hight of the peak and the arm) of the flare in the light curve can be greatly changed because the $g$ is a strong function of the radial coordinate; second, the width of the peak due to the lensing is sensitive to $r$.

Fig. 2.10 shows $c_o$ as a function of the inclination angle for a spot at different radius. (a), (b), (c), (d), (e), and (f) refer to the cases for $r = 4r_s, 6r_s, 8r_s, 10r_s, 15r_s, 20r_s$.

As the inclination angle increases, the $c_o$ decreases, which indicates that more distinct flares will be observed in the light curves at a larger inclination angle.

Analytic formulae are given for the solid angle which read

$$g_c = \frac{\pi}{\Omega} + 0.5 \sin\theta R_s,$$

$$c_o = 1.118R_s + 0.156 - (1.092R_s - 1.331)10^{-2}\theta_o \qquad (\theta_o \leq 60^o),$$

$$c_o = 1.363R_s + 2.065 - (1.5R_s + 1.85)10^{-2}\theta_o \qquad (\theta_o > 60^o),$$

$$g_w = 6.878R_s - 19.067 - (4.417 \times 10^{-2} R_s + 0.152)\theta_o \qquad (\theta_o < 50^o, R_s < 25M),$$

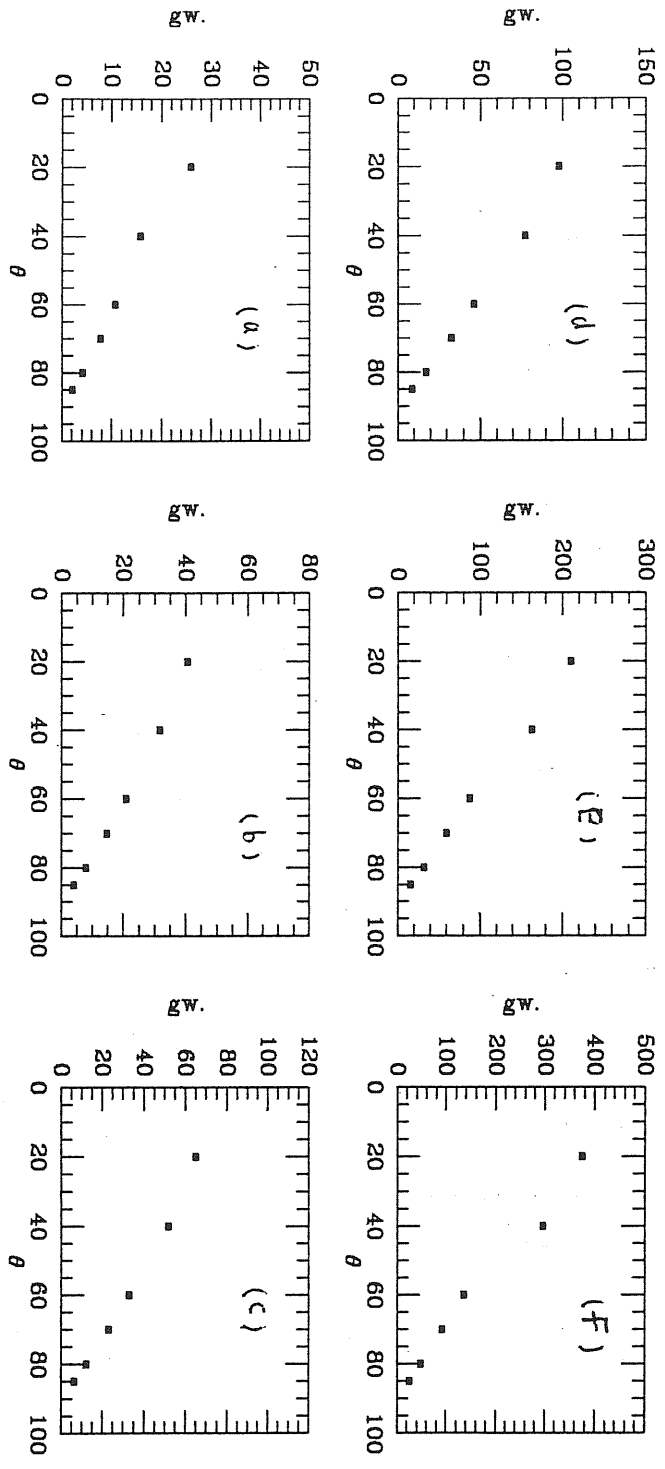


**Figure 2.9.** The fitted $g_w$ as a function of inclination angle $\theta_o$ for different radial locations of a spot. (a), (b), (c), (d), (e) and (f) refer to the cases of $r = 4r_s, 6r_s, 8r_s, 10r_s, 15r_s, 20r_s$ respectively. The units for $g_w$ are arbitrary, and the unit for the inclination angle is degree.

$$g_w = 19.7R_s - 334.16 - (0.159R_s - 2.414)\theta_o \qquad (\theta_o < 50^o, R_s \geq 25M),$$

$$g_w = 7.748R_s - 24.02 - (8.55 \times 10^{-2}R_s - 0.2616)\theta_o \qquad (\theta_o \geq 50^o, R_s < 25M),$$

$$g_w = 14.59R_s - 178.77 - (0.1613R_s - 1.983)\theta_o \qquad (\theta_o \geq 50^o, R_s > 25M),$$

$$g_n = 8.76 \times 10^{-2}R_s - 4.191 - (1.46 \times 10^{-3}R_s - 0.2782)\theta_o \qquad (\theta_0 < 80^o),$$

$$g_n = 2.18R_s - 497.4 - (2.906 \times 10^{-2}R_s - 6.633)\theta_o \qquad (\theta_o > 80^o).$$

In the above formulae $R_s$ is dimensionless, $\theta_o$ is in the units of degree. Fig. 2.11 shows the comparison between the solid angle calculated by using the approximated formula and that calculated through the method introduced in section 2. The spot is at $6r_s$ for (a) and (b), at $20r_s$ for (c), the inclination angles are $70^o$ for case (a) and $85^o$ for cases (b) and (c).

Our future work will include fitting the redshift factor $g$. As is described in section 2 of this chapter, the solid angle and the redshift factor are two basic quantities. The fitted formula can be used to derive whatever is needed, e.g., the variability power spectrum, the energy spectrum and the emission line from a relativistic disk through a simple algebra calculation.

### 2.3.1 Conclusion

- The lensing effect is most sensitive to the inclination angle, especially when the inclination angle is larger than $80^o$ (or some value around it).
- The width of the flares due to the lensing in the light curve increases as the spot goes outwards. The lensing effect diminishes when the width goes to infinity.

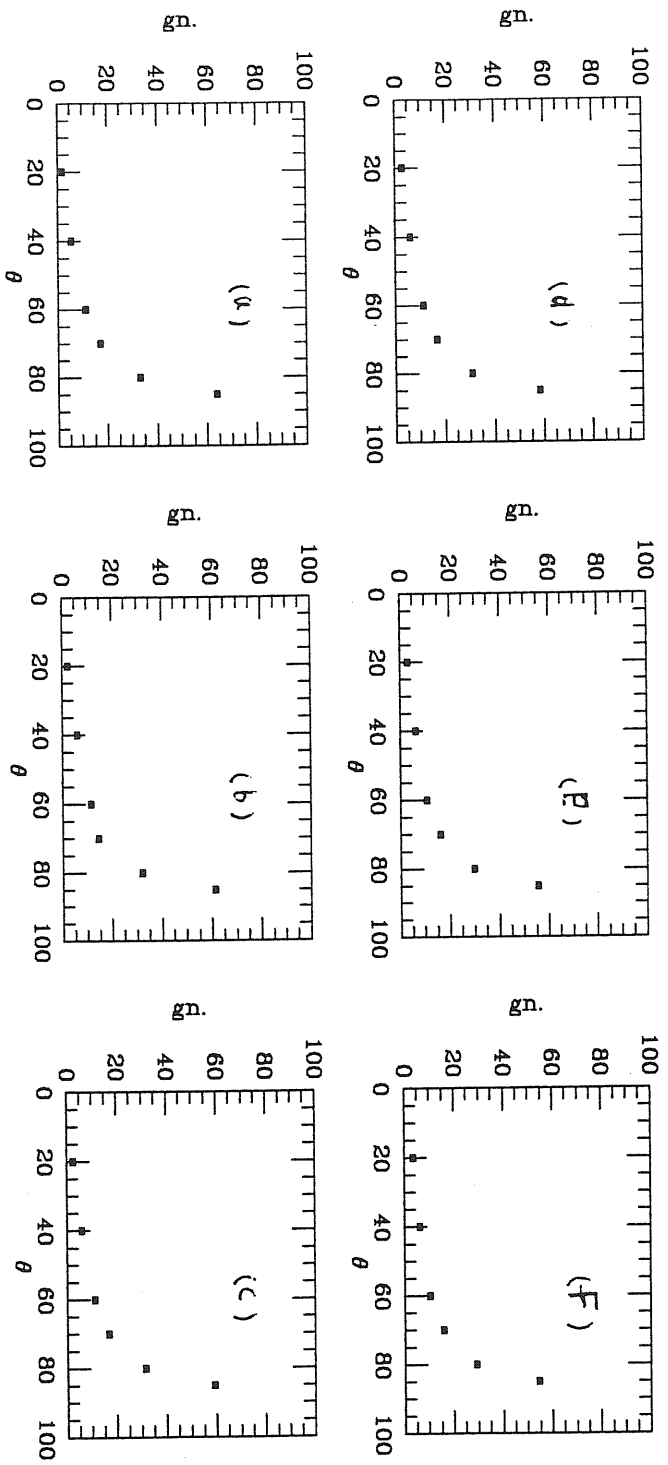


**Figure 2.8.** The fitted $g_n$ as a function of inclination angle $\theta_o$ for different radial location of the spot. (a), (b), (c), (d), (e) and (f) refer to the cases of $r = 4r_s, 6r_s, 8r_s, 10r_s, 15r_s, 20r_s$ respectively. The units for $g_n$ are arbitrary, and the unit for the inclination angle is degree.

## 2.4 Non-isotropic radiation

The radiation both from a spot and from the disk itself may be non-isotropic, and the emitted energy flux can be angularly dependent. In this part, we give analytic expression for the relation between the impact parameter of a photon and the angular direction in which the photon is emitted.

We consider a thin disk around a Schwarzschild black hole. The four-momentum of a photon has components:

$$
\begin{aligned}
p^t &= \frac{1}{(1-\frac{2M}{r})^2} \\
p^r &= \left(1-(1-\frac{2M}{r})\frac{B^2}{r^2}\right)^{1/2} \\
p^\theta &= \frac{1}{r^2}\left[B-L\right]^{1/2} \\
p^\phi &= \frac{L}{r^2}
\end{aligned}
\tag{2.23}
$$

where the impact parameters $B$ and $L$ are defined in section 2.

The three angles measured in the rest frame of the spot are:

$$
\begin{aligned}
cos\hat{\theta} &= -\frac{p^{(\theta)}}{p^{(t)}} = \frac{\gamma_\mu^{(\theta)} p^\mu}{\gamma_\nu^{(t)} p^\nu} \\
&= \sqrt{1-v^2}\,\frac{\left[(\frac{B}{r})^2-(\frac{L}{r})^2\right]^{1/2}}{1-\Omega L},
\end{aligned}
\tag{2.24}
$$

$$
\begin{aligned}
\cos\hat{\gamma} &= -\frac{p^{(r)}}{p^{(t)}} \\
&= \sqrt{1-v^2}\,\frac{\left[1-(1-\frac{2M}{r})\frac{B}{r}\right]^{1/2}}{1-\Omega L},
\end{aligned}
\tag{2.25}
$$

$$
\cos\hat{\psi} = -\frac{p^{(\phi)}}{p^{(t)}}
$$

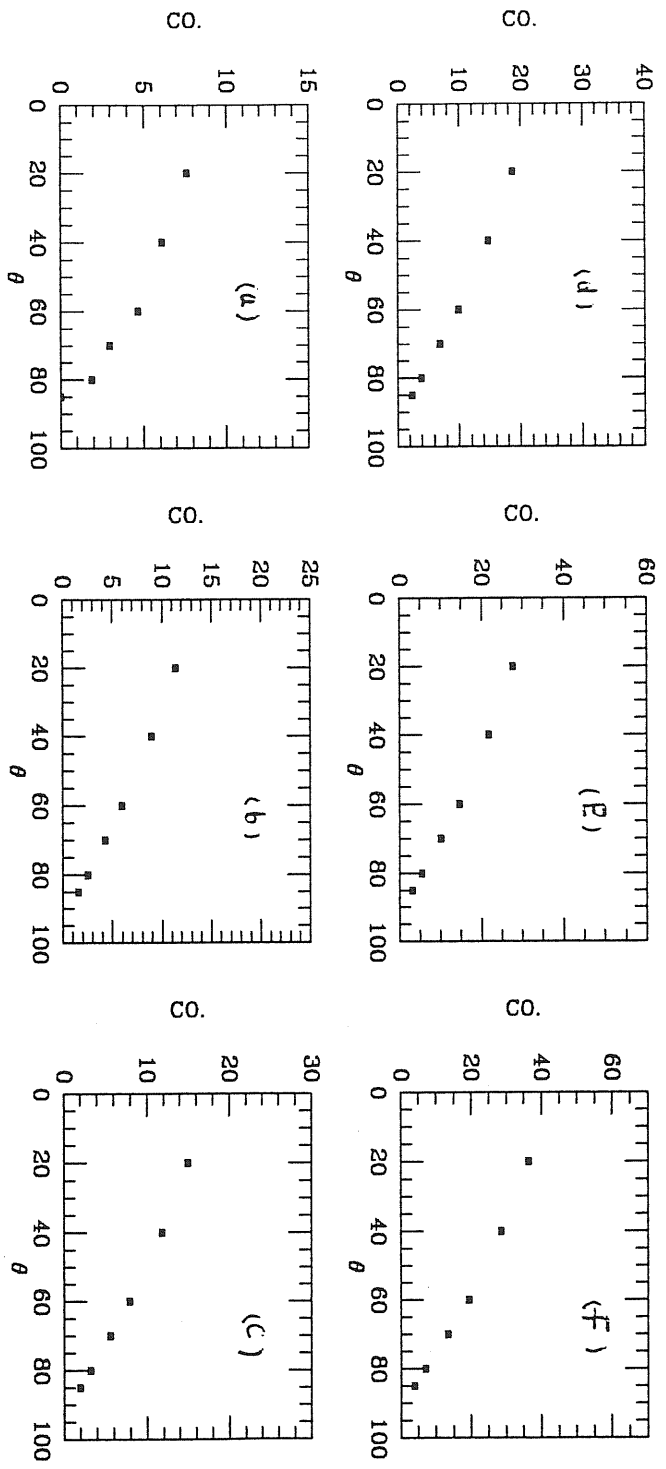


**Figure 2.10.** The fitted $c_o$ as a function of the inclination angle $\theta_o$ for different radial locations of the spot. (a), (b), (c), (d), (e) and (f) refer to the cases of $r = 4r_s, 6r_s, 8r_s, 10r_s, 15r_s, 20r_s$ respectively. The units for $c_o$ are arbitrary, and the unit for the inclination angle is degree.

$$= \sqrt{1-\frac{2M}{r}}\frac{\left[\frac{\Omega r}{1-\frac{2M}{r}}-\frac{L}{r}\right]}{1-\Omega L}. \tag{2.26}$$

In deriving the above formulae $\frac{p_\phi}{P_t} = -L$ is used. Now we can write the flux due to a finite spot as

$$F = \int\int f(\hat{\theta},\hat{\psi},\hat{\gamma}) I_{em} g^4(B) \frac{B}{d^2}\frac{\partial B}{\partial R}\frac{\partial \phi'}{\partial \phi_s} dR_s d\phi_s, \tag{2.27}$$

where $\frac{\partial B}{\partial R}$ and $\frac{\partial \phi'}{\partial \phi_s}$ can be calculated from Eqs. (2.19) and (2.20). $f$ represents the dependence of flux on the direction in which the photon is emitted. It is not a well defined quantity. Nevertheless, if there is a thick electron scattering atmosphere above the disk surface, $f$ is described by the well-known "limb darkening law" (Chandrasekhar, 1960),

$$f(\hat{\theta},\hat{\psi},\hat{\gamma}) \sim 1 + 2.06\cos\hat{\theta}$$

$$\sim 1 + 2.06\sqrt{1-v^2}\frac{\left[(\frac{B}{r})^2 - (\frac{L}{r})^2\right]^{1/2}}{1-\Omega L}, \tag{2.28}$$

where $\hat{\theta}$ is the emitting angle of the photon relative to the normal of the disk measured at the emitting frame. Once we know the location of the observer and the emitting matter ($\theta_o, R_s, \phi_s$ are given), with the methods introduced in section 2, we can calculate $f(\hat{\theta},\hat{\psi},\hat{\gamma})$ and also the flux due to non-isotropic radiation.

## 2.5 The light curve due to disk self-eclipse

The disk self-eclipse occurs when dense, accreting material is in the line of sight, in which case part of the disk is obscured by the disk itself. This should be a phenomenon common to AGN and galactic accreting systems. The eclipse by the disk itself would largely account for the X-ray variabilities both AGN and galactic X-ray sources. The study of the signal variability would improve our understanding

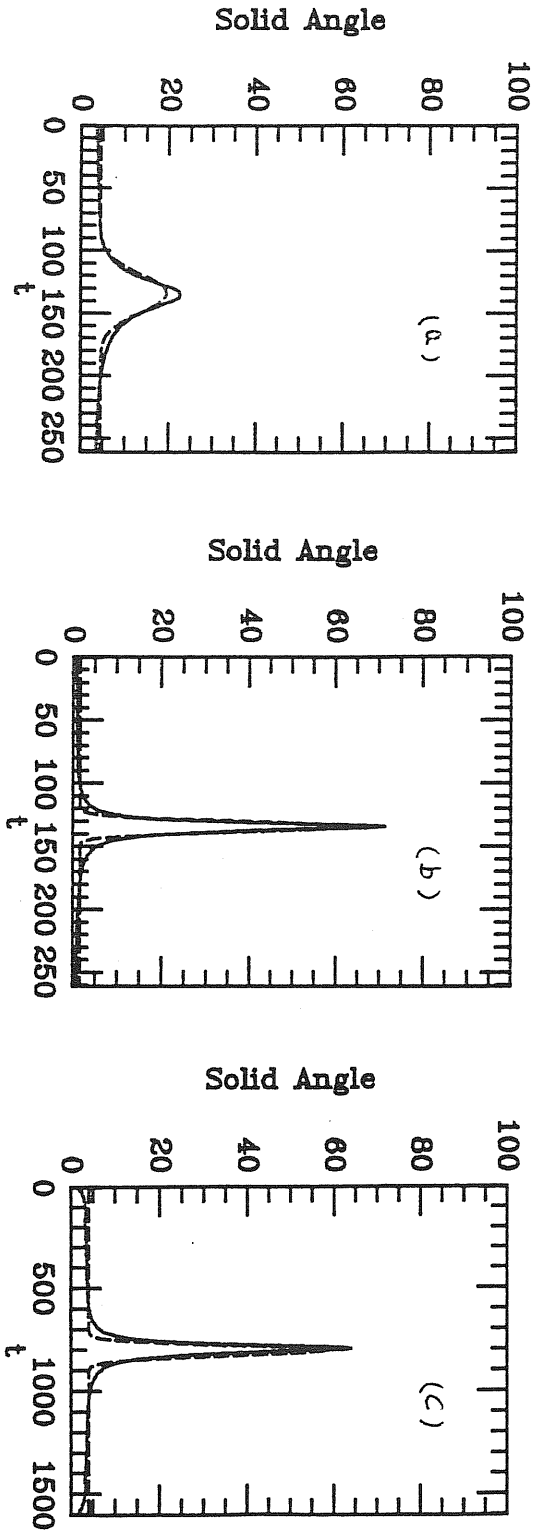


**Figure 2.11** The solid angle calculated both from the approximated formula and from solving the field equation. The dotted line refers to the result from approximated formula.

of the geometry of the accretion disk, the orbital period, and further the central mass of the black hole.

The effect of disk self-eclipse has been postulated by Milgrom (1978), Parmar and White (1988), and Mason (1989) as an explanation for the observed X-ray dips in some galactic X-ray sources. The dips have been observed in X-ray light curves of some low-mass X-ray Binaries (LMXRB), e.g. EXO 0748-676. The dips are caused by the disk absorption. In an LMXRB system, the material from the mass-donating companion star forms an accretion disk around the neutron star. The outer edge of the disk is thicker than its central part. If the viewing angle of the observer is large enough, the outer part of the disc may block the view, which produces dips in the X-ray signal.

Although the vertical structure of the accretion disk has not been fully defined due to the insufficient knowledge of the energy liberation processes of accreting matter, various theoretical attempts have been made. For example, Wandel and Liang (1991) have presented a hybrid accretion disk model for AGNs. Their solutions yield various disk shapes. Szuszkiewicz (1992,1989) also provides different shapes of slim disks. In this section, we assume a dense, optically thick and vertically–structured disk. Its outer part is thicker than its inner part as expressed in Fig. 2.12a. The disk opening angle is $\theta_w(r)$ and the top of the disk is at $R_w$. The realistic disk could be complicated with $\theta_w$ as a strong function of $r$, the disk radius coordinate. The methods we use can be applied to any case once $\theta_w(r)$ is given.

### 2.5.1 The geometry and calculations

Let us first consider a small spot on the disk moving around a Schwarzschild

black hole. In comparison with the black hole, the gravitational effect of the surrounding matter is much weaker and therefore can be neglected. The disk is optically thick while the outside material is optically thin. In this case, photons can travel freely once emitted. The spot radiates the X-ray photons isotropically in its own rest frame. The deflection angle of a photon emitted by the spot is $\phi_\infty$. As the photon motion is planar in the Schwarzschild space time, the motion must always be confined to a properly chosen "equatorial" plane.

The redshift factor is

$$g = \frac{\sqrt{(1 - v_s^2)(1 - \frac{2}{R})}}{1 - \Omega L},$$

where

$$L = \frac{l}{E}$$

(again we use the spherical coordinates and geometric units, and all physical quantities are expressed as dimensionless) is the impact parameter of photons relative to the symmetry-axis, i.e. the azimuthal component of the impact parameter $B$. $E$ and $l$ are the energy and angular momentum of the photon. The velocity of the spot measured in the frame of a local static observer is

$$v_s = \frac{\Omega R_s \sin\theta_w(r)}{\sqrt{1 - \frac{2}{R_s}}}.$$

where $R_s$ is the radial location of the emitting matter. The angular velocity on the surface of the disk remains to be determined. It depends on the shape of the disk. We will discuss this briefly at the end of the section.

The deflection angle can be calculated from the geodesic equation for photons,

$$\phi_\infty = \int_0^{u_s} \frac{B\,du}{\sqrt{2u^3B^2 - u^2B^2 + 1}}.$$

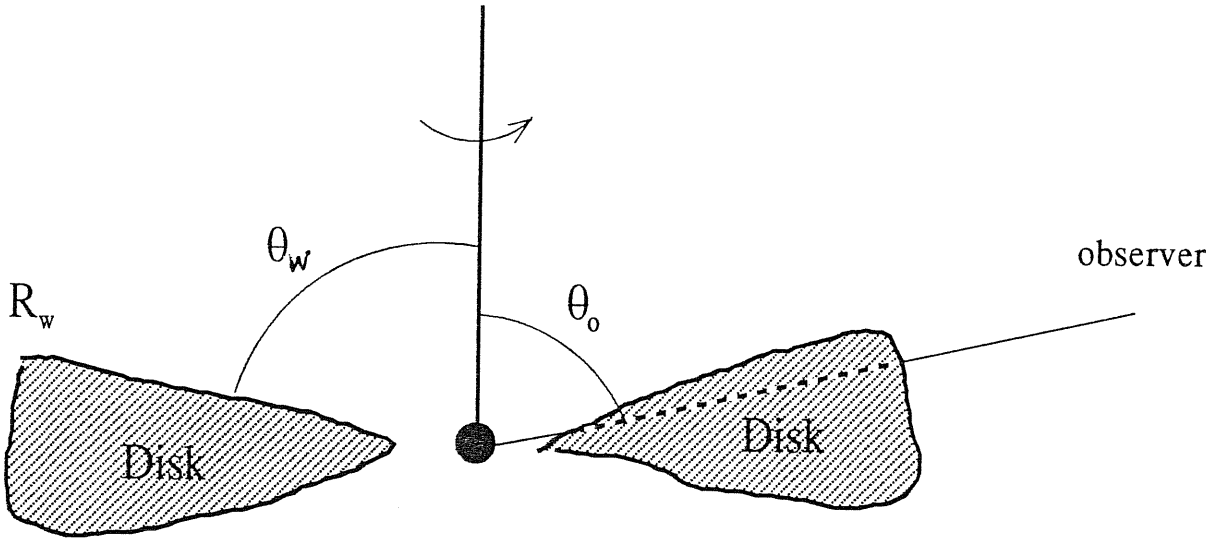


**Figure 2.12a.** The spot rotates around the black hole with angular velocity $\Omega$; the observer is at rest at infinity and located at $\phi_s = 0$ with viewing angle $\theta_o$; the disk has its top at $R_w$ and opening angle $\theta_w$; and $S$ is the observer's photographic plate.

When the considered photon trajectory has a periastron $p$, the formula can be expressed in terms of the Jacobian elliptic integrals in the form

$$\phi_\infty = 2\left(\frac{p}{q}\right)^{1/2}[F(\chi_s/2,k) - F(\chi_\infty/2,k)] \tag{2.14}$$

for photons without a turning point above the orbital plane of the spot and

$$\phi_\infty = 2\left(\frac{p}{q}\right)^{1/2}[2K(k) - F(\chi_s/2,k) - F(\chi_\infty/2,k)] \tag{2.15}$$

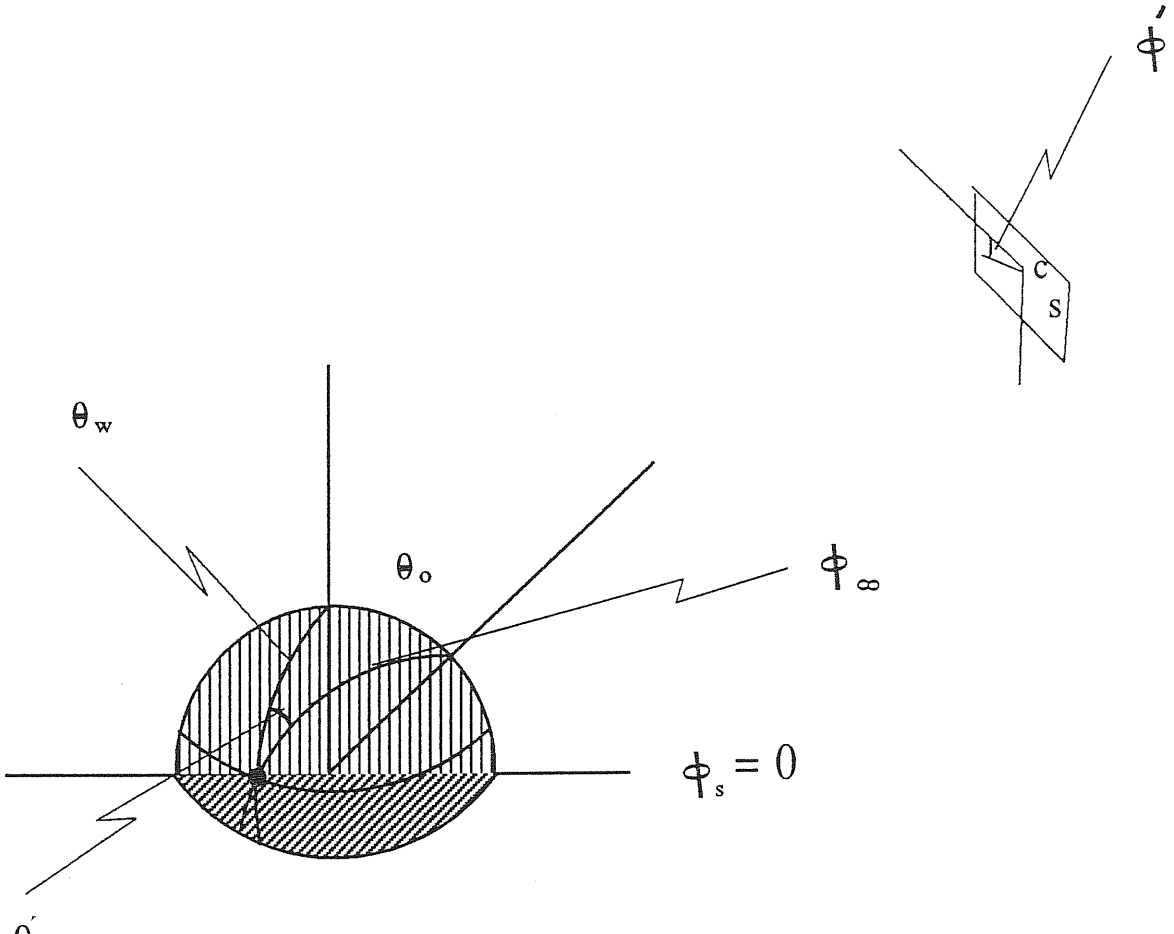


**Figure 2.12b.** The spot rotates around the black hole with angular velocity $\Omega$; the observer is at rest at infinity and located at $\phi_s = 0$ with viewing angle $\theta_o$; the disc has its top at $R_w$ and opening angle $\theta_w$; and $S$ is the observer's photographic plate.

for photons with a turning point above the orbital plane.

From the geometry (Fig. 2.12), we can find the relation

$$\cos\phi_\infty = \sin\theta_w \sin\theta_o \cos\phi_s + \cos\theta_o \cos\theta_w. \tag{2.29}$$

The impact parameter $B$ can be obtained from (2.14), (2.15), and (2.29) once the coordinates of the spot and the observer are given.

Through the geometry (see Fig. 2.12 ) we know that

$$L = \sin\theta' B,$$

where $\theta'$ can be calculated from

$$\sin\theta' = -\frac{\sin\phi_s \sin\theta_o}{\sqrt{1-\cos^2\phi_\infty}}. \tag{2.30}$$

The observed solid angle $\triangle\Pi$ subtended by the spot at the observer can be expressed in terms of the special impact parameter $B$,

$$\triangle\Pi = \frac{B}{d^2}\frac{\partial B}{\partial R}\frac{\partial\phi'}{\partial\phi_s} dR_s d\phi_s,$$

where $\frac{\partial\phi'}{\partial\phi}$ is found to be

$$\frac{\partial\phi'}{\partial\phi_s} = \cos^2\phi'\left(\frac{\cos\phi_s\sin\theta_w}{\cos\theta_o(\tan\theta_o\cos\theta_w - \cos\phi_s\sin\theta_w)}\right.$$
$$\left. - \frac{\sin^2\phi_s\sin^2\theta_w}{\cos\theta_o(\tan\theta_o\cos\theta_w - \cos\phi_s\sin\theta_w)^2}\right), \tag{2.31}$$

where

$$\phi' = \arctan\left(\frac{\sin\phi_s\sin\theta_w}{\cos\theta_o(\tan\theta_o\cos\theta_w - \cos\phi_s\sin\theta_w)}\right),$$

and $\frac{\partial R}{\partial B}$ can be calculated by

$$\frac{\partial R}{\partial B} = \frac{\sqrt{2u_s^3 - u_s^2 + \frac{1}{B^2}}}{u_s^2 B^3}\int_0^{u_s}\frac{du}{\sqrt{(2u^3 - u^2 + \frac{1}{B^2})^3}}. \tag{2.32}$$

With the relation $B(\phi_s, R_s)$, we can calculate the solid angle $\Delta\Pi(\phi_s)$, the redshift factor $g(\phi_s)$, and therefore the flux $F(\tau)$ through the integration of equation (1) over the effective area. For a given $R_s$, the photon arrival time $\tau(B)$ is a function of $\phi_s$. It is given by the spot travel time plus the elapsed time $\Delta\tau$ of the photon

moving from the spot to the observer. The calculation of $B(\phi_s, R_s)$, $\Delta\Pi(\phi_s)$ and $F(\tau)$ is done numerically.

Once we have the $B(\phi_s, R_s)$ , we can determine if the photon with impact parameter $B$ can be absorbed by the disk or not.

### 2.5.2 The condition of eclipsing

When the the viewing angle $\theta_o$ is larger than the opening angle of the disk $\theta_w$ (for a complicated shape of disk, $\theta_w$ refers to the angle between the symmetry axis and the line linking the center and the top of the disk), part of the disk will be obscured. This is, however, a very loose condition for eclipse. In special relativity, a photon goes along a straight line, and the eclipse phase ($\phi_e$) of an orbit at $R_s$ can be derived directly from the geometry,

$$\phi_e = \arccos\left(\frac{1}{2R_s}\left[(R_s + R_w)\frac{\tan\theta_w}{\tan\theta_o} - (R_w - R_s)\frac{\tan\theta_o}{\tan\theta_w}\right]\right).$$

In general relativity, a photon goes along a curved line. So the eclipse condition must be calculated from the geodesic equation.

To find the eclipse condition, we define $\phi_c$ as

$$\phi_c = \int_{u_w}^{u_s} \frac{B\,du}{\sqrt{2u^3B^2 - u^2B^2 + 1}}, \tag{2.33}$$

where

$$u = \frac{1}{R}, u_s = \frac{1}{R_s}, u_w = \frac{1}{R_w}.$$

When the considered photon trajectory has a periastron $p$, this formula can be expressed in terms of the Jacobian elliptic integrals in the form

$$\phi_c = 2\left(\frac{p}{q}\right)^{1/2}\left[F(\chi_s/2, k) - F(\chi_w/2, k)\right] \tag{2.34}$$

for photons without a turning point above the orbital plane and

$$\phi_c = 2\left(\frac{p}{q}\right)^{1/2}[2K(k) - F(\chi_s/2,k) - F(\chi_w/2,k)] \tag{2.35}$$

for photons with a turning point above the orbital plane. Here, $K(k)$ denotes the complete elliptic integral, and $\chi_s$ is defined in section 2.2 of this chapter and

$$\sin^2(\chi_w/2) = \frac{\frac{\pm p}{R_w} + q - p + 2}{q - p + 6}.$$

With the disk geometry, we can easily find the $\phi_{geo}$, the angle between the line linking the disk top (at $\phi_s = 0$) and the hole and the line connecting $\phi_s$ where the emitting matter is located and the hole. It is obvious that, if

$$\phi_c(\phi_s) > \phi_{geo}(\phi_s), \tag{2.36}$$

the photon will be absorbed by the disk. From $B = B(\phi_s)$, we can identify the values of $\phi_s$ at which the eclipse occurs and terminates.

### 2.5.3 A brief discussion of the rotation law of disks

Let us now return to the rotation law of the surface of the disk. For a very thick disk, the dependence of angular velocity on radius is complicated. It has to be found from the analysis of equilibrium distributions of a fluid in the field of black holes (Kozlowski et al 1978). For a perfect fluid, the models have been constructed in both fully general relativistic and a pseudo-Newtonian framework ( Jaroszynski et al 1980, Paczynski and Wiita 1980, Abramowicz et al 1980) by using a macroscopic approach based on conservation laws and stability requirements. All uncertainties of microphysics (e.g. viscosity processes) are absorbed in two *a priori*

assumed structural functions — the surface distributions of the specific angular momentum and of the flux of the radiation.

It can be shown that the inner edge of the disk $r_{in}$ should be located between the marginally bound ($r_{mb} = 4M$) and marginally stable ($r_{ms} = 6M$) circular orbits, and that the disk becomes thicker with $r_{in}$ approaching $r_{mb}$. Here we choose to adopt the fully general relativistic model, because we also take into account all the relativistic effects in the case of the motion of photons. According to Jaroszynski, et al., the shape of a thick disk around a Schwarzschild black hole is given by *a priori* assumed distribution of the specific angular momentum $\ell(r) = \ell_d(r)$.

For simplicity, we confine ourselves to the simplest case of

$$\ell_d(r) = const. = \ell_K(r_{in}) = \frac{r_{in}^{3/2} M^{1/2}}{(r_{in} - 2M)}, \tag{2.37}$$

where $r_{in}$ is the inner edge of the disk where the matter moves along a circular geodesic orbit. For $r_{in}$ close to the marginally bound orbit at radius $r_{mb} = 4M$, we obtain a thick disks, with both $\theta_w = \theta_d(r) = const$ and $R_w$ governed by the value of $r_{in}$. In this case, the angular velocity on the surface of the disk is given by

$$\Omega_d(r) = \frac{\ell_K(r_{in})(1 - \frac{2M}{r})}{r^2 \sin^2 \theta_w},$$

and, if we restrict ourselves to very thick disks with $r_{in} \approx r_{mb}$, we can approximate the angular velocity of a spot on the surface of the disk by

$$\Omega(r) = \frac{4M(1 - \frac{2M}{r})}{r^2 \sin^2 \theta_w}. \tag{2.38}$$

For a slim or a thin disk, $\theta_w$ is close enough to $\theta = \frac{\pi}{2}$, the disk can be considered to be almost Keplerian and the angular velocity can be approximated

by the "Keplerian" formula ($\sin^2\theta_w \simeq 1$)

$$\Omega(R) = (\frac{M}{r^3 \sin^2\theta_w})^{1/2}. \tag{2.39}$$

### 2.5.4 Some general results

In the following, we take $\theta_w$ and $R_w$ as free parameters and use a numerical code based on the formulae derived in the second section.

First, we show how the shape of the light curves depends on the geometry of the disk and the viewing angle of the observer.

Fig. 2.13 shows light curves of a spot at $r_s = 6r_g$ versus the observer's time for different viewing angles $\theta_o = 70^o, 75^o, 80^o$, and different disk top $R_w = 12.5r_g$ and $R_w = 10r_g$, with the black hole mass $M = 10^6 M_\odot$. The shape of these light curves is different from the case of the Keplerian disk with $\theta_w = 90^o$ in which a peak plus a shoulder is distinct. As $R_w$ increases, the eclipse region gets larger and the light curve appears sharper. The eclipse region also depends on the viewing angle of the observer. As $\theta_o$ decreases, the region gets smaller and the light curve has a tendency to become wider, because the gravitational focusing plays a less important role when the viewing angle becomes smaller. The light curves show similarities to the folded EXOSAT light curve of Seyfert galaxy NGC 6814, which suggests the existence of an eclipse in this source.

Fig. 2.14 illustrates the light curve of a spot versus the orbital position. The solid line shows the observed light curve and the dotted line shows that without eclipse. The upper panel represents the Doppler boosting induced light curve and the lower one the gravitational focusing induced curve. The disk has its top at $R_w = 250r_g$. The spot is located at $25r_g$, the disk opening angle is $\theta_w = 80^o$

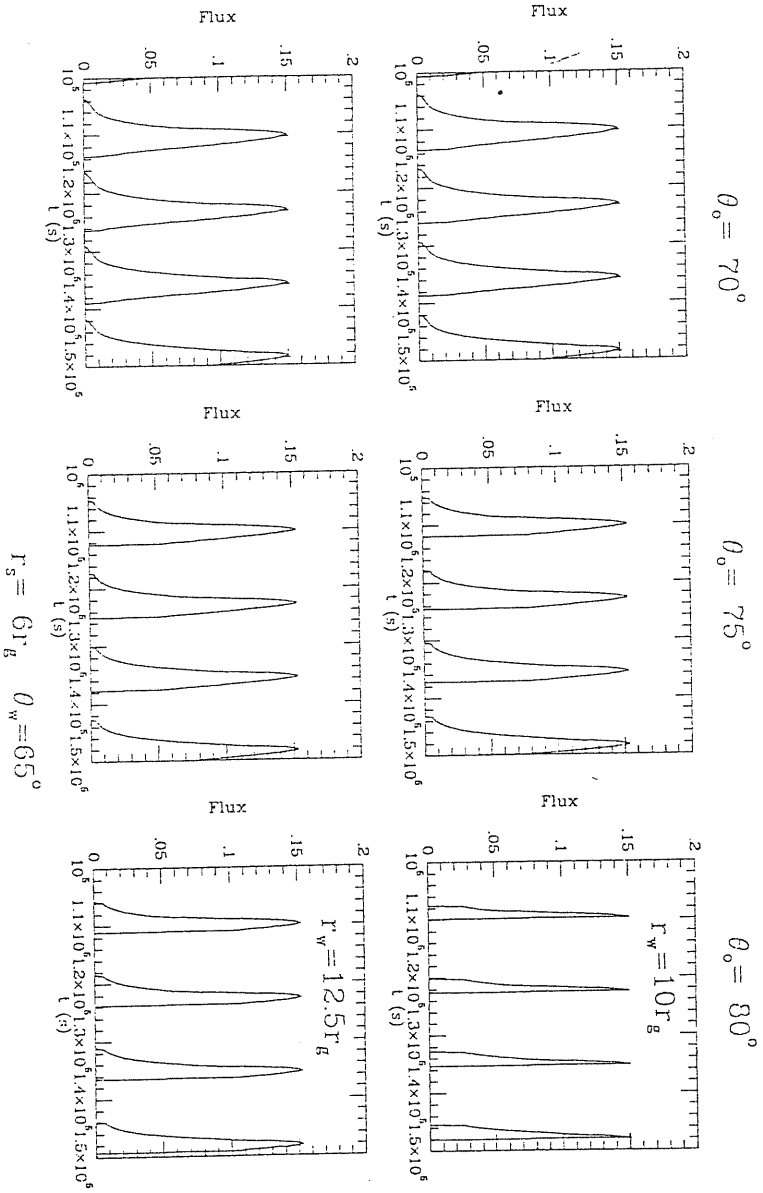


**Figure 2.13.** The light curves for different viewing angles $\theta_o = 70^o, 75^o, 80^o$, and different disk top $R_w = 12.5r_g$ and $R_w = 10r_g$. The black hole is assumed to have $M = 10^6 M_\odot$. The units for flux are arbitrary.

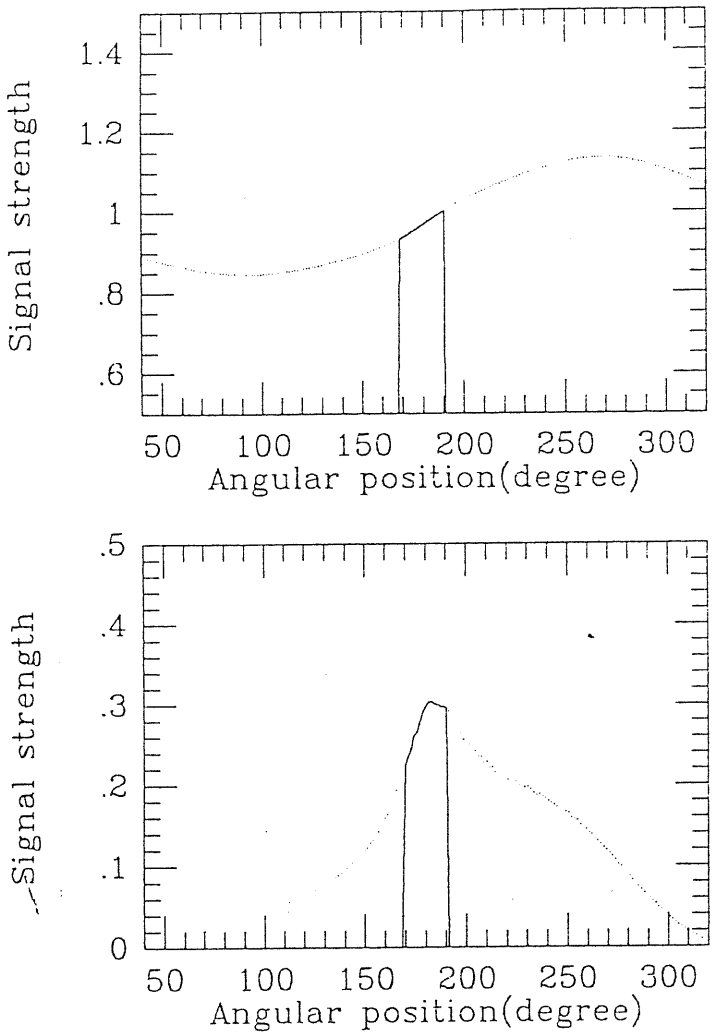


**Figure 2.14.** The light curve versus the orbital position. The solid line shows the observed light curve and the dotted line shows that without eclipse. The upper panel represents the Doppler boosting-induced light curve and the lower one the gravitational focusing-induced light curve. The units for flux are arbitrary.

and the viewing angle of the observer is $\theta_o = 81^o$. The two cases exhibit different

structures at the top of the signal: the one due to the gravitational lensing has a peak in the middle (i.e. the eclipse occurs symmetrically around orbital phase $\pi$) while the one due to the Doppler boosting has it on the right.

Figure 2.15 shows the part of the disk which can be seen by a distant observer. Bending of light rays enables the observer to receive radiation from the region which extends closer to the black hole than it does when this effect is ignored.

### 2.5.5 Conclusion

- Analytic methods of calculating light curves due to a spot corotating with a relativistic disk are derived. The methods are not dependant on the special geometry of the disk considered here;
- An analytic condition of photon–eclipsing is obtained;
- The shape of the light curve from a spot relies strongly on the geometry of the disk and the inclination angle to the observer. The eclipse due to the disk geometry clips the flares into a sharp peak. The shape and the width of the light curve can be employed as a sensitive " diagnostic instrument"to determine the geometry of the system;
- The difference between the Doppler boosting induced light curves and the gravitational lensing induced ones lies in the structure of the top of the flare. The lensing induced curve has its maximum at the center, while the one due to the Doppler effect always has it on the right.

Part of the work presented in this chapter is adapted from

Bao, *Astron. Astrophys*, 1992,

Bao and Stuchlik *Ap. J.*, 1992,

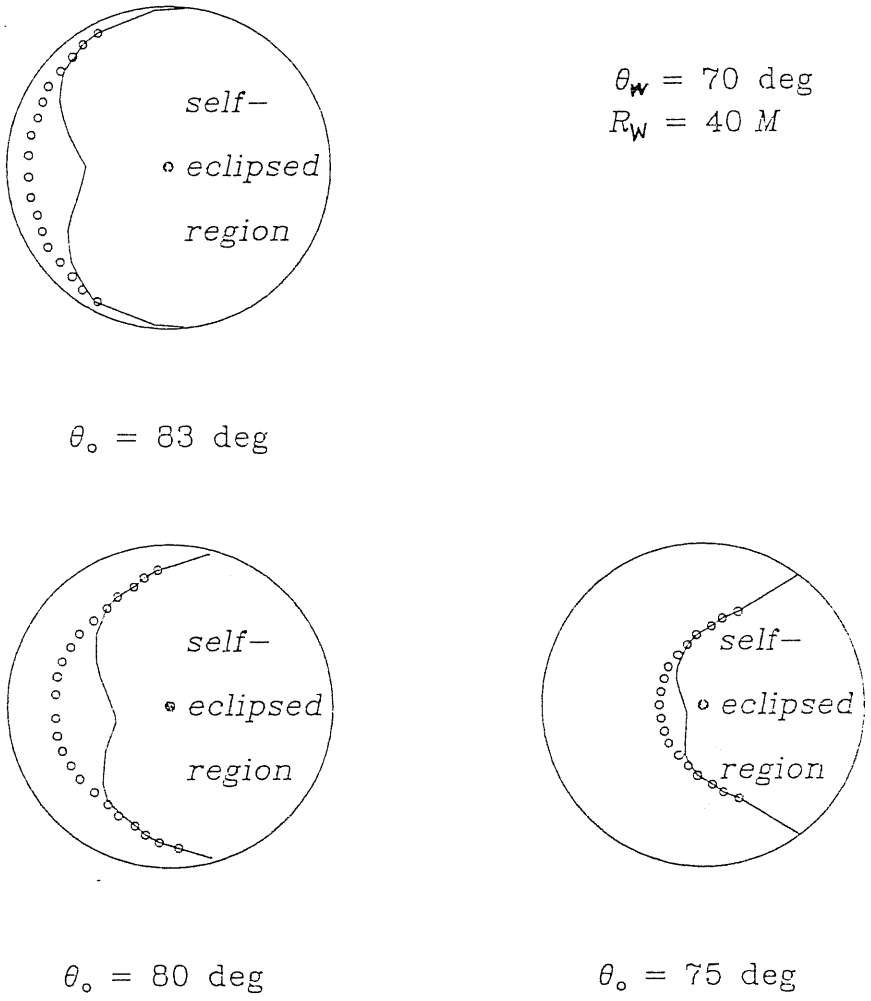


**Figure 2.15.** The visible and self-eclipsed region of the disk for the three values of the viewing angle $\theta_o$. The circle in the centre of each figure denotes the horizon of the hole. The large circle is the projection of the disk's outer edge, $r = R_\omega$, as viewed from above (along the common symmetry axis of the disk and the black hole). The observer is located on the right-hand-side of the figure, far from the disk. The full curve is the border of the self-eclipsed region in our model, and the small circles denote the location of this border when gravitational focusing is ignored.

Karas and Bao *Astron. Astrophys*, 1992.

# Chapter 3

# The Variability Power Spectrum Due to Orbiting Spots

## 3.1 Introduction

In order to examine more closely the nature of flux variation with the time, especially to search for a characteristic time scale, the power spectrum technique is widely used in data analysis (e.g. Lawrence et al 1987, McHardy and Czerny 1987, Barr et al 1988; Pounds and Turner 1988; Tagliaferri et al 1991).

Here, we discuss the variability power spectrum due to the orbital motion of spots. Both classical and fully relativistic approaches are adopted. The non-relativistic treatment can supply us with a direct knowledge, i.e. the analytic expression of variability power spectrum, while the fully relativistic treatment may derive the results more close to the real situation when the system has a large inclination angle, and the photon emitted region is near the central black hole. As a result of the random distribution of spots on the disk, the observed X-ray intensity will have components at the orbital frequencies of all the spots present which range from $10^{-2} \sim 10^{-5}$ Hz. The envelope of the overlapping power spectrum profiles due to individual spots will yield a broad feature in the observed

power spectrum.

The instabilities work most efficiently in the inner disk. The disk is smoother as one moves out radially, which gives a cut-off frequency at the lower end where there are fewer spots on the disk surface. In principle, the inner edge of the disk introduces a cut–off at high frequencies end. The variability could be affected by the rotation of the disk, the brightness of the spot, and the number density of spots within the two cut–offs, but less strongly outside the frequency range. We therefore expect the variability power spectrum to take different shapes as the two frequencies are crossed. For galactic X-ray sources, the variability power spectrum has the "knee" frequency at the lower end and the feature of QPO (quasi–periodic oscillation) frequency at higher end (Makishima 1988). For AGN, on the other hand, the data are not sufficiently good and complete to offer any valid information about either of the cut–offs. Probably, we may still observe variability between these two frequencies.

There exists a possibility that a very bright spot or a few spots occasionally appear from a narrow region of the disk. In this case, the observed light curve shows periodic flares due to the Doppler effect and the gravitational lensing –a phenomenon which may have been detected during the *EXOSAT* observation of Seyfert Galaxy NGC 6814.

When the disk is seen almost face-on (at a small viewing angle), the observed variability may only reflect the intrinsic changes of intensity due to the non-axisymmetry property of the disk, whereas when the disk is seen at a large viewing angle, the intrinsic variability amplitude and local non-uniform effects will be amplified by the Doppler effect and the gravitational lensing.

The spot production and decay processes might themselves deserve some de-

tailed and rigorous analysis. However, assuming that these processes are known already, we will concentrate only on how spot statistics, the orbital motion, the inclination of the disk and the gravitational lensing effect contribute to the variability patterns.

In this chapter, we reveal various behaviors of the variability power spectrum due to spots. Section 2 introduces some basic formulae of variability power spectrum. A mathematical explanation for the "scale-invariant" behavior is given in section 3. Section 4 and 5 show the results obtained through weak field approximation. A general behavior of the variability power spectrum is described there. Section 6 discusses the influence of the full relativistic effect on the variability power spectrum.

## 3.2 The variability power spectrum

Before analysing the variability power spectrum resulting from the corotating spots, it is worth introducing a few basic theoretical concepts. For detailed knowledge, see Rice (1954).

Suppose we have a signal $F(t)$ which extends from time $t = 0$ to $t = \infty$, the autocorrelation function $\psi(\tau)$ of $F(t)$ is defined as

$$\psi(\tau) = \lim_{T\to\infty} \frac{1}{2T} \int_{t_1}^{t_1+T} F(\tau)F(\tau + t_o)dt_o, \tag{3.1}$$

where the limit is assumed to exist ( $t_1$ is arbitrary for stationary process). The power spectrum is related to this function through

$$P(\omega) = 4\int_0^\infty \psi(\tau)\cos\omega\tau d\tau. \tag{3.2}$$

Further, we can write the power spectrum of $F(t)$ in terms of its Fourier transform $S(\omega)$,

$$P(\omega) = \lim_{T\to\infty} \frac{1}{2}\frac{|S(\omega)|^2}{T}, \tag{3.3}$$

where

$$S(\omega) = \int_0^T F(t)e^{i\omega t}dt. \tag{3.4}$$

If the lifetime of spots was finite, there would be many spots during $T$, and there would also be many spots at any given time. For many spots, we must add the contributions from all of these spots,

$$P(\omega) = \frac{1}{2}\lim_{T\to\infty}\frac{1}{T}\sum_i |S(\omega; r_i, \phi_i, t_i)|^2, \tag{3.5}$$

where $S(\omega; r_i, \phi_i, t_i)$ is the Fourier transform of $F_i(t)$ for the $i^{th}$ spot created at the location $(r_i, \phi_i)$ and time $t_i$. The summation is over all spots appearing during time $T$. If we consider the spots creation process to be stationary and spots created at the same radius to be identical and factor out the constant part of the redshifted intensity from $S(\omega; r_i, \phi_i, t_i)$, and if we convert the summation into integration by introducing the probability function $n(r, \phi_i)$ of the average number of spots created at radius $r$ and azimuthal angle $\phi_i$ on the surface of the disk, then we can write the power spectrum $P(\omega)$ as

$$P(\omega) = \frac{1}{2}\int \frac{I(r)^2}{\tau}|S(\omega; r_i, \phi_i, t_i)|^2 n(r, \phi_i)drd\phi_i. \tag{3.6}$$

## 3.3 The variability of "timescale–invariant"

After over 20 years of accumulation of observational data from different satellites, especially from the "long looks" of EXOSAT, it is found that in the energy

range of 2–10 KeV, the energy flux of most samples varies at all timescales. The variability shows no feature in most cases and its power spectrum appears in a power-law shape, $P(\omega) \sim \omega^{-\beta}$ at the frequency range of $10^{-5} - 10^{-3}$ Hz (Pounds and McHardy 1988). The power law index $\beta$ is in the range of 1–2. The power spectra of high energy X-ray from the galactic black hole candidate Cyg X–1, the neutron star binary and the low mass X-ray binaries(LMXBs) also exhibit the same power law behavior in the frequency range 0.1–10 Hz. These frequencies scale roughly with the mass.

The power–law behavior means that the variability of ANG in the observed frequency range is self-similar, timescale–invariant, or short of characteristic timescale. The possible exception to this behavior is NGC 6814 whose power spectrum has several peaks.

To understand the self-similar behavior, let us first consider the timescale-invariant power spectrum $P(\omega)$, which requires that (Makishma 1988)

$$< p(R\omega) >=< c(R)p(\omega) > \tag{3.7}$$

This should be held for any positive number R and positive value $\omega$. In formula (3.7), c(R) is a positive function, and with the condition $c(1) = 1$, the <> refers to the ensemble average. Take a logarithm of formula (3.7) and let

$$P(\omega) =< lnp(\omega) > \tag{3.8}$$

and

$$C(R) =< lnc(R) >, \tag{3.9}$$

then it can be written as

$$P(R\omega) = C(R) + P(\omega). \tag{3.10}$$

Again let

$$R = 1 + x, \tag{3.11}$$

where x is an infinitesimal variable, (3.10) becomes

$$x\omega P'(\omega) = C(1) + xC'(1). \tag{3.12}$$

Then let $\beta = -C'(1)$, we obtain

$$P'(\omega) = -\beta/\omega, \tag{3.13}$$

where $C(1) = 0$ is used.

Integrate (3.13) we obtain

$$P(\omega) = -\beta ln\omega + b,$$

where $b$ is the arbitrary constant. Let $B = e^b$,then

$$< p(\omega) >= B\omega^{-\beta}, \tag{3.14}$$

so the power spectrum is in the shape of a power–law.

A self-similar variation has several peculiar properties: the power would diverge at high frequency limit if $\beta < 1$, at low frequency limit if $\beta > 1$ and at both limits if $\beta = 1$. Since the actual variance should not diverge, we expect $\beta > 1$ at sufficiently high frequency and $\beta < 1$ at sufficiently low frequency.

## 3.4 The multi-peaked variability power spectra

### 3.4.1 The formula

A spot with the observed intensity $I_{obs}$ which occupies a solid angle $\Delta\Pi$ has the observed energy flux

$$F_{obs} = I_{obs}\Delta\Pi.$$

The intensity of light $I_{obs}$ is

$$I_{obs} = g^4 I_s. \tag{3.15}$$

$g$ is the redshift factor and has the form of

$$g = (1 - v\sin i\sin\phi_s)\gamma, \tag{3.16}$$

where $i$ is the inclination angle of the orbit, $\phi_s$ is the angular position of the spot in the orbit, $\gamma$ is Lorentz factor, $v$ is the speed of the spot in unit of $c$, and $c$ the speed of light. In the calculation, we choose to neglect the gravity and take it for granted that photons go in a straight line– a reasonable approximation when the lensing effect is not important (Zhang and Bao 1991, Bao 1992). What is more, the approximation not only makes the analytic calculation of the power spectrum possible, but also provides insights into the basic properties of the spectrum.

We can relate $\phi_s$ to the signal arrival time by

$$\phi = \Omega(t + \Delta t), \tag{3.17}$$

where $\Delta t$ is the time delay with which a distant observer receives the light rays from two different orbital positions when the spot moves at relativistic speed, and $\Omega$ is the angular velocity of spot. Simple geometrical considerations give (see Fig. 3.1)

$$\Delta t = -\frac{v}{\Omega}\cos\phi_s\sin i. \tag{3.18}$$

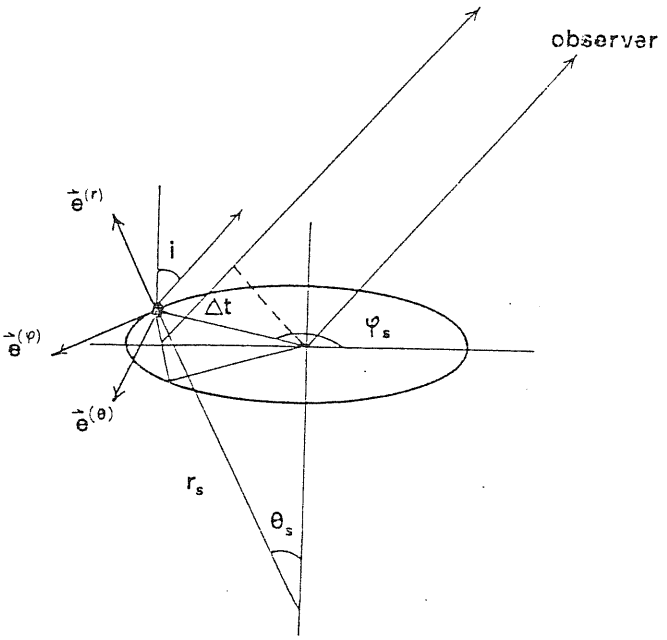


**Figure 3.1** Illustration of a spot on the orbit $(r_s, \theta_s)$ at orbit position $\phi_s$. The spacial legs of the orthonormal frame carried by the spot are $(e^{(r)}, e^{(\theta)}, e^{(\varphi)})$. The orbital plane is inclined at angle $i$, and the difference in travel time for a photon emitted at a particular orbit position (as compared with photons emitted at orbital center) is $\Delta t$.

The spot is not visible for $\phi_s$ in the range

$$-\phi_e < \phi_s < \phi_e,$$

where $\phi_e$ is the eclipse phase of the orbit by the outer part of the disk. For a spot of infinitely long life, the resulting light curve will be

$$F_{obs} = I_s \Delta\Pi (1 - v \sin i \sin \phi_s)^4 \gamma^4, \tag{3.19}$$

$$-\phi_e < \phi_s - 2n\pi < 2\pi - \phi_e,$$

$$n = ..., -1, 0, 1....,$$

and if $\phi_s$ is outside that range, the flux will be zero.

The distributed portion of the power spectrum of the signal is (Rice 1954)

$$P(\omega) = 2\mu |s(\omega)|^2, \tag{3.20}$$

where

$$s(\omega) = \int_{-\infty}^{\infty} e^{-i\omega t} F(t) dt$$

is the Fourier expansion of the individual intensity and $\mu$ is the characteristic rate of spots appearance, which depends on the radius of the considered spot. In our case, the final power spectrum is

$$P(\omega) = 2\mu \int_0^{2\pi} \rho(\phi) |s(\omega)|^2 d\phi, \tag{3.21}$$

where $\rho(\phi)$ is the probability distribution function of the initial phase from which the spots start to contribute to the luminosity. For axisymmetric distribution,

$$\rho(\phi) = \frac{1}{2\pi}.$$

For simplicity, we assume the time delay effect to be so small that can be ignored. It will be seen later( next section ) that this does not change the basic structure of the calculated power spectrum. The individual intensity is therefore

$$F(t) = I\Delta\Pi g^4(t)\theta(t)e^{-\frac{t}{\tau}}G(t), \tag{3.22}$$

where

$$g = (1 - v\sin i\sin(\phi_s + \phi_i))\gamma,$$

and $\phi_i$ is the initial phase of the $i$th spot from which the spot starts to contribute to the luminosity. $\theta(t)e^{-\frac{t}{\tau}}$ is the life time envelope, that is, the spot suddenly appears and then exponentially decays. $G(t)$ is the square wave function due to the eclipse and can be written in Fourier series

$$G(t) = 1/2\sum_{n=-\infty}^{\infty} b_n e^{in\Omega t}, \tag{3.23}$$

where

$$b_n = \begin{cases} \frac{-2\sin(n\phi_e)}{n\pi}, & \text{n} \neq 0; \\ \frac{(\pi-\phi_e)}{\pi}, & \text{n=0.} \end{cases}$$

We notice that in the calculation, all terms with $e^{i\phi}$ have zero averages, in other words, the interference terms do not contribute to a randomly–phased average. So from formula (3.19)–(3.23), we obtain

$$P(\omega) = 2\mu\tau^2 I_s^2\Delta\Pi^2\gamma^8\sum_{j=-4}^{4}\frac{c_j^2\varepsilon_j(\phi_e)}{1+\tau^2(j\Omega-\omega)^2}, \tag{3.24}$$

where

$$\varepsilon_j = A_j^2 + B_j^2;$$

$$A_j = \frac{\pi-\phi_e}{2\pi} - \frac{me+df}{e^2+f^2};$$

$$B_j = \frac{mf - ed}{e^2 + f^2};$$

$$m = sh(\frac{\pi - \phi_e}{\Omega\tau}) \cos(\frac{(j\Omega - \omega)(\pi - \phi_e)}{\Omega});$$

$$d = ch(\frac{\pi - \phi_e}{\Omega\tau}) \sin(\frac{(j\Omega - \omega)(\pi - \phi_e)}{\Omega});$$

$$e = sh(\frac{\pi}{\Omega\tau}) \cos(\frac{(j\Omega - \omega)\pi}{\Omega});$$

$$f = ch(\frac{\pi}{\Omega\tau}) \sin(\frac{(j\Omega - \omega)\pi}{\Omega}); \qquad (3.24a)$$

$$c_0 = 1;$$

$$c_1 = c_{-1} = -2v_i;$$

$$c_2 = c_2 = -3/2v_i^2;$$

$$c_3 = c_{-3} = v_i^3/2;$$

$$c_4 = c_{-4} = v_i^4/16;$$

$$v_i = v \sin i.$$

### 3.4.2 Discussions

Some important properties can be derived from formula (3.24) and (3.24a). When the lifetime of the spots is long enough, the power spectrum shows distinct peaks at

$$\omega = n\Omega,$$

where $n = 0$ corresponds to the red noise caused by time variations in the photon arrival rate. The presence of this noise follows from the fact that the mean X-ray intensity contributed by each spot is positive.

All spots that contribute to the luminosity also contribute to the red noise. The power density of this component of the spectrum is almost constant at the frequency

$$\tau\omega < 1,$$

but rolls off at high frequencies and gives a red spectrum. The terms related to $j\Omega - \omega$ describe the power density near $j\Omega$, the orbital frequency and its overtones. The absolute strength of the first four peaks is proportional to $v_i^{2j}; j = 1, 2, 3, 4$ and that of the rest to the combinations of even power of $v_i$. It is obvious that these four main peaks are the direct results of the formula (3.15) where the fourth power is present. It is therefore concluded that the main peaks result from the relativistic effect on the propagation of photons. Fig. 3.2 shows the power spectra for $v_i = 0.3$, $\phi_e = 2$ (in the unit of radius), and for different lifetime of spots. As $\tau$ increases, the peaks in the spectrum are more distinct.

It is understood that, firstly, the peaks in the theoretical power spectrum are proportional to the speed of spots. When the speed of a spot is zero (suppose that the viewing angle of the observer is not zero), there are no distinct peaks in the power spectrum except red noise($c_1 \neq 0$). The greater the velocity, $v$, of the spot is, the more distinct the peaks are in the power spectrum. Secondly, the strength of the peaks does not depend on the first order or any odd order of velocity, because the power density of the intensity does not relate to the direction of the rotation of the spot. Fig. 3.3 shows the power spectra of $\phi_e = 0.5, \tau = 5 \times 10^5$s for different projection velocities $v_i$. The absolute strength grows with the increase of $v_i$. It is

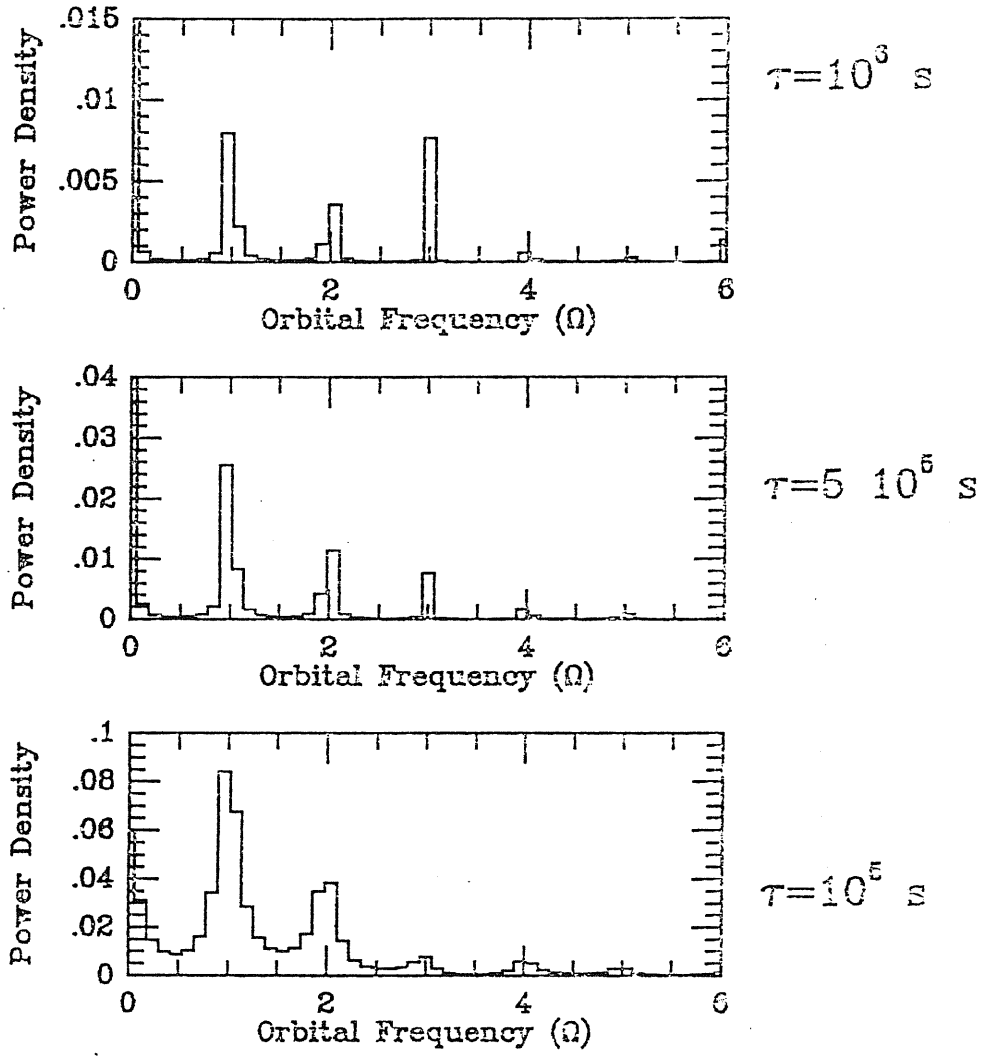


**Figure 3.2**. The power spectra for different lifetimes of $\tau = 10^5 s, 5 \times 10^5 s$, and $\tau = 10^6 s$. The eclipse phase and the projection velocity for the three cases are $\phi_e = 2.0$, $v_i = 0.3$.

interesting that the relative ratios remain the same in this situation.

When the viewing angle of the observer is larger than the disk opening angle,

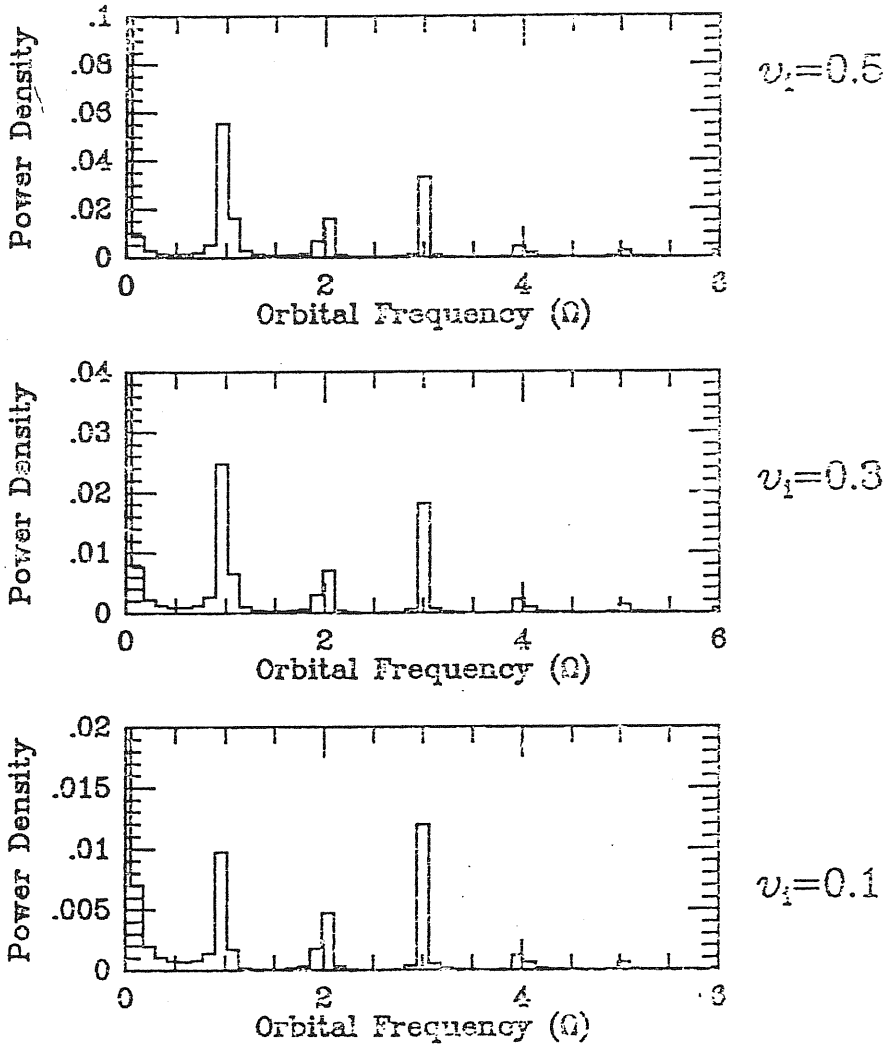


**Figure 3.3.** The power spectra for different projection velocities of $v_i = 0.1, 0.3,$ and $v_i = 0.5$. The eclipse phase and lifetime of spots for the three cases are $\phi_e = 0.5, \tau = 5 \times 10^5$ s.

some part of the disk will be obscured by the outer part. This could be a case common to X-ray sources. Fig.3.4 presents the power spectrum for $\tau = 5 \times 10^5$,

the projection velocity $v_i = 0.3$, and for different eclipse phases $\phi_e$. The relative strength of each peaks is strongly modulated by the eclipse. In the non-eclipsing case, however, $\varepsilon(\phi_e)$ is constant and the relative height of the peak depends solely on the coefficient $c_j$, i.e. the projection velocity. The ratio of the peaks $k$ and $l$ is

$$R = (\frac{c_k}{c_l})^2.$$

If we consider the peak at fundamental ($k = 1$) and at the first harmonic ($l = 2$), and suppose that the projection velocity $v_i = 0.3$, then

$$R \sim 20.$$

As is shown in Fig. 3.4, most of the power is contained in the peak at fundamental. Eclipse introduces fast variation in the signal, which drives more power into the harmonics. If the spots scatter over a wide range of the disk, this effect will flatten the variability power spectrum. In this case, the creation rate of the spot $\mu$, the life time of the spot $\tau$, and the emissivity of the spot $I_s$ are a function of $r$ at which the spot locates.

The power spectra are constructed from the whole effective area of the disk,

$$P(\omega) \sim \sum_{j=-4}^{4} \int_{r_{in}}^{r_{out}} \mu\tau^2 I_s^2 \Delta\Pi^2 \gamma^8 \frac{c_j^2}{1+\tau^2(j\Omega-\omega)^2} \varepsilon(\phi_e) dr, \qquad (3.25)$$

when $\tau$ is large enough. And if we only consider the power near $j\Omega, j = 1, 2, 3, 4$, then

$$P(\omega) \sim \sum_{j=1}^{4} \mu(r)\gamma^8 \tau(r)^2 I_s(r)^2 \Delta\Pi(r)^2 c_j(r)^2 \frac{dr}{d\Omega} (\phi_e(r) - \pi)^2. \qquad (3.26)$$

Apart from the extra term $(\pi - \phi_e)^2$, the formula (3.26) is the same as what we have derived before (see the next section), although a different life time envelop is employed here. The power spectrum can be expressed as

$$P(\omega) \sim \omega^{-\beta+\alpha},$$

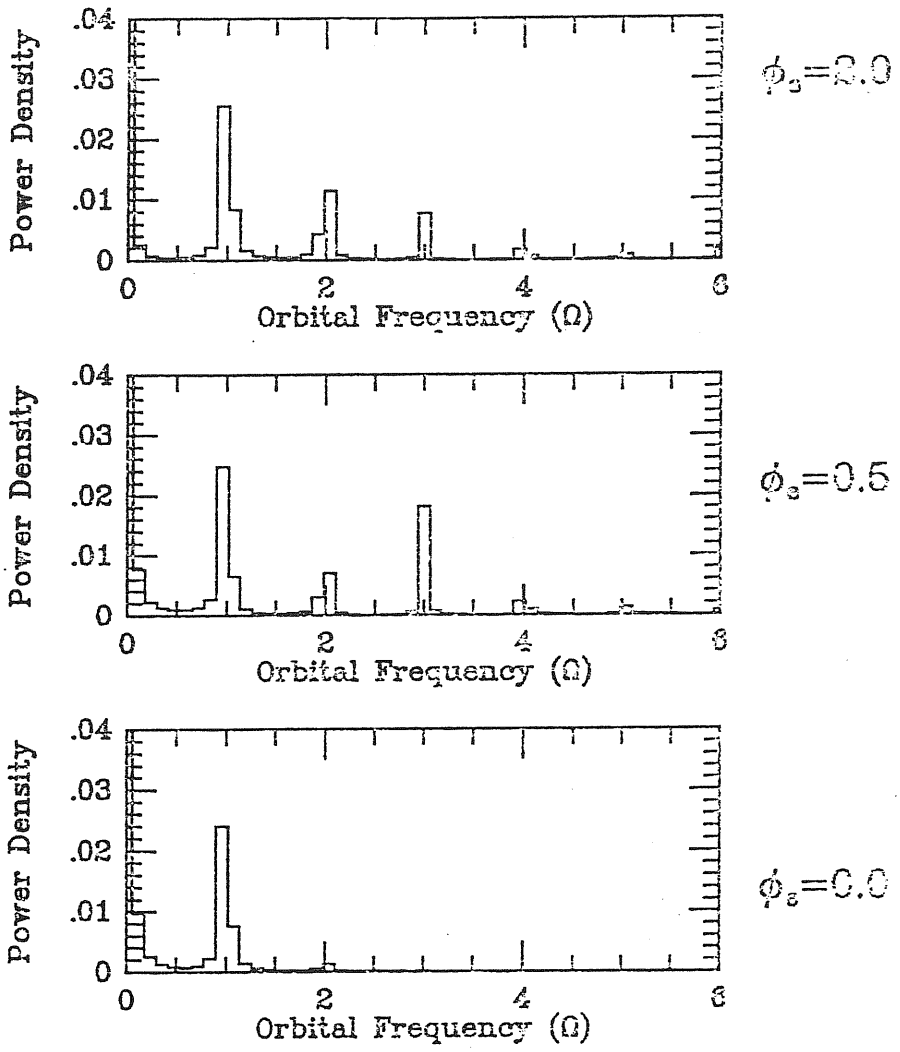


**Figure 3.4.** The power spectra for different eclipse phases $\phi_e = 2.0, 0.5$, and $\phi_e = 0.0$. The lifetime and projection velocity for the three cases are $\tau = 5 \times 10^5 s$ and $v_i = 0.3$.

where $\beta$ has the same meaning as that of Zhang and Bao (1991) (see the next

section), and $\alpha$ contains the contribution from eclipse. We can assume that

$$\phi_e \sim r^{-\alpha_e},$$

that is, the deeper the spot is located, the larger the eclipse phase becomes. For a disk with rotation law $\Omega \sim r^{-\alpha_\Omega}$,

$$\phi_e \sim \omega^{\frac{\alpha_e}{\alpha_\Omega}},$$

then

$$\alpha \sim 2\frac{\alpha_e}{\alpha_\Omega}.$$

The eclipse always flattens the variability power spectrum, because the short timescale variations are involved.

Finally, to some extent, the observed relative strength of the peaks yields valuable information about the velocity of the innermost disk, the viewing angle of the observer, the eclipse phase of the orbit, and the average lifetime of the spots.

It should be mentioned that when the photon moves in a strong gravitational field, there will be faster variation in the X-ray intensity due to the lensing effect.

### 3.4.3 Conclusion

- If the "clumps", i.e, spots, appear in a narrow range of the disk, their intensity shows periodic flares due to the rotation of the disk which corresponds to multi–peaked variability power spectrum.
- The first four peaks in the spectrum result from the relativistic effect on the propagation of photons.
- The ratios among the peaks are strongly modulated by the disk self-eclipse caused by the outer part of the disk. When the spots scatter over a wide

range, the eclipse always flattens the variability power spectrum due to the shorter timescale variation involved.

## 3.5 Variability power spectrum of many spots

We shall approximate the innermost X-ray producing region of the accretion disk as consisting of two components: $L_D$ due to a steady and axially symmetric disk and $L_s$ due to the contribution from all the spots,

$$L = L_D + L_s. \tag{3.25}$$

The time and angle averaged $L$ could be computed from a disk model. The spots are assumed to have average values as functions of the radius for their brightness, $I_o(r)$, lifetime, $\tau(r)$, and the number of spots per unit interval of radius, $n(r)$. The explicit functional forms for these quantities should be given by a specific model describing the intrinsic variability. When $\tau(r)$ is longer than a few orbital periods, observations cannot easily differentiate different intrinsic variabilities with the same $I_o(r)$, $\tau(r)$, and $n(r)$. For this reason, we will not discuss any particular intrinsic variability here.

### 3.5.1 An analytic formula

In the following, we derive a general expression for the observed power spectrum for any given intrinsic variability, with the rotational effect included. It is straightforward though tedious, to show (Appendix A) that for axisymmetric

$n(r, \phi_o)$,

$$n(r, \phi_o) = \frac{1}{2\pi} n(r),$$

and for a (possible eclipsing )neutron star or Schwarzschild black hole system,

$$P(\omega) = \frac{1}{2} \int \frac{I_o^2(r)}{\tau(r)} n(r) p(r, \omega) dr$$

$$= \frac{1}{2} \int \frac{I_o^2(r)}{\tau(r)} n(r) \sum \alpha_N v_i^M J_N(K v_i)$$

$$\times G_{\omega - N_1 \Omega} G^*_{\omega + N_2 \Omega}. \tag{3.26}$$

In order to write (3.26) in a compact form, we use a few abbreviations. The full expressions are given in Appendix A. More specifically, $K, M, N, N_1, N_2$ are merely symbolic representations of some integers; $\alpha_N$ corresponds to the $N^{th}$ numerical expansion coefficient; $J_N(X)$ is the $N^{th}$ order Bessel function; $G_\omega$ is the Fourier transform of the evolution function $G(t)$ due to the intrinsic variability in the spot's own rest frame; and $G^*_\omega$ denotes its complex conjugate. The situations where $N = 0$ but $N_1, N_2 \neq 0$ will be seen only when there is an eclipse. It is also to be noted that $M + N$ is always an even number, which can be understood from the time reversal symmetry of the disk motion.

From this general expression, we can see that, as is expected, the resulting power spectrum is controlled by the rotation law $\Omega(r)$ of the disk and the radial dependence of the spot number density $n(r)$, the spot brightness $I_o(r)$ and the spot lifetime $\tau(r)$. In particular, for a ring of spots not observed face-on ($\sin i = 0$), in addition to the intrinsic variability ($G_\omega$), we can also see the rotation- induced variability ($G_{\omega - n\Omega}$). The strength of the repeated feature depends on the $2n^{th}$ power of the projected orbital speed of the spots on the ring, $(v_{orb} \sin i)^{2n}$, and the total intensity of all of these spots. When the spots are spread over a wide

range of radii, the rotation will introduce a broad feature into the power spectrum in the frequency range of the corresponding orbital frequencies.

To study further the effects of rotation and the statistics of spots on the observed variability, let us consider a simple case where

$$G(t;r) = \begin{cases} 1, & t_o < t < t_o + \tau(r); \\ 0, & \text{otherwise} \end{cases} \tag{3.27}$$

and treat the disk as being geometrically thin so that eclipse becomes negligible. We will also ignore the relativistic corrections to the orbital motion. Since typically, even for a Schwarzschild black hole,

$$v_i \ll 1,$$

this will not be a serious limitation even for black hole systems. Then as long as

$$\frac{1}{\tau} \ll \Omega,$$

we can approximate $G_\omega$ as

$$G_\omega \sim \frac{\sin\frac{(\omega-\Omega)\tau}{2}}{(\omega-\Omega)},$$

and the summation in (3.26) will be dominated by the first non-trivial terms (we are not interested in the $\omega = 0$ component here). Therefore, we have

$$P(\omega) \sim \int \frac{I_o^2(r)n(r)v_i^2}{\tau}\left(\frac{\sin\frac{(\omega-\Omega)\tau}{2}}{(\omega-\Omega)}\right)^2 dr$$

$$\sim \left[I_o^2(r)n(r)v_i^2\tau(r)\left(\frac{dr}{d\Omega}\right)\right]|_{\Omega=\omega}. \tag{3.28}$$

From this, we readily see that if $I_0(r), n(r)$, and $\tau(r)$ follow power-laws as functions of $r$,

$$I_o \sim r^{-\alpha_I}, n(r) \sim r^{1-\alpha_n}, \tau(r) \sim r^{\alpha_r}, \tag{3.29a}$$

and if the disk rotation can also be described in the power-law shape,

$$\Omega(r) \sim r^{-\alpha_\Omega}, \tag{3.29b}$$

then the resulting power spectrum $P(\omega)$ will also take a power-law shape,

$$P(\omega) \sim \omega^{-\beta} \sin^2 i, \tag{3.30}$$

where

$$\beta = 1 + \frac{2\alpha_I + \alpha_n - \alpha_\tau - 4}{\alpha_\Omega}.$$

One interesting consequence of (3.30) is that, for uniform radial distribution of the statistical properties of the spots ($\alpha_n = \alpha_\tau = \alpha_I = 0$) and for a keplerian disk ($\alpha_\Omega = 3/2$), the power spectrum has the form

$$P(\omega) \sim \omega^{-\frac{5}{3}} \sin^2 i. \tag{3.31}$$

It should be mentioned that while the simple power-law form (3.30) indicates roughly how the variability changes with the statistical properties of the spots and the rotation of the disk, it is obtained upon the omission of the eclipsing and the Lorentz factor of the orbital speed. If we return the Lorentz factor, (3.30) will no longer be in an exact power-law shape. It will then tend to be less steep close to the highest orbital frequency, because the actual contribution from the spots with higher orbital frequency is greater than when the Lorentz factor is ignored. It should also be noted that while (3.31) gives a definite number, $-5/3$, for the power-law index, it is obtained for an oversimplified and, perhaps, unrealistic spot population. In general, we tend to have fewer spots away from the inner edge of the disk ($\alpha_n > 0$), as is likely to introduce a flattening of the power spectrum at the low frequency end. We would also expect the variation in the disk surface

brightness be weaker and slower at larger distances ($\alpha_I > 0$),($\alpha_\tau > 0$). which would further flatten the power spectrum at the low frequency end. Concerning the rotation law, the disk is expected to be intermediate between a Keplerian disk ($\alpha_\Omega = 3/2$) and a constant specific angular momentum torus ($\alpha_\Omega = 2$). However, because of the lack of detailed studies of nonaxisymmetric and non-stationary accretion disks, it is largely unknown which values $\alpha_I, \alpha_a, \alpha_n$ will take. Some careful analysis of the time evolution of non-axisymmetric disks has to be carried out before any reasonable estimate for these statistical properties of the spots can be given.

### 3.5.2 Numerical simulations

To understand the effect of rotation and of the statistical properties of spots on the observed variability as shown by (3.26) and to avoid the limitations brought about by the assumptions on the spot motion leading to (3.30), we make some simple numerical simulations of light curves and estimate the power spectra directly from these simulated light curves. We consider the disk to be geometrically thin so that all of the spots are orbiting the central object in the equatorial plane. To generate these light curves, we first assign each spot a randomly selected creation time $t_i$. We then assign the initial positions $r_i$ of these spots randomly according to their average lifetime ($r$) and the average number of spots per unit interval of radius $N(r)$. The initial angular position is $0 < \phi_i < 2\pi$. The resulting light curve at time $t$ is found by summing the fluxes from all of the contributing spots, and the contribution from each spot is computed by using Eq. (3.19). 100 spots are used in our simulations. To simulate any possible instrumental noise or noise inherent to the signal, $L_D$ also contains a 10% noise contribution. The innermost orbit

($r_{in} = 10M$) is divided into 32 zones, and 4000 orbits are taken between $r_{in}$ and $r_{out}$. The outermost orbit considered is at $r_{out} = 80M$. Each orbit is divided uniformly, with each zone corresponding to approximately the same duration for all these orbits.

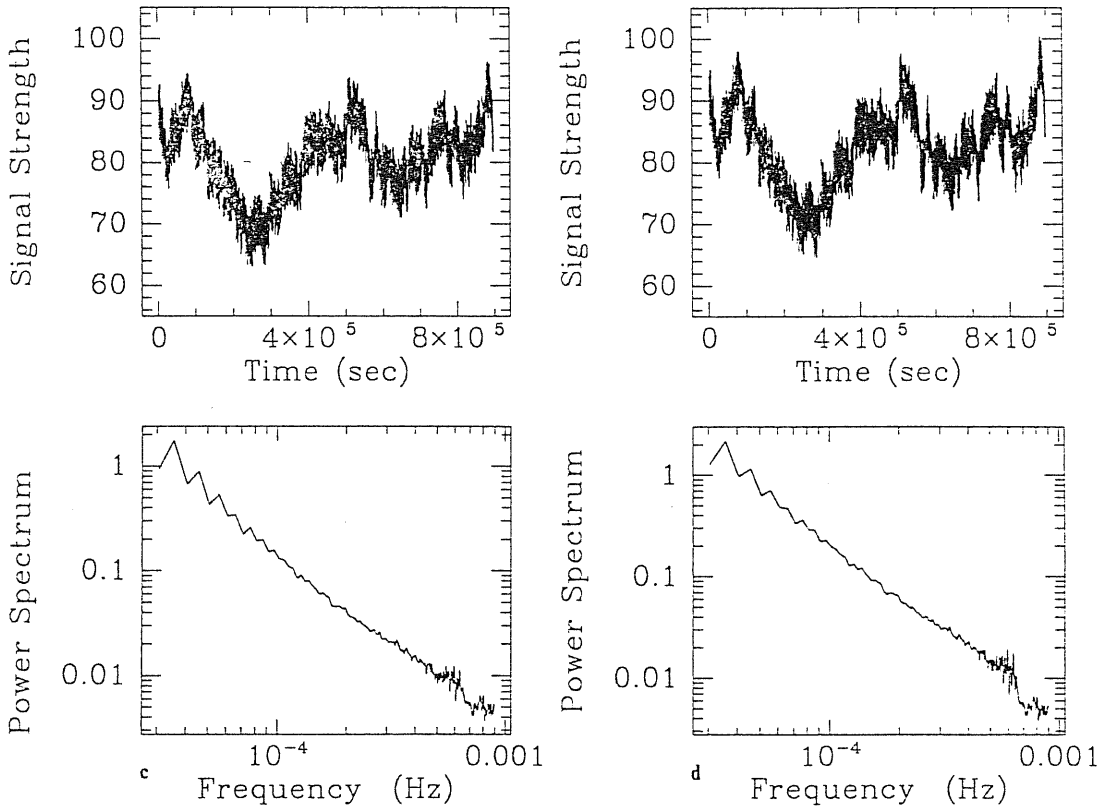


**Fig. 3.5c** and **5d** Simulated light curves (top) and the corresponding power spectra ( bottom) due to the same spot and disk configuration, but with increased inclination angle. For **c** (left), the inclination angle is 40°; and for **d** (right) 60°. Note that the logarithmic slope approaches −1.5 with an increasing inclination angle.

Fig. 3.5 shows the simplest case, with $G(t)$ taking the form (3.27). The lifetime $\tau$

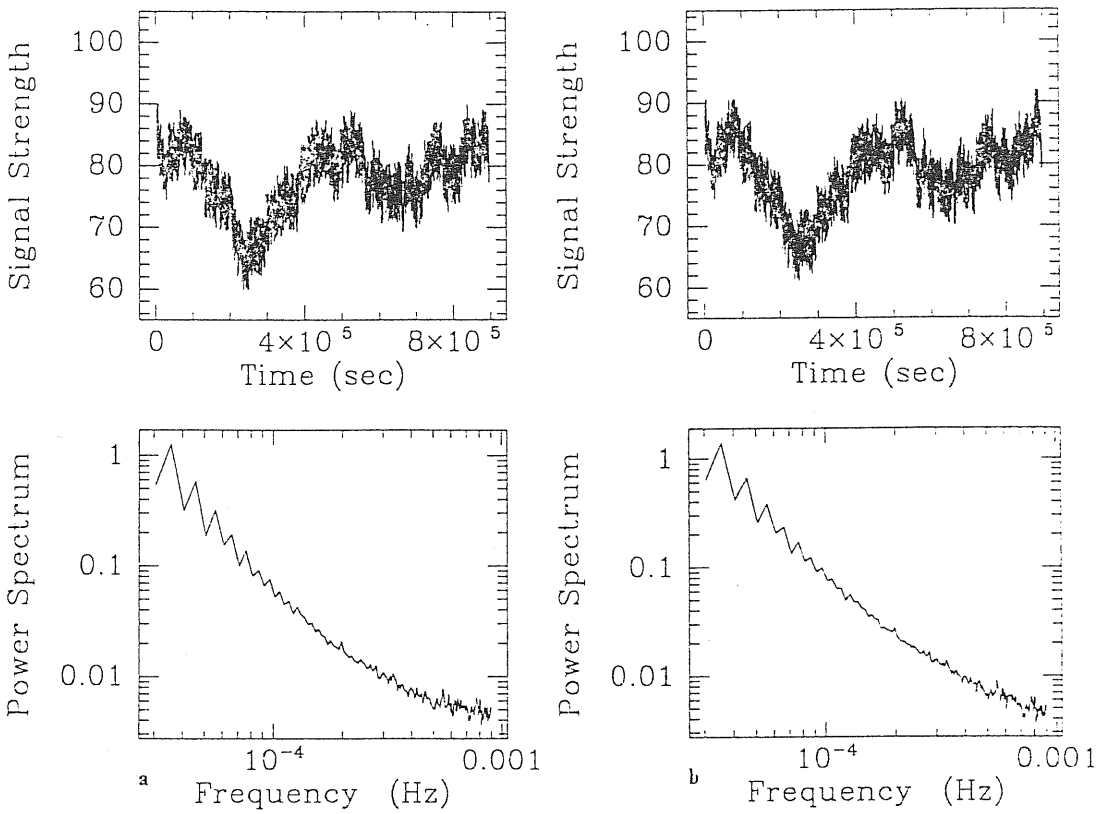


**Fig. 3.5a** and **5b** Simulated light curves (top) and their corresponding power spectra ( bottom). The results are gained from the calculations for 100 spots distributed uniformly between 10M and 80M on the surface of a Keplerian disk around $10^7 M\_odot$ black hole. Once created, a spot is taken to survive 4 times the orbital period of the outermost orbit, throughout which it retains a constant brightness. The ratio between the luminosities in the disk and in the spot component is $L_s/L_D = 3$ with a 10% noise contribution to $L_D$. The inclination for **a** (left) is $0^o$, and for **b** (right) $20^o$.

is the same for all of the spots and is chosen to be 4 times the orbital period of the outmost orbit. The spots are distributed uniformly on the surface of the disk and

have equal brightness. In Fig. 3.5a the disk is viewed face-on and no variability can be seen apart from that due to the switching on and off of the spots and that of the noise. In Figs. 3.5b, c, d, the effect of rotation gradually appears as the inclination angle $i$ increases: that part of power spectrum due to the spot rotation increases above the noise level and its shape changes until it reaches a power-law shape, $P(\omega) \sim \omega^{-1.5}$. Here the slight departure of $\beta$ from that predicted by (3.31) is basically due to the larger Lorentz factor and larger variation in the time delay at the smaller radii (i.e., at larger orbital frequencies). Note that, once it rises above the noise level and dominates the intrinsic part, the changed slope of the power spectrum is completely determined by the disk rotation and the statistical properties of the spots, while the inclination angle mainly controls the amplitude.

In Fig. 3.6, we use an $n(r)$ with a decrease in the surface number density of spots beyond $r \simeq 30M$ to modulate the tendency of the disk to be smoother at larger radii. All of the other parameters are the same as in Fig. 3.5. The inclination angle is $i = 60^o$. This simulation is made to demonstrate that the spatial distribution of spots will make a difference to the apparent variability when the disk is seen with a non-zero inclination angle. In particular, when there is a drop in the spot density beyond a certain radius, the power spectrum could be flattened below the corresponding orbital frequency.

Finally, to show that the observed variability can be different from the intrinsic variability, we give $G(t)$ the form of an exponential decay,

$$G(t) = \begin{cases} e^{-(t-t_i)/t_o}, & t > t_i; \\ 0. & \text{otherwise} \end{cases} . \tag{3.32}$$

Here the e-folding time $t_o$ is 4 times the orbital period of the innermost orbit ($\Omega(r_{in})t_o = 8\pi$). Therefore we would expect that the power spectrum be different near the highest orbital frequency but change little below $\Omega \leq 2\pi/t_0$. The rotation

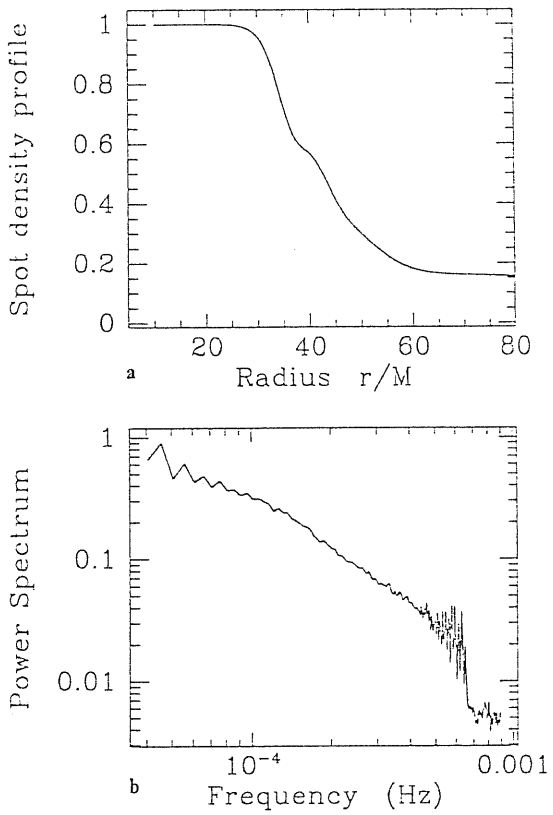


**Fig. 3.6a** and **3.6b** As the surface number density of spots falls below a certain radius, the power spectrum will be flattened below the corresponding orbital frequency. All the parameters used here are the same as in Fig. 3.5, except that a different radial dependence of spot density is adopted. **a** (top) shows the surface number density profile of the spots; **b** shows the variability power spectrum for an inclination angle $i = 60^o$. Note the flattening of the power spectrum at low frequency and the cut-off at the highest orbital frequency.

law is $\Omega \sim r^{-2}$ and is normalized so that the innermost orbit will have the same orbital frequency as a Keplerian one. Because of the shorter effective time of spots in this case and the limitation of computer capability, instead of keeping

the effective average number of spots on the disk surface constant, we here take $L_s/L_D = 50$. The range of radii is chosen to be from $r_{in} = 6M$ to $r_{out} = 50M$. It should be noted that the expression (3.27) does not quite apply to thin disks close to this $r_{in}$. The strong light bending and the consequent time delay will introduce a larger amplitude into the rotation-induced variability at the orbital frequency than that described by (3.27). In a subsequent work, these two important effects for thin disks around a black hole or for large inclination angles will be included in a fully relativistic treatment. Nevertheless, we here use (3.27) to compute the simulated light curve and demonstrate that, due to the relativistic orbital motion, the observed variability (Fig. 3.7b) will be different from the intrinsic variability (Fig. 3.7a), when the timescale of the latter is of a few orbital periods.

Finally, it is worth emphasizing that the orbital motion is likely to change the apparent variability unless the variability arises from some global changes and the variation is axisymmetric.

### 3.5.3 Discussion

We would like to comment briefly on the potential connections between the results presented here and the observations. It is found that for almost all of the sources, the power spectra of AGN X-ray light curves take a power-law shape, $P(\omega) \sim \omega^{-\beta}$. This is also true for galactic black hole candidates and low-mass-X-ray-binaries (LMXB's) (see chapter 1 and the proceedings edited by Treves 1987; see also Mittaz and Branduardi-Raymont 1989 and Fiore et al. 1989 for two possible expectations). This power-law behaviour generally occurs in the range from hours to days for AGN and 0.1Hz - 10Hz for galactic sources, a range which scales roughly with the central mass. Since these objects are all believed to be

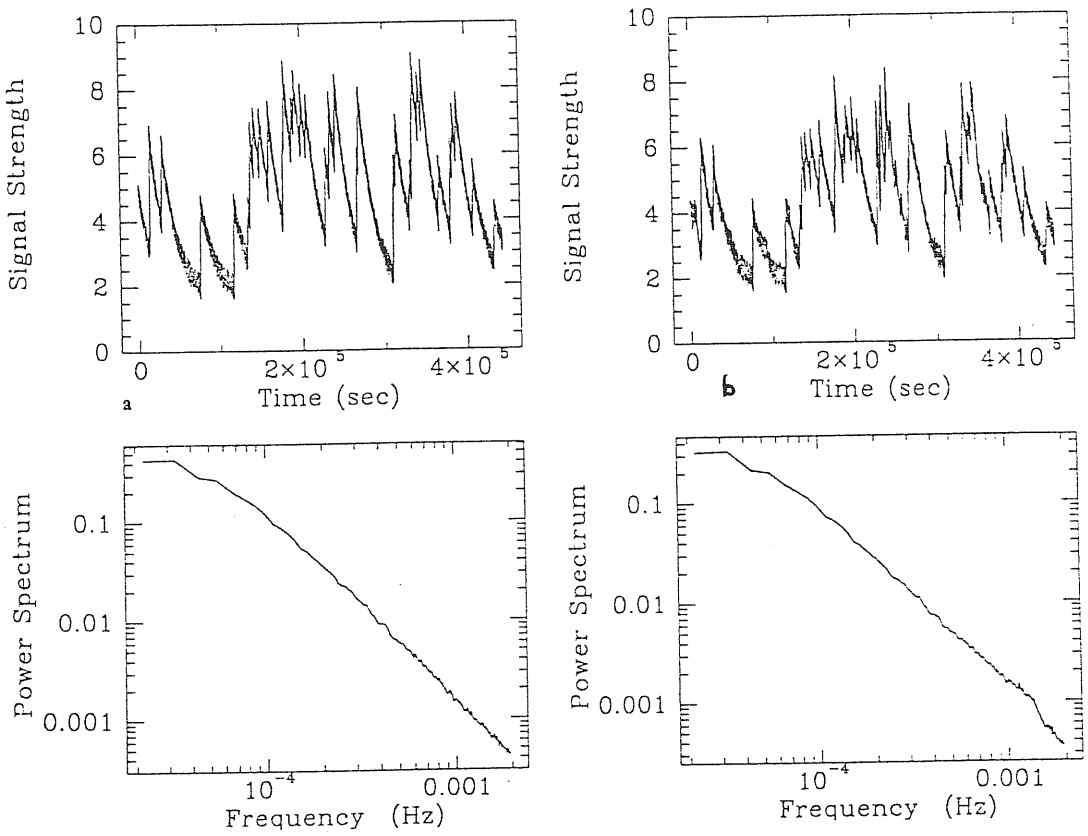


**Fig. 3.7a** and **3.7b.** The apparent variability can be different from the intrinsic variability due to the orbital motion of the spots, if they can survive for a few orbital periods. In these diagrams, the intrinsic variability is described by an exponential decay, $e^{-t/t_o}$ and $\omega(r_{in})t_o = 8\pi$. **a** (left): The simulated light curve (top) and the corresponding power spectrum (bottom) when the disk is seen face-on; **b** (right): The inclination angle here is $60^o$. Note that the spot appears near the innermost orbit at time $t \sim 210^5 s$ in the portion of the light curve shown here. Note also the departure of the power spectrum from $\omega^{-2}$ for high orbital frequencies.

powered by the accretion and the disk motion must be relativistic for these systems, the similarity in the variability might be attributed to the presence of "hot spots" on the surface of the disk.

As is clearly demonstrated in Fig. 3.6, if rotation is one of the important factors, any radial variation in spot properties will introduce certain observable structures into the variability power spectrum. The most noteworthy ones are the flattening of power spectra at the low frequency end, corresponding to the decrease of the spot number and spot intensity at larger radii, as first suggested by Shakura and Sunyaev (1976) and Nolan et al (1981); and the cut-off in power spectra at the high frequency end, corresponding to the absence of spots beyond the inner edge of the disk. The low frequency flattening could also be a result of the exponential decay in time of spot intensity, but the high frequency cut-off seems more naturally associated with the absence of spots. There is a possible break case of low frequency flattening of the power spectrum of AGN, i.e., NGC 5506, (see Fig. 2 in McHardy 1989) and a few break cases for galactic sources(e.g., Fig. 2 in Nolan et al. 1981 ad Fig. 3 in Makishima 1988 for Cyg X-1). The situation at the high frequency end is generally less clear due to the high noise level there, with possibly the exception of Cyg X-1 for which an ensemble-averaged power spectrum in the X-ray energy band 1-24KeV is obtained (Fig. 3 in Makishima 1988). We can read off the cut-off frequency to be approximately 100 Hz from this figure. This would correspond to a central mass in the range $14M_{\odot} \leq M \leq 60M_{\odot}$ if we take $8M \geq r_{in} \geq 3M$, taking into account the sharp decrease of radiation from disks very close to the inner edge of the accretion disk. This estimate is not very different from the current observational estimate of $M = 16 \pm 5M_{\odot}$ (Gies and Bolton 1986), though we may still need to look at the higher energy band so that the reprocessing of signal

by the intervening medium can be considered unimportant. Nevertheless, if the noise inherent in the signal (e.g., that due to flicker noise, which will always be present, or due to variations in the intervening medium) is not very high, then by reducing the instrumental error we might be able to observe features close to the cut-off and relate them to the central mass.

The fact that the intrinsic variability timescales are generally longer than the local orbital period has enabled us to partially understand the X-ray variability power spectrum. However, our present lack of knowledge of the spot production and destruction processes has prevented us from making any fit of a particular model to the observational data, aside from pointing out the possible causes of some observed structures in the power spectrum. Some further study of non-stationary, non-axisymmetric accretion disks is clearly needed in order to understand the rich variability data now available from which useful information on the central engine can be extracted.

### 3.5.4 Conclusion

- The slope of the variability power spectrum due to many spots depends on the statistics of spots, the inclination angle of the spots orbit and the rotation law of the disk.
- Flattening (at low frequency end) and cut off (at high frequency end ) features are distinct in the variability power spectrum. The former is due to a decrease in the spots number and the intensity in the outer part of the disk, whereas the latter is due to the absence of spots from the inner edge of the disk.
- The uniform radial distribution of the statistical properties of the spots and

a Keplerian disk gives the power index

$$\beta = \frac{5}{3}$$

## 3.6 The power spectrum due to spots on a relativistic Keplerian disk

The Doppler effect and occultation have been well discussed in section 4 and section 5. It is assumed that photons travel in a straight line. The Doppler effect introduces variations in X-ray intensity. The statistics of spots, the rotation law of the accretion disk, together with the viewing angle of the observer control the shape of the power spectrum of the light curve. This approach gives a good approximation when the disk is very thick or when the observer is not close to the orbital plane of the emitting matter (spots). It makes the problem easier to solve, and such quantities as the impact parameter of the photon, the relation between the position of the emitting matter and the photon arrival time can thus be expressed analytically. However, the gravitational effect can be very important when the above conditions are not satisfied. In this case, we can not find any analytic relation between the impact parameter of the photon and the position of the spot, nor between the flux and photon arrival time and so on. Meanwhile, we can no longer treat the solid angle as a constant in general relativity (see last chapter). In order to find the relations we have to do integrals along each photon trajectory from the spot to the observer. For the power spectrum due to many spots at different radii, the above-mentioned factors will complicate the computation process. In the following, the numerical result is presented. In the

calculation, all relativistic effects (Doppler effect and gravitational lensing) are included.

### 3.6.1 Power spectrum due to one spot

We calculate the time series due to one spot by the method described in chapter 2., and then we use numerical code to calculate its corresponding power spectrum.

Fig. 3.8 shows the light curves and their power spectra for a spot located at $r = 6r_s$ and at different inclination angles.

The power spectra of the light curves due to one spot are multi-peaked, the peaks harmonically related. The fundamental corresponds to the orbital period of the spot, and the peak at fundamental contains more power than those at harmonics. As the inclination angle increases (see Fig. 3.8), the gravitational lensing effect intensifies, and the light curve appears non–sinusoidal. This phenomenon makes the variability power at harmonics comparable with that at fundamental because of the increasing lensing effect. The ratios between the peaks in the power spectrum due to one spot are a function of the viewing angle of the observer $i$ and the position of the spot $r_s$. Note that under the weak field approximation (see Fig. 3.4), even for large projection velocity $v_i$, the harmonics (non–eclipsing case) possesses far less power than the fundamental. Two interesting results can be derived from the power spectrum. First, the high frequency component( higher than orbital frequency) contains power comparable to the fundamental, that is, the full relativistic effect (the Doppler effect plus the gravitational lensing) will flatten the power spectrum of many spots. Second, since the lensing effect becomes greater when the spots are closer to the black hole, more power goes to the

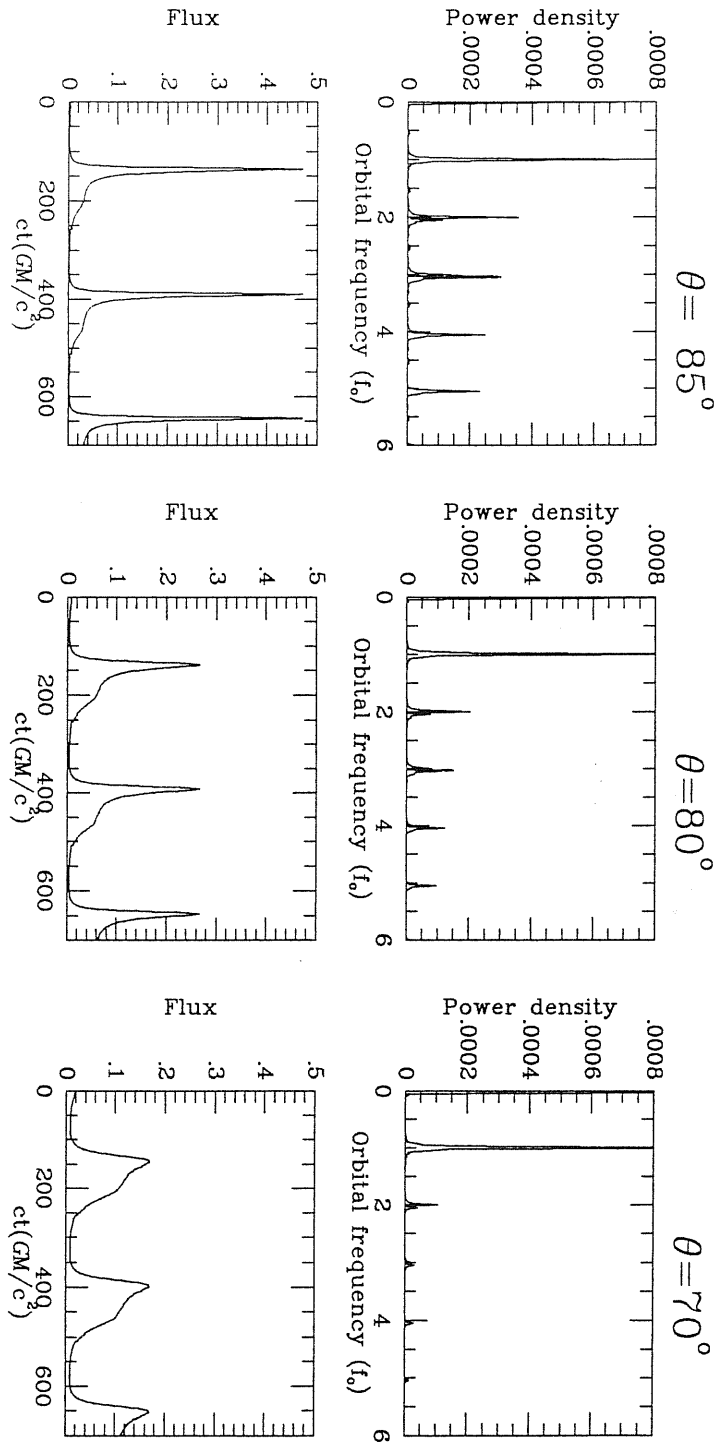


Fig. 3.8 The light curves and their power spectra for a spot at $r = 6r_s$ and with different orbit inclination angles $i = 70°, 80°$ and $85°$. The units for the flux and power density are arbitrary, and the unit for time is $\frac{GM}{c^2}$. $f_o$ is the orbital frequency of the spot.

harmonics, which will smooth the predicted "cut off " frequency that corresponds to the highest orbital frequency of the spots (section 5).

### 3.6.2 Power spectrum due to non-uniform statistics of spots

The realistic statistics of spots could be highly complicated, as depends on many currently-unknown parameters, e.g.,the time evolution envelope, the creation phase of spots, the size of the spots and the brightness of the spots, etc. We have discussed the case in which the spots creation is axisymmetric and all the spots have equal brightness (section 4). In this situation, the shape (the relative ratios of the peaks) of the power spectrum is strongly modulated by the disk self-eclipse. In the non-eclipsing situation, the peak at the fundamental contains almost all of the variability power. However, the practical statistics of the spots may be a strong function of the spots creation phase $\phi_i$ and the brightness of the spots. In this part, we will show how the creation phase and the brightness of the spots, apart from the radial location of spots and the inclination angle of the spots orbit, affect the shape of variability power spectrum.

Fig. 3.9 shows the light curve and its power spectrum due to four spots. The spots have different brightness, and are distributed non-axisymmetrically. Spot 1 with brightness 1.5 is at $\phi_s = 0$ at moment $t = 0$; spot 2 is at $\phi_s = 1.57$ with brightness 0.5; spot 3 is at $\phi_s = 3.64$ with brightness 1; and spot 4 is at $\phi_s = 4.71$ with brightness 0.5. All the spots are located at $6r_s$ ($r_s$ is Schwarzschild radius) and the observer has a viewing angle of $i = 76.5^o$. The light curve shows visible periodic flares, and the ratios of the flares are relative to the spots brightness. There are mainly five peaks (others with negligible power) in the power spectrum. The amount of power contained in the peaks is independent of the harmonical

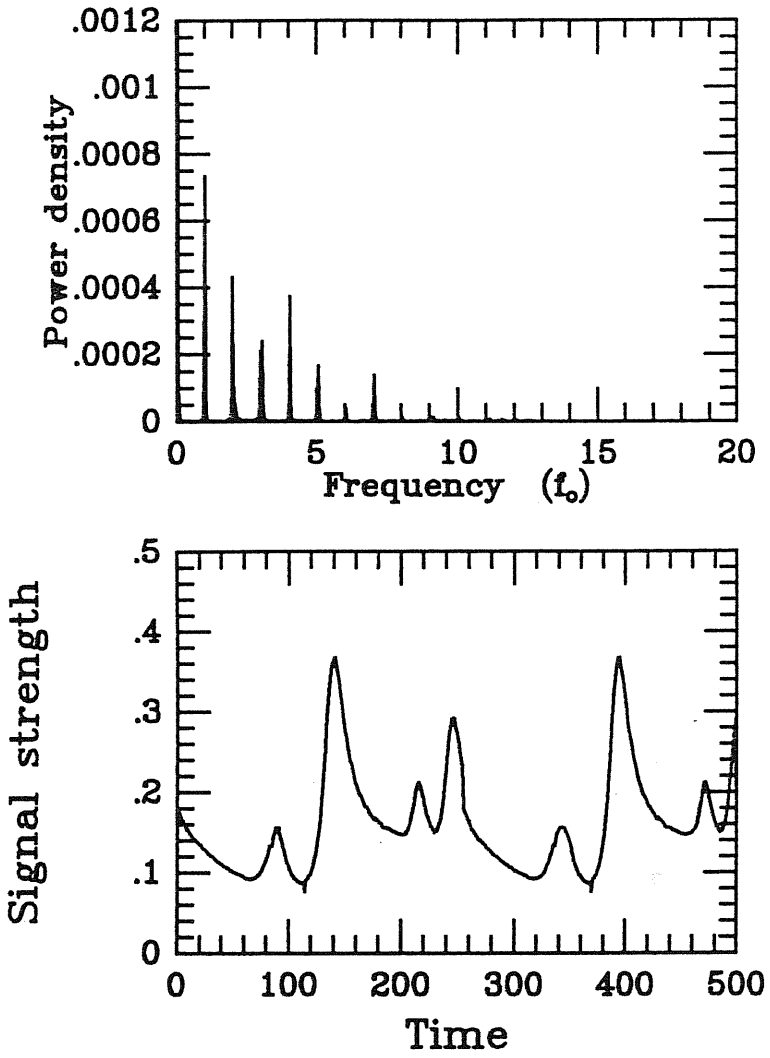


**Fig. 3.9** The light curve and its power spectrum due to four spots. The spots have different brightness and are distributed non-axisymmetrically. The first bright spot( with brightness 1.5) is at $\phi_s = 0$ at moment $t = 0$, spot 2 is at $\phi_s = 1.57$ with brightness 0.5, spot 3 is at $\phi_s = 3.64$ with brightness 1 and spot 4 is at $\phi_s = 4.71$ with brightness 0.5. All the spots are located at $6r_s$.

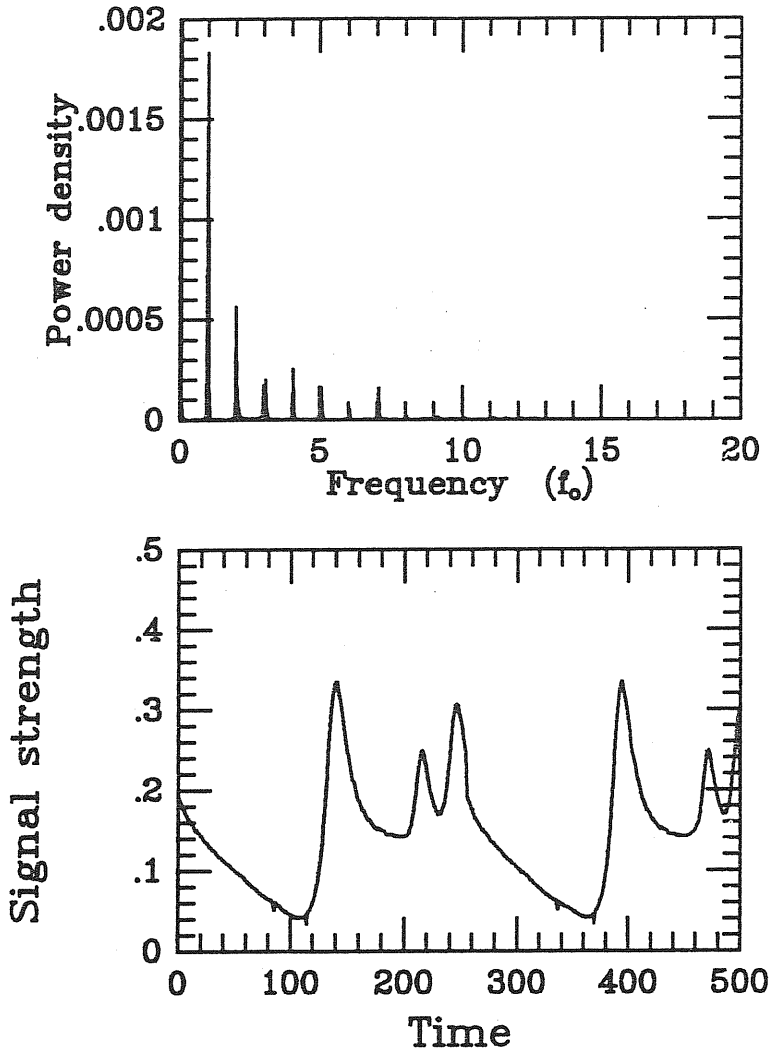


**Fig. 3.10** The light curve and its power spectrum for four spots. The spots have different brightness and are distributed non-axisymmetrically. The first bright spot( with brightness 1.5) is at $\phi_s = 0$ at moment $t = 0$, the spot 2 is at $\phi_s = 1.57$ with brightness 0.02, spot 3 is at $\phi_s = 3.64$ with brightness 1 and spot 4 is at $\phi_s = 4.71$ with brightness 0.7. The spots are located at $6r_s$.

order.

Fig. 3.10 shows the light curve and its power spectrum due to four spots. The spots have different brightness and are distributed non-axisymmetrically. The first bright spot( with brightness 1.5) is at $\phi_s = 0$ at moment $t = 0$; spot 2 is at $\phi_s = 1.57$ with brightness 0.02; spot 3 is at $\phi_s = 3.64$ with brightness 1; and spot 4 is at $\phi_s = 4.71$ with brightness 0.7. The spots are located at $6r_s$, and the observer has a viewing angle of $i = 76.5^o$. Since spot 2 is faint, its resulting flare in the light curve is too weak to see. The difference of the statistics of the spots between Fig. 3.9 and Fig.3.10 lies in the brightness. The two power spectra are structured quite differently. In Fig. 3.9 the peak at fundamental is the highest, the fourth peak second to it, while in Fig. 3.10 the third peak is the highest, and the one at fundamental is even lower than the one at the first harmonic. This demonstrates that the non-uniform brightness of the spots also influences the power spectrum.

Fig. 3.11 shows the light curve and its power spectrum due to the presence of four spots.

The spots have different brightness, and are distributed non-axisymmetrically. The first bright spot( with brightness 1.5) is at $\phi_s = 0$ at moment $t = 0$; spot 2 is at $\phi_s = 1.57$ with brightness 0.5; spot 3 is at $\phi_s = 3.64$ with brightness 1; and spot 4 is at $\phi_s = 4.71$ with brightness 0.5. The spots are located at $6r_s$, and the observer has a viewing angle of $i = 74^o$. All the physical conditions are the same as those in Fig. 3.10 except for the inclination angle. In this case we make only a slight change in the inclination $i$ from $76.5^o$ to $74^o$, which leads to different features in their power spectra. This implies that the gravitational lensing effect is essential to the structure of the spectrum (the lensing effect is sensitive to the inclination angle).

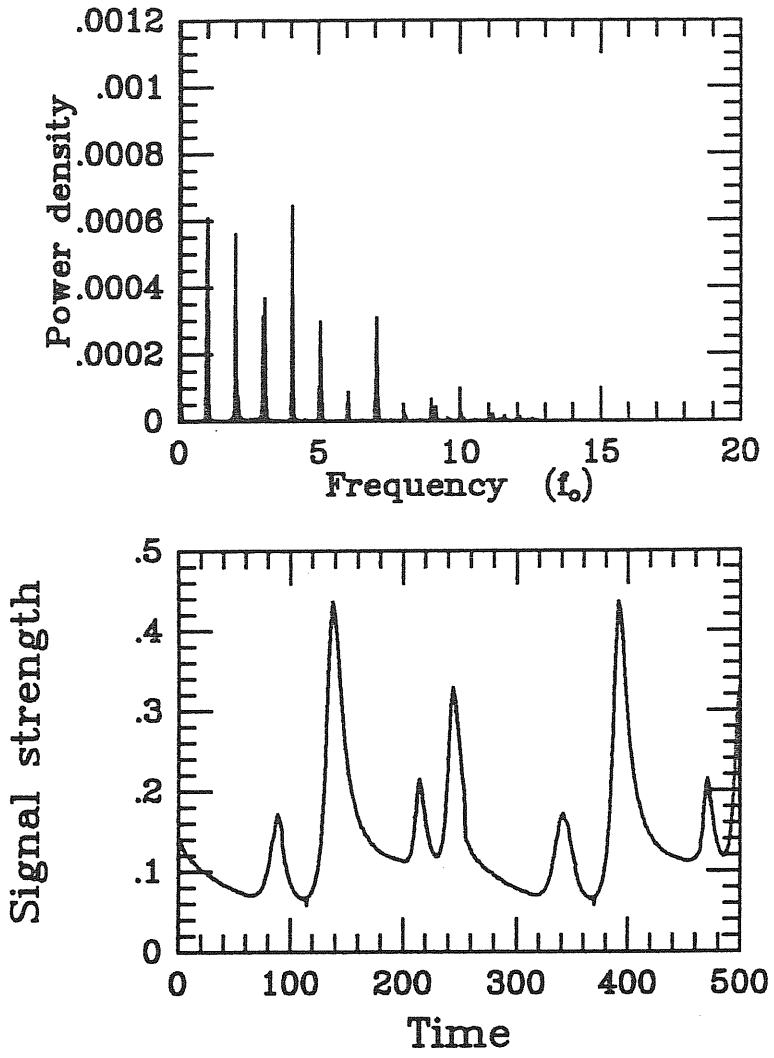


**Fig. 3.11** The light curve and its power spectrum due to four spots. The spots have different brightness and are distributed non-axisymmetrically. The first bright spot( with brightness 1.5) is at $\phi_s = 0$ at moment $t = 0$; spot 2 is at $\phi_s = 1.57$ with brightness 0.5; spot 3 is at $\phi_s = 3.64$ with brightness 1; and spot 4 is at $\phi_s = 4.71$ with brightness 0.5. The spots are located at $6r_s$.

### 3.6.3 Variability Power-law spectrum

To produce the power-law variability spectrum, we calculate the light curves and the power spectrum due to many spots scattering over a wide range of the disk. We first calculate the light curve of one spot at different radii using the methods described in chapter 2, and then derive the total light curve by summing the contributions from all the spots according to the given time. We assume that the spots have equal brightness and radiate X-rays isotropically in their own rest frames.

In the first place, we check if the number of the spots $N$ is an important parameter for a power–law variability power spectrum. The calculation shows that when the statistics of the spot, e.g. the distribution function $n(r)$, the emissivity $I(r)$ of the disk, is given, $N$ does not affect the slope of the power spectrum, that is, after $N$ exceeds a certain limit, the slope of the power spectrum remains the same regardless of the number adopted. The critical number for a power law variability spectrum is order of $N \sim 10$. The greater the number of the spots is, the smoother the power spectrum looks. Fig. 3.12 shows the power spectrum for 10 spots distributed from $r_{in} = 3.5r_s$ to $r_{out} = 35r_s$. The spots are uniformly distributed on the surface of the disk, the lifetime of the spots is chosen to be $\tau = 6 \times 10^3 \frac{GM}{c^3} s$ and the black hole has $10^8$ solar mass.

The result that the slope of variability power spectrum is independent of the number of spots $N$ ($N \geq 10$) is extremely important from the theoretical point of view. In principle, it is possible to fit the theoretical variability power spectrum to the observed one. And from the fitting we could obtain the statistics of the spots, the emissivity of the accretion disk and the inclination angle of the source. If we could identify the cut off frequency from the power spectrum, we would also

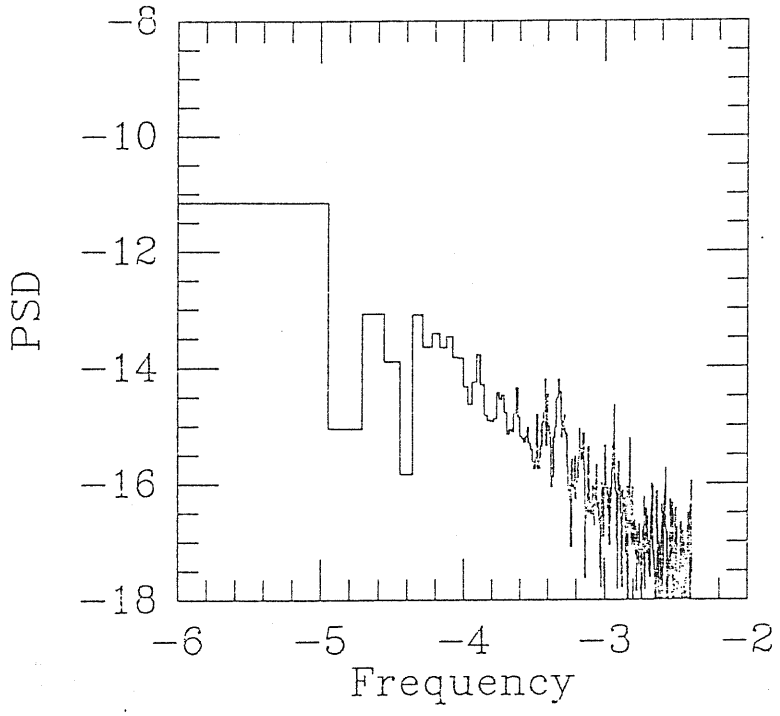


**Fig. 3.12** The power spectrum for 10 spots distributed from $r_{in} = 3.5r_s$ to $r_{out} = 35r_s$. The spots are uniformly distributed on the surface of the disk, the life time of spots is chosen to be $\tau = 6 \times 10^3 \frac{GM}{c^3} s$ and the black hole has $10^8$ solar masses.

be able to derive the central mass from the fitting.

To show how the spectrum shape depends on the inclination angle $i$, the power spectra for different inclination angles are given in Fig. 3.13

As has been proved in the weak field approximation (section 5), the power spectrum turns flatter with the increase of the inclination angle. Apart from the rotation induced variability power in the spectrum, the gravitational lensing ef-

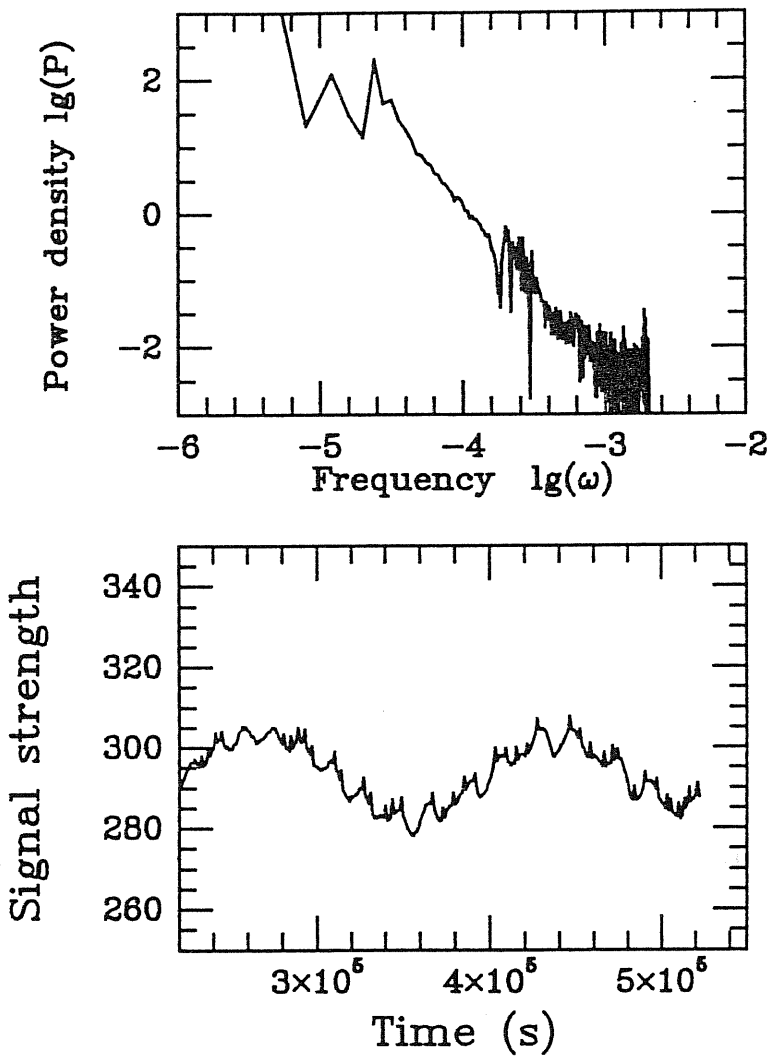


**Fig. 3.13a** The light curve due to 100 spots and its power spectrum for the inclination angle $i = 40^o$. The emissivity of the disk is assumed to be $I(r) \sim r^{-1/2}$.

fect also plays an important role in the variability power spectrum. As previously mentioned, we expect the power at high frequencies to increse when the lensing is involved. Fig. 3.13 shows the light curves and power spectra for different in-

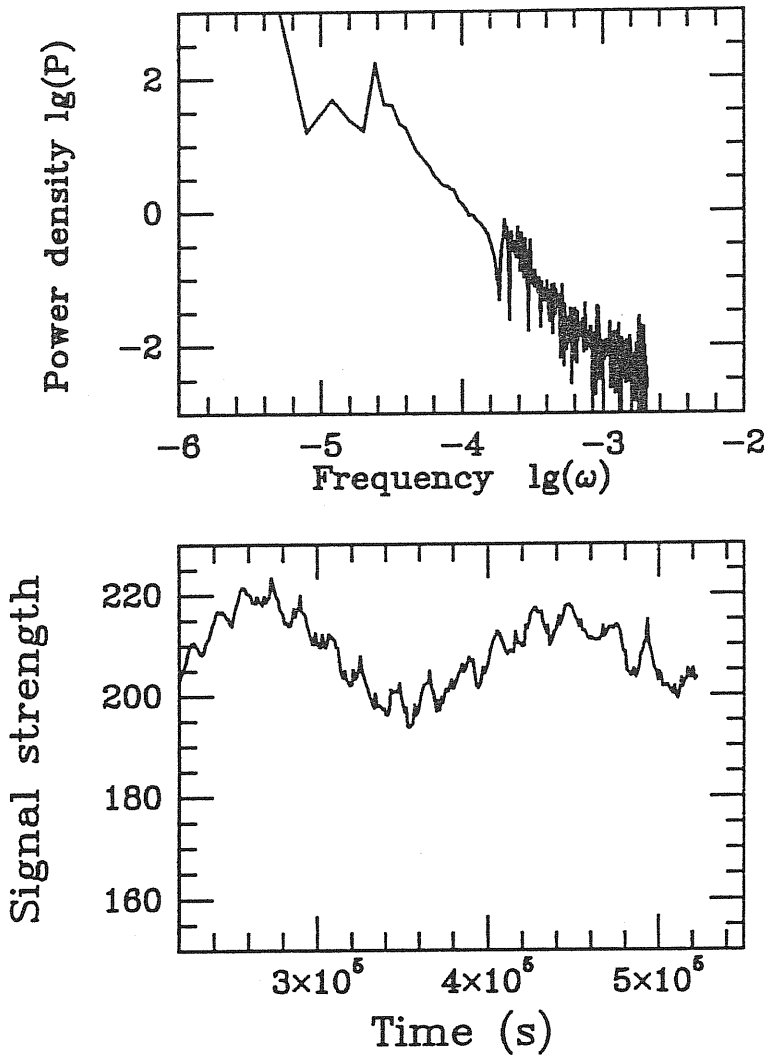


**Fig. 3.13b** The light curve due to 100 spots and power spectrum for the inclination angle $i = 60^o$. The emissivity of the disk is assumed to be $I(r) \sim r^{-1/2}$.

clination angles $i = 40^o, 60^o, 80^o$. The emissivity of the disk is assumed to be $I(r) \sim (0.1r)^{-1/2}$.

Not all kinds of disk emissivity of disk are capable of reproducing an exact

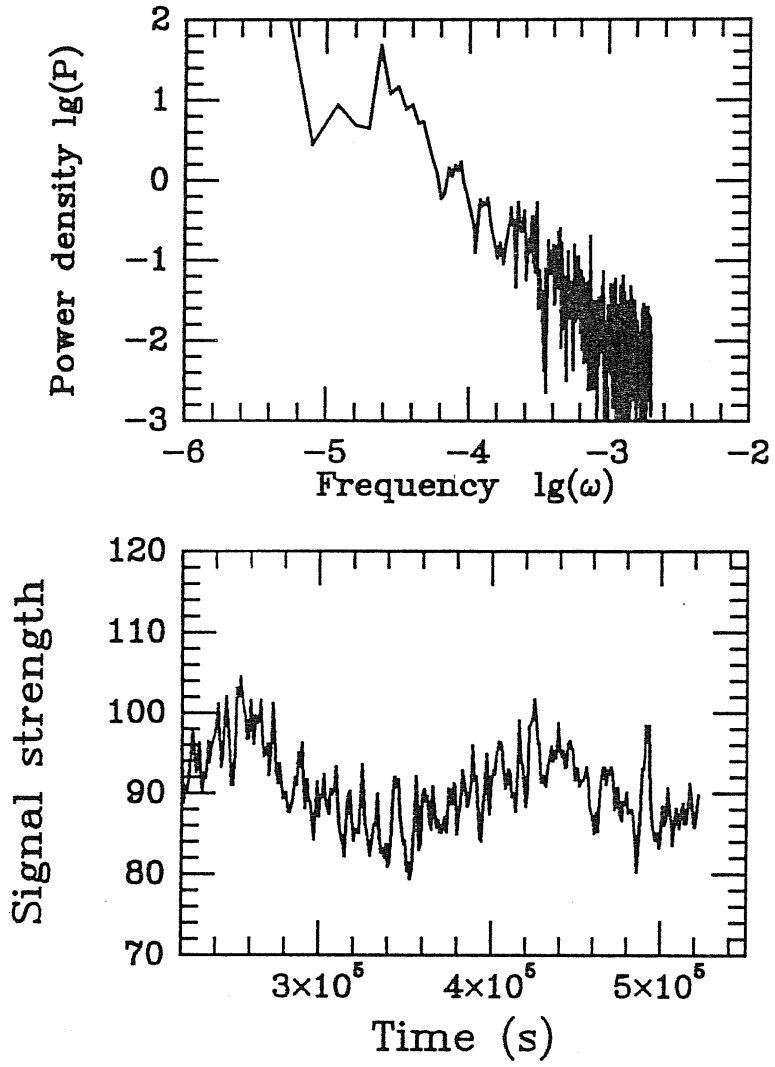


**Fig. 3.13c** The light curve due to 100 spots and its and power spectrum for inclination angle $i = 80^o$. The emissivity of the disk is assumed to be $I(r) \sim r^{-1/2}$.

power-law variability spectrum. Fig. 3.14 shows the light curve and the power spectrum for inclination angle $i = 80^o$. The emissivity of the disk is assumed to be $I(r) \sim r^{-1}$. The power spectrum is not exactly in a power-law form. This

knowledge can be useful to our future fitting, because the number of the parameters is thus reduced.

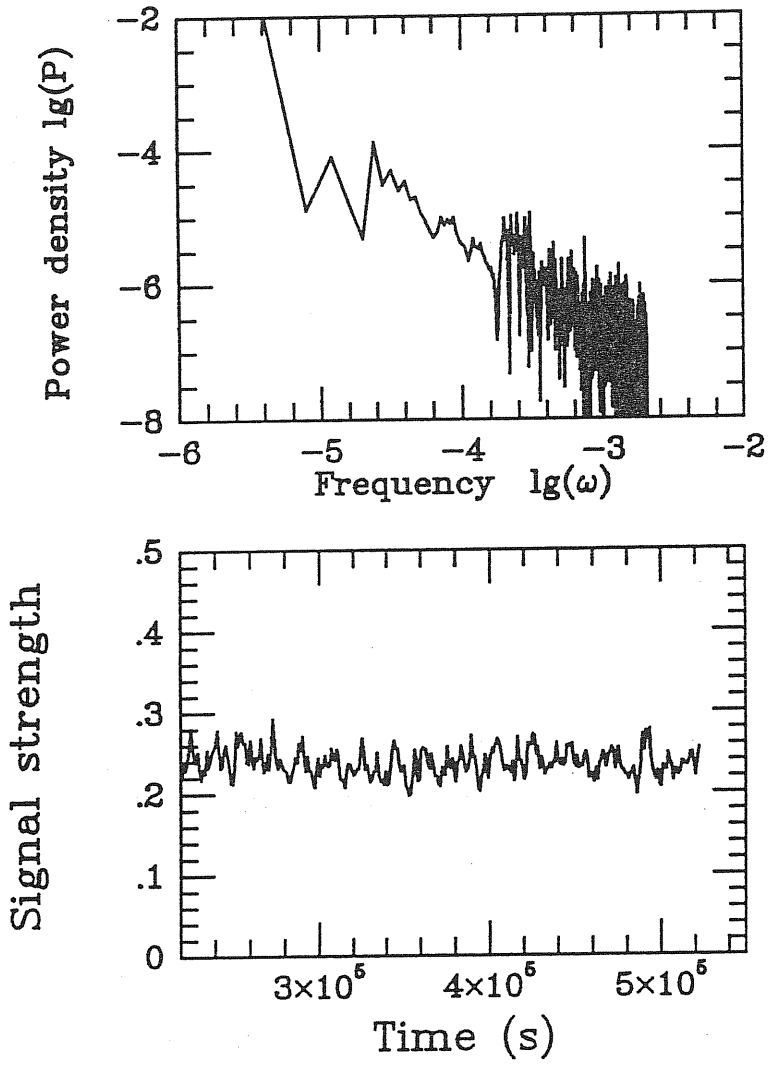


**Fig. 3.14** The light curves due to 100 spots and power spectrum for the inclination angle $i = 80^o$. The emissivity of the disk are assumed to be $I(r) \sim r^{-1}$. The power spectrum does not show an exact power-law form.

Another interesting finding is that we have not seen any distinct cut–off feature in the variability power spectrum as mentioned in the last section. The gravitational lensing is responsible for this. In the weak field approximation, for one spot, the variability power resides mostly in the fundamental, and the power in the other peaks is almost negligible (see section 4 of this chapter). So for many spots at different radii, the fundamentals due to all spots form a power law variability spectrum with a sharp cut-off feature at its high frequency end which corresponds to the fundamental frequency of the power spectrum of the spot located at the innermost region of the disk. When the gravitational lensing is involved, other harmonics contain power comparable with that at fundamental, and so the cut–off feature is weakened.

### 3.6.4 Discussion

The gravitational lensing and the Doppler effect introduce fast and sharp fluctuations in the X-ray light curve, which drives more power into high frequency components in the variability power spectrum. It weakens the "cut off" feature of the variability power spectrum when many spots appear on the surface of the accretion disk. Since AGN are believed to be black hole systems, our results may account for the difficulty in finding roll-off phenomenon in the X-ray variability power spectrum.

It is possible that for those sources with small inclination geometry in which power at the orbital frequency is dominant in the power spectrum, the cut-off frequency should be easier to identify. However, it is not always necessarily so because the rotation induced variability power is not always strong enough under the condition of small inclination geometry. It all depends on the completeness of

the observational data and the techniques for dealing with the data. In addition, the Doppler effect and the gravitational lensing are both important factors for the slope.

A multi-peaked variability power spectrum can be obtained when a spot is present on the surface of the accretion disks owing to the Doppler effect and the gravitational lensing. This may explain the variability power spectrum of NGC 6814 (for detail see the next Chapter).

### 3.6.5 Conclusion

- In the multi-peaked variability power spectrum, more power goes to higher harmonics when the lensing effect is involved;
- The non-uniform statistics of the spots, such as the brightness of spots, the creation phases, can affect the relative ratios of the peaks in the variability power spectrum.
- The lensing effect weakens the cut–off feature in the power-law variability power spectrum.
- The spots number $N$ exercises no control over the power spectrum slope when the statistics of the spot is given, which in principle makes the fitting of the observed power spectrum possible.
- The number of the parameters can be reduced, because not all kinds of statistics are capable of producing a power-law shaped variability spectrum.

Part of the work shown in this chapter is adapted
from Bao *Astron. Astrophys.*, 1992, Zhang and Bao *Astron. Astrophys.*, 1991,
Abramowicz, Bao, Lanza, and Zhang *Astron. Astrophys.*, 1992.

# Chapter 4

# The Models For NGC 6814

## 4.1 Introduction

### 4.1.1 Observation of NGC 6814

The X-ray flux of NGC 6814, a nearby ($z = 0.0053$) and a low luminosity Seyfert galaxy ($L_x \sim 10^{41-43} ergs^{-1}$), was found to vary with a timescale of $\sim 100$ sec early in 1978 by HEAO-A2 instrument (Tennant et al. 1981). The rapid variability was again observed by EXOSAT and Ginga many years later. In addition, many other peculiar properties of the source were seen.

From September, 1983 to October, 1985, the European X-ray Observatory EXOSAT observed NGC 6814 for five times at the intervals from a few months to a year, with the first four lasting approximately 5 hr and the last one about one day. The longest observation, the observation 1985/289, revealed quasi-periodic flares with a period $\sim 12200 \pm 100$ s in the ME $(2 - 6Kev)$ light curve, which for the first time shows strong evidence of the periodic behaviour of AGN (cf. NGC 4151, which displays periodicity in its X-ray light curve, but with small amplitude,

Fiore et al. 1989). The periodicity of NGC 6814 was first reported by Mittaz and Branduardi-Raymont in 1989(here after MB) and later confirmed by Fiore, Massaro and Barone in 1991, who also demonstrated the existence of some quasi-periodicity in four other shorter EXOSAT observations. The observed variability power spectrum of the longest observation is characterized by two components: the power- law component with the power index being $\beta \sim 1.0$ in the frequency range of $6 \times 10^{-5} - 10^{-2}$ Hz and the multi-peaked component with fundamental at $f_o = 8.2 \times 10^{-5}$ Hz corresponding to the duration of the periodic flares. Fig. 4.1a shows the ME light curve for observation 1985/289. The flux is basically chaotic, and the quasi-periodic flares are visible. The periodic flares are marked by arrows with intervals about 12000 s. Nothing unusual is seen in the ME background, so the flares could be securely attributed to the source.

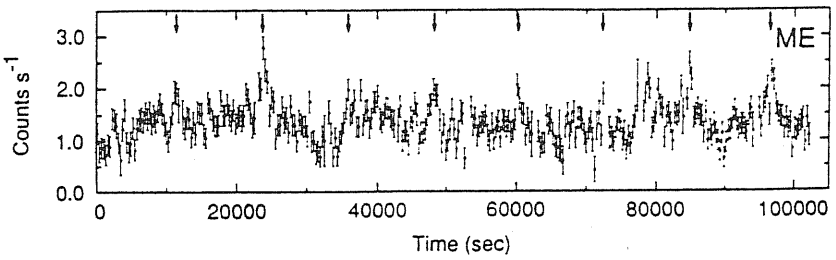


**Fig. 4.1a** The EXOSAT ME light curve of observation 1985/289 with bin time of 300 s. The arrows indicate the times of flares recurring at $\sim$ 12000$s$ interval (taken from MIttaz and Branduardi–Raymont 1989).

Fig. 4.1b shows the autocorrelation function for ME observation of 1985/289. There are two peaks at around 12000 s and 24000 s indicating the presence of the periodic flares in the time line.

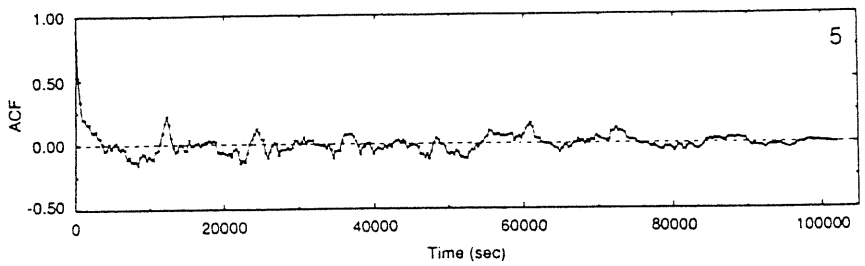


**Fig. 4.1b** The autocorrelation function of NGC 6814 for observation 1985/289 with bin time of 300 s. What is intersting is the peaks at 12000 s and 24000 s (taken from MIttaz and Branduardi–Raymont 1989). MB

Fig. 4.1c gives the variability power spectrum of the ME observation of 1985/289. The power spectrum shows five prominent peaks due to the presence of the periodic flares in the time series. It should be mentioned that a similar analysis of the background data of this observation has also been performed, but the produced power spectrum displayed no peaks which implies that the periodic behavior is intrinsic to the source, and it is neither caused by the periodicities inherent to the background nor by the array swapping of EXOSAT ME detector which occurs at every 10000–12000 s. The five peaks in the power spectrum correspond to the harmonics of the $\sim$ 12000s recurrence period of the flares, therefore

indicating that the flares are *non-sinusoidal.* The peaks are respectively located in the power spectrum at $f_o, 2f_o, 3f_o, 4f_o, 5f_o$.

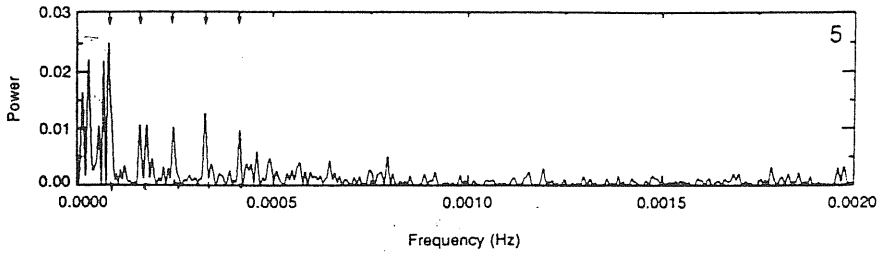


**Fig. 4.1c** The variability power spectrum of NGC 6814 for ME observation 1985/289. The peaks are marked by arrows corresponding to $\sim$ 12000$s$ fundamental and its harmonics. (taken from Mittaz and Branduardi–Raymont 1989). MB

Fig. 4.2 shows the power-law components of the variability power spectrum of 1989/289. The best fit of the power index is $\beta \sim 1.38 \pm 0.26$. This behavior is shared by most AGNs.

The same source was pointed at again by Ginga at three epochs from 1989 to 1990 ( April 28–30, 1989, April 15–17, 1990, and October 6–7, 1990) covering an energy range 1.5 to 37 KeV. The observation April 1990 and the observation April 1989 both revealed quasi–periodic dips and sharp drops with a period of $\sim$ 12000 sec in their light curves. The dips have width of about 200 – 300 sec. Fourier analysis shows that the shape of the variability power spectrum at high frequency

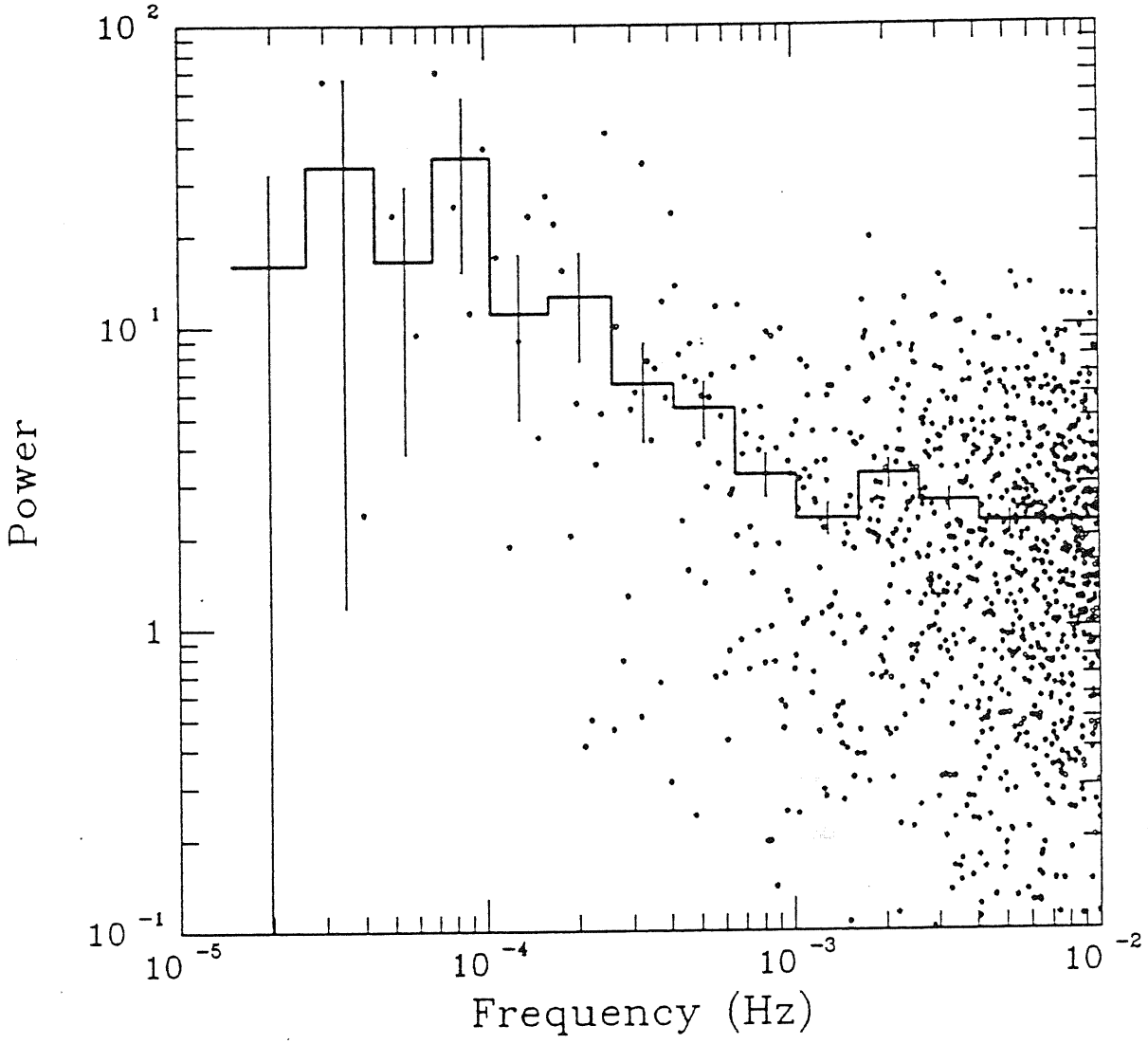


**Fig. 4.2** The power-law components of variability power spectrum of ME observation for 1985/128 plotted in a double logarithmic scale. The power index $\beta \sim -1$ (taken from Fiore, Masaro, and Barone 1992).

is roughly $p(f) \sim f^{-1}$, with no discernable steepening before Poisson noise level becomes dominant at 300 seconds (Done et al 1990) , and that there is a hump

in the power spectrum at $\sim 8 \times 10^{-5}$ Hz, which indicates the periodic behaviour at $\sim$ 12000 sec. The second observation showed phase coherence for 7 periods in the range of 12110–12145 seconds (Done et al. 1991). The morphology of the light curves seems to be remarkably different from that of EXOSAT. The folded light curve exhibits three main peaks instead of one as seen in the EXOSAT data. The five years separation of the EXOSAT and Ginga data argues that the periodic behaviour is well-defined and stable, and that the timescale may be attributed to some fundamental property of the system.

In the observation April 1989, the X-ray flux was changed by a factor of more than five over the entire observation, and the fact that the shortest time for the source to change by a factor of two was found to be about 50 s (Turner et al 1990) suggests that the hard X-ray emission region is very compact.

Moreover, Ginga found a fluorescent iron line with the centroid at $6.4KeV$ and with a line width of $0.4 \pm 0.4KeV$ in the X-ray spectrum of NGC 6814. The discovered iron line indicates the existence of "cold" matter around the central black hole. The equivalent width of the line is $\sim 350ev$, which is quite unusual to other Seyfert galaxies with a typical value of 150 eV (Pounds et al 1990). This suggests that NGC 6814 is very special. The iron line flux is also highly variable on the timescale of a few hundred seconds. The correlated change of the iron line flux with the continuum was observed. No lags between the intrinsic intensity variation of the line and that of the continuum larger than 200 sec were found (Done et al 1991). If the iron line is attributed to the "cold" iron, then this result is an indication that the primary X-ray source is extremely close to the "cold" matter. Fig. 4.3 shows the light curves of continuum X-ray (3.4 – 20.9 KeV) and of iron line of the Ginga observation of 1989 with the bin time of 256 s. The

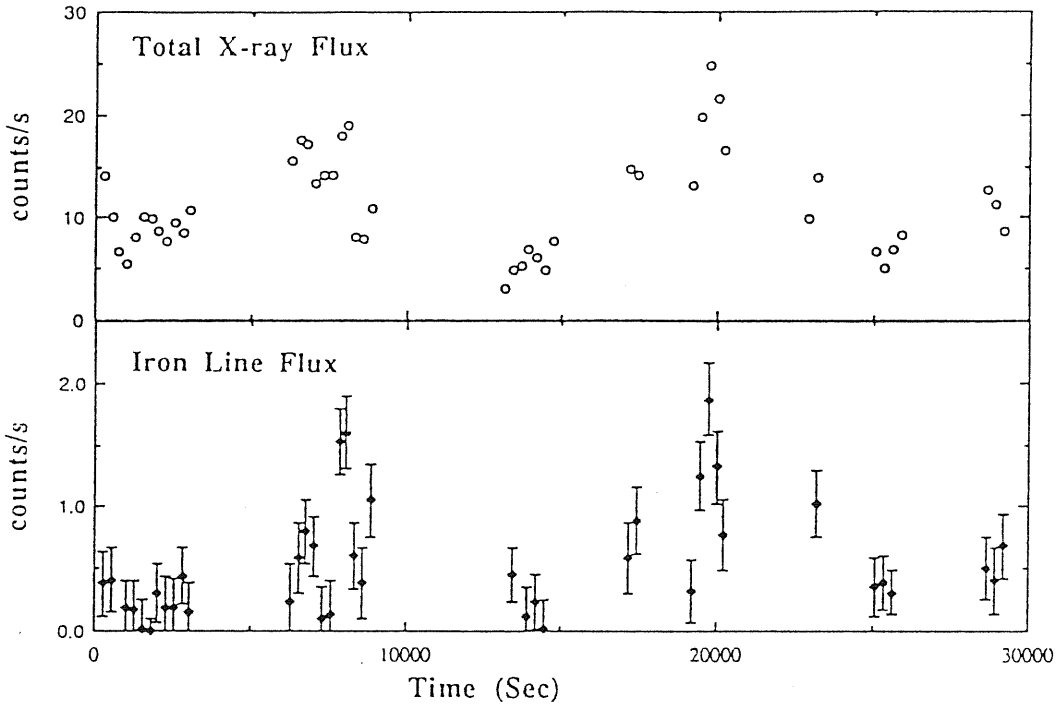


**Fig. 4.3** The light curve of the continuum X-rays and the light curve of the iron line (3.4 – 20.9 KeV) with bin time of 256 sec (taken from Kunieda et al 1990).

correlated variations are clearly seen.

The cross correlation function of the X-ray continuum and iron line is shown in Fig. 4.4. No delay larger than 256 sec is found.

### 4.1.2 Stability of the periodic behaviour of NGC 6814

The existence of the quasi-periodic flares in the X-ray flux of NGC 6814 is unlikely to be an artifact of some instrumental effects or data analysis. The data

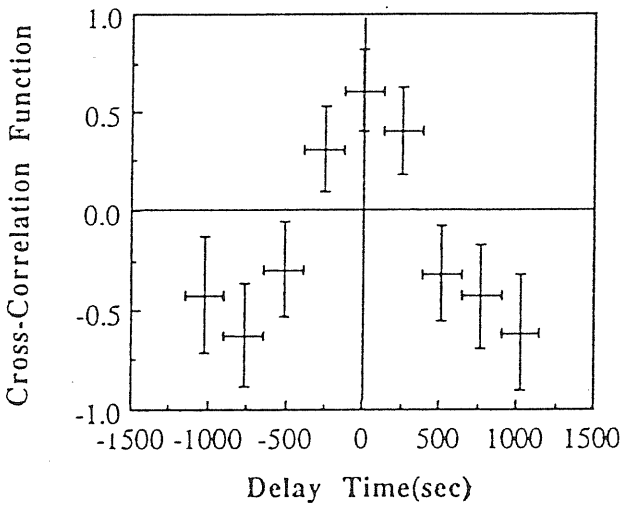


**Fig. 4.4** The cross correlation function of iron line flux vs continuum X-ray flux of observation 1989. Time binning is 256 sec (taken from Kunieda et al. 1990).

were collected by several different X-ray receivers on two satellites, and were then analyzed through different statistical methods. No change in the quasi-period was detected in the last $T = 5$ years, the time spanned between the EXOSAT and Ginga observations. The accuracy of the period estimate is better than about 10%, that is, the absolute error of a particular estimate is less than $\Delta t = 1000$ sec. Therefore, the relative quality of the stability of the quasi-period is better than $Q = T/\Delta t = 1.5 \times 10^5$. This is to show that a systematic period change, if present, is very small, $\dot{P}_0 < 1/Q < 10^{-5}$, and that the periodic flaring behaviour of NGC

6814 is a very stable and *intrinsic* phenomenon associated with some fundamental property of the system.

The average X-ray luminosity of NGC 6814 (which is approximately proportional to the accretion rate) has been slowly varying between $10^{42}$ erg/sec and $10^{43}$ erg/sec without upsetting the quasi-period $P_0$. The variability of NGC 6814 can therefore be attributed to a process very stable and independent of the accretion rate.

### 4.1.3 Where are the X-ray sources ?

The geometry of the innermost part of AGN, especially the relative location of primary X-ray sources to the "cold" accretion gas, has not yet been well-determined. The peculiar properties of NGC 6814 strongly suggest that a "clumpy" disk, with X-ray sources embedded, is most proper for characterizing the source (Day et al 1990; George and Fabian 1991). A "clumpy" disk is possible for the following reasons:

1. The innermost part of the disk may be unstable, and therefore the instability will produce clump-like matter in the disk.
2. The observed chaotic and quasi-periodic X-ray light curve and the variability features, i.e, the power-law component and the multi-peaked component, may be caused by the clumps corotating with the accretion disk.
3. The equivalent width of the iron line of this source is extremely large. An iron line equivalent width from reflection by an accretion disk of cool thick matter is expected to be about 180 ev or less for a solar abundance of iron (George and Fabian 1991; Matt, Perola and Piro 1991), which shows that the

**Figure 4.5** A possible geometry of NGC 6814.

equivalent width of the iron line of NGC 6814 is difficult to be explained by a simple reflection from an accretion disk subtending $2\pi$ at the X-ray source. The large equivalent width requires that the reflecting medium subtend a large solid angle at the primary X-ray source $\frac{\Omega}{4\pi} \geq \frac{1}{2}$( Turner et al. 1990) so that the cold accreting matter can absorb a large amount of hard X-ray. It is easy for the "cold" matter to subtend a large solid angle at the X-ray sources in this geometry.

4. The rapid X-ray variability with timescale $\sim$ 50s is seen in the X-ray continuum and the iron line flux; neither the time delay between the variation of iron

line and the continuum nor the delay between harder ($7-20$ KeV) and softer ($3-5.5$ KeV) X-rays larger than 200 s are found (Kunieda et al 1990, Done et al 1991). This suggests that the primary X-ray sources are very compact and are extremely close to the reflecting medium. The correlated variations of the hard and soft X-rays X-ray continuum and the iron line flux could be accounted for by the reprocessing of the hard X-ray radiation.

### 4.1.4 The orbital motion of the hot spot

The possible geometry described in the last section leads us to the awareness of the possibility to explain the periodic behaviour in terms of a process related to the orbital motion of the X-ray sources. The chaotic light curves suggest that apart from a bright clump which produces the main periodic flares during the time evolution, there exit many other small fainter clumps, which may explain the noise power spectrum. Stability of the period and independence from the accretion rate can be explained kinematically, and the fact that the variability is rarely observed can be attributed to the special geometry.

## 4.2 Fitting the models to the EXOSAT 1985/289 light curve

### 4.2.1 One bright spot model

It is very natural to associate the periodic flares with the theoretical light curve due to a spot moving around a black hole. A model of this kind was proposed

by Abramowicz, Bao, Fiore, Lanza, Massaro, Perola, Spiegel and Szuszkiewicz (1991).

The simplest version of the orbiting models consists of a single bright spot in a circular orbit centered on the black hole. The light curve depends on just two parameters, the radius of the orbit $r$ and the inclination angle $i$.

In the course of the fitting, we first calculate the light curves for different radii and different inclination angles, using the method described in Chapter 2. All the relativistic effects have been included with no approximations. Examples of the model light curves for different values of $r$ and $i$ are shown in Figure 2.7 in Chapter 2. It is worth noting that for small inclination angles (the orbit is seen nearly pole-on), the light curves are almost sinusoidal and have maxima at the orbital phase $\phi = (3/2)\pi$ and minima at $\varphi = (1/2)\pi$. This is because for the small inclination angles the orbital modulation of the observed intensity is dominated by the Doppler effect, which depends on the component orbital velocity along the line of sight which is maximal and positive (the source of light approaches the observer) at the phase $\phi = (3/2)\pi$ and maximal and negative at the phase $\varphi = (1/2)\pi$. For the large inclination angles (the orbit seen almost edge-on) the gravitational lensing of the light becomes dominant. This effect is more prominent when the inclination angle is larger than the critic value $i = 80^o$ (see Chapter 2). The lensing enhances the observed intensity when the bright spot is exactly behind the black hole (orbital phase $\varphi = \pi$) and moves orthogonally to the line of sight.

For each primary model light curve, hundreds of different secondary light curves were generated to statistically simulate the noise and the instrumental effects such as the low frequency noise present in the signal, the systematic error

connected to the background subtraction crossing array swaps due to the ME detector of EXOSAT. First, a Poisson noise distribution and the low frequency noise with the same statistical characteristics as for the observed low frequency noise were added to each model curve. Then, the secondary light curves have been sampled exactly at the same time as the observed one. The effect of the systematic error in the background subtraction was simulated by a random addition or subtraction of 1% of the background count rate to each segment between two swaps. The instrumental and noise effects have been simulated separately for each secondary light curve. Then the variability power spectra are calculated for each simulated time series, the distribution of the power at each frequency is derived and compared with that for the *EXOSAT* 1985/289 observation analyzed by Fiore, Massaro, and Barone(1992) ( see Table 1). Fig. 4.6 shows an example of this comparison for $i = 85^o, r = 10r_s$.The filled circle represent the power actually measured at $f_o ... 5f_o$ given in Table 1.

**Table 1:**

| Harmonic Number | $f_0$ | $f_1$ | $f_2$ | $f_3$ | $f_4$ |
|---|---|---|---|---|---|
| Frequency ($10^{-4}$Hz) | 0.825 | 1.625 | 2.475 | 3.300 | 4.125 |
| Normalized Power | 27.5 | 54.3 | 47.3 | 39.6 | 40.7 |

**Table 1** Harmonic peaks in the *EXOSAT* observation 1985/289.

Finally, the probability that the observed distribution of power in the harmonic frequencies $f_n$ is produced by the given model is calculated. It is found that the inclination angles lower than 80° must be rejected at a confidence level higher than 95 % and that the probability increases with $i$. The result is show in Table 2.

At this inclination, the probability appears to decrease slightly with the in-

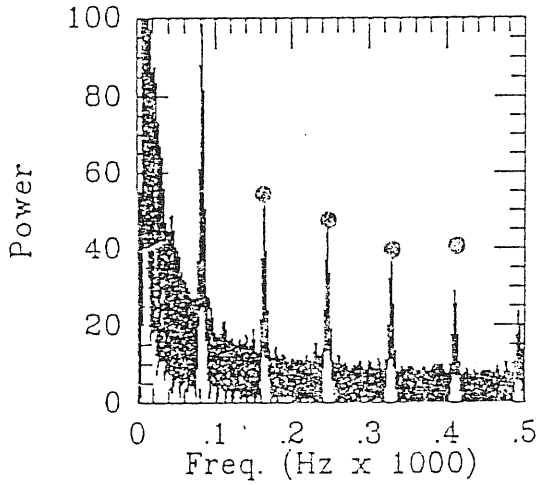


**Fig. 4.6** An example of PSD computed from one spot model.

**Table 2:**

| $r_S/r_G$ | 8 | 10 | 15 |
|---|---|---|---|
| $i$ | | | |
| 75° | $< 0.25$ | $< 0.25$ | $< 0.25$ |
| 80° | 0.25 | $< 0.25$ | 0.25 |
| 83° | 7.75 | 4.50 | 6.25 |
| 85° | 19.75 | 12.00 | 11.50 |

**Table 2** Probability (%) that the observed distribution of power is produced by a model with given $i$ and $r_S$.

creasing radius, but the dependence is so weak that it places no significant constraints on the orbital radius.

The best model parameter corresponds to $i = 85°$ and $r \sim 8r_G$. Since the error is not sensitive to the orbital radius, we can not decide $r$ precisely at which the spot locates. Figure 4.7 shows the light curve calculated for this case (with no noise or instrumental effects added), which is similar to Fig. 4.8.

The observed period $P_0 = 1.2 \times 10^4$ sec gives the mass of the central black hole $M = 6 \times 10^6 M_\odot$. The gravitational radius corresponding to the mass is $r_G = 9 \times 10^{11}$ cm, and the light crossing time $t_G = r_G/c = 30$ sec.

### 4.2.2 $1^{+3}$ spots model

Since "one spot" model can not determine the accurate location of the spot, which is, however, pivotal to understanding the source, a more complicated model is needed. Recently, the present writer has fitted $1^{+3}$ spots model. $1^{+3}$ means one bright spot and three faint spots. There are two reasons for adopting this model. Firstly, the power-law component in the variability power spectrum of NGC 6814 indicates the existence of many small faint spots on the disk, apart from the bright spot. As has been stated in Chapter 3, the power-law component of the variability power spectrum is attributed to the spots scattering widely on the disk, while the multi-peaked component is due to one or several spots appearing from a narrow radial region of the disk. The bright X-ray source (the bright spot) produces periodic flares during their corotating with the disk around a central black hole, and the faint spots, randomly distributed on the disk, produce the statistic fluctuations in the light curve, generating the power-law component in the

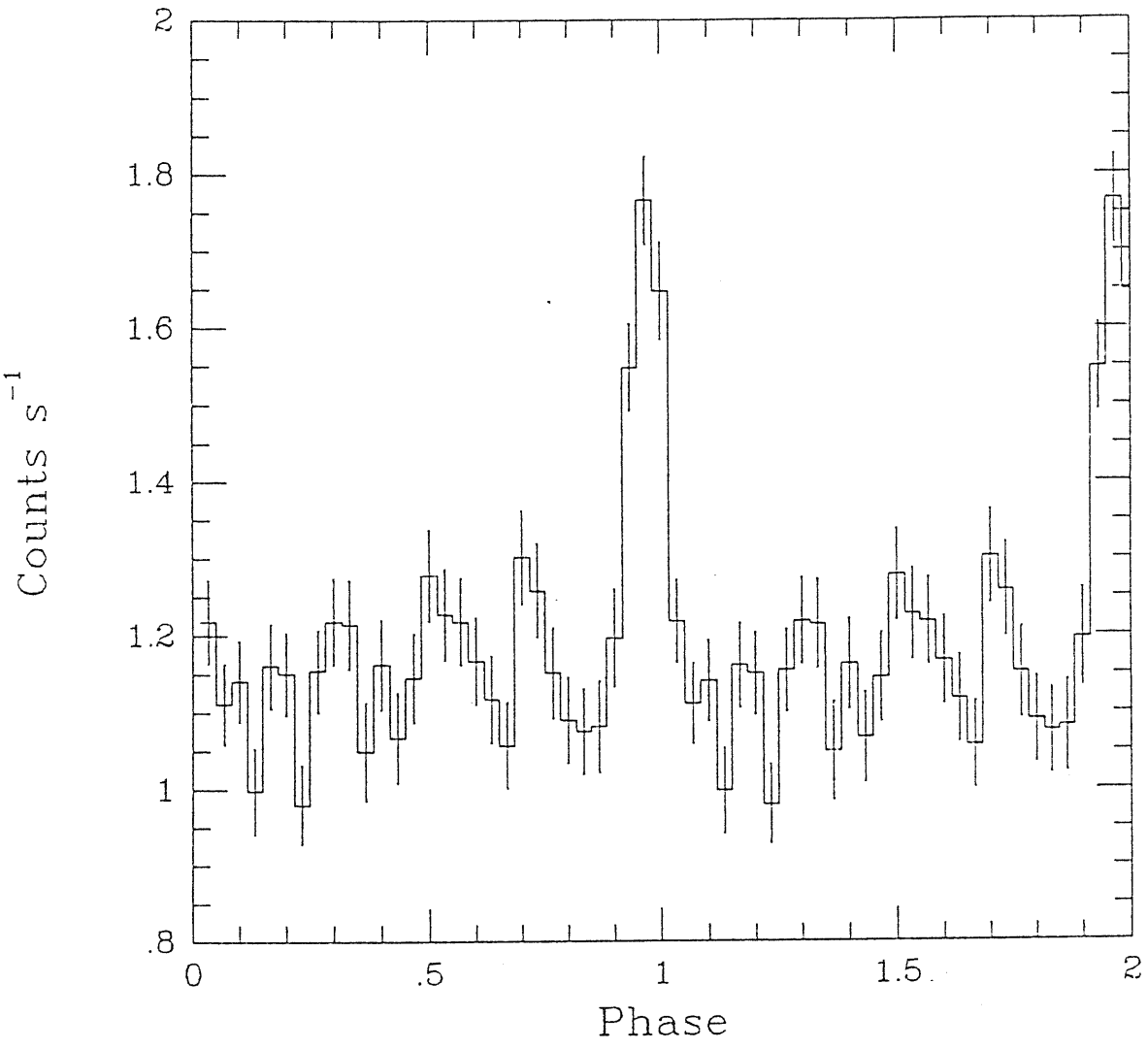


**Figure 4.8:** The folded light curve of EXOSAT observation of 1985/289 (from Abramowicz *et al.*, 1991a, 1991b).

variability power spectrum. It should be mentioned that the intrinsic brightness variation of those faint spots also contribute to the power-law component in the power spectrum. The power spectrum slope which is about $\beta \sim 1$ for NGC 6814

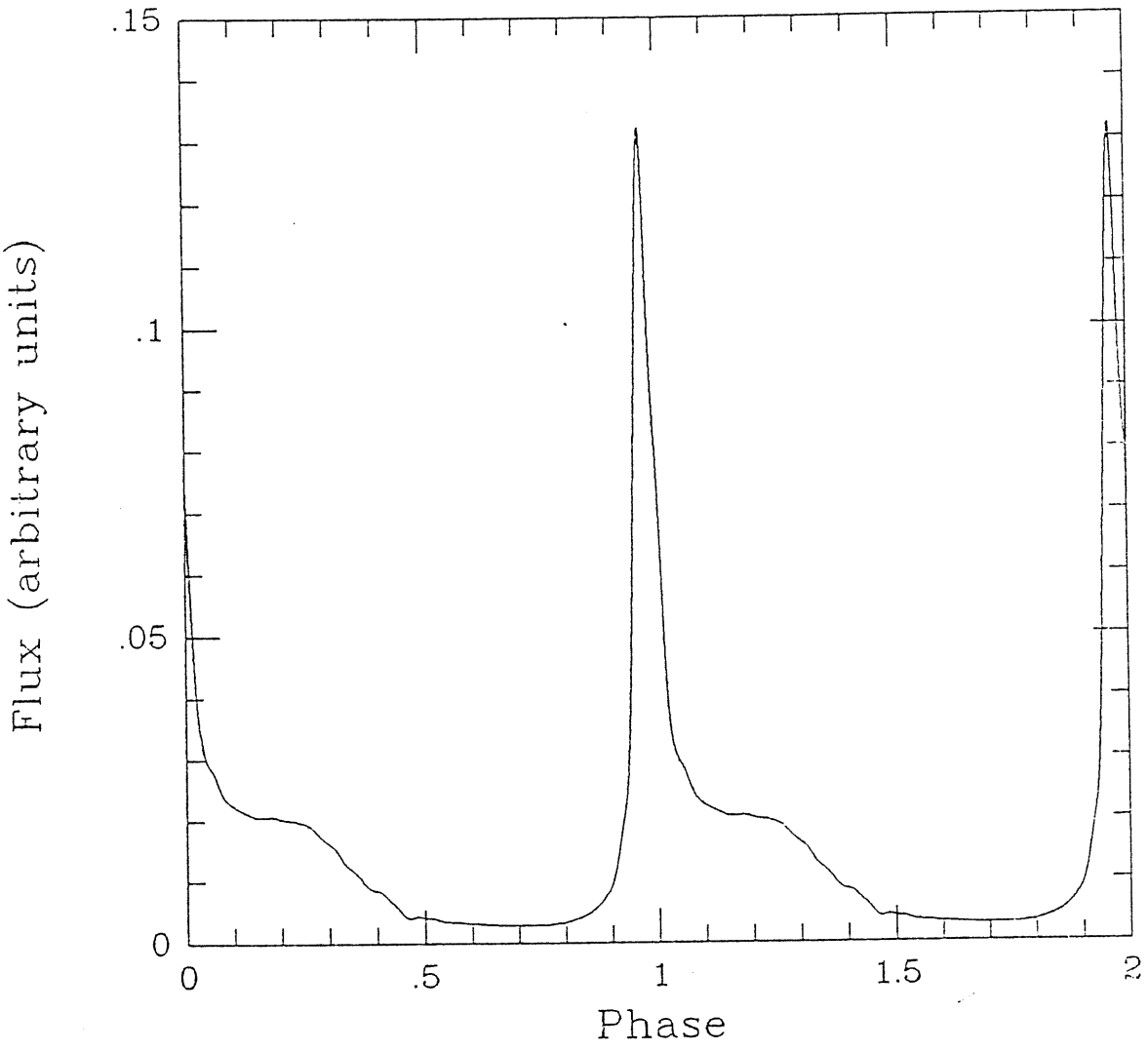


**Figure 4.7:** Light curve for the best orbital model (single bright spot on a circular orbit with $r = 8r_s$ and $i = 85°$ (from Abramowicz *et al.*, 1991a, 1991b)

can be an information source for the emissivity of the disk, the lifetime of the faint spots, the inclination angle of their orbits, etc. A more detailed description of this should be consistent with much of other observational evidence, with respect to the width of the iron line due to the inclination of the inner part of the disk, the

width of periodic flares and so on and so forth. Secondly, the variability power spectrum due to one spot differs a great deal from that of the observed one (see Chapter 2), which underlies the failure of the "one spot" model to determine the precise location of the bright spot in "one spot" model. Several small less bright spots might be in the same orbit as the bright spot. This should be reflected in the X-ray intensity of the source, and therefore in the multi-peaked variability power spectrum. The contribution from the small spots will influence the power spectrum. The observed multi-peaked variability power spectrum of NGC 6814 is probably a result of the "interference" of the two components (see Fig. 4.1).

The folded light curve of observation 1985/289 (Fig. 4.8) is unlikely caused by one spot on the orbit. Several faint flares may appear between the two big flares, and are not equally spaced.

**Table 3:**

| Harmonic Number | $f_0$ | $f_1$ | $f_2$ | $f_3$ | $f_4$ |
|---|---|---|---|---|---|
| Relative Hight | 2.5 | 1.0 | 1.0 | 1.3 | 0.95 |

**Table 3** Harmonic peaks in the *EXOSAT* observation 1985/289 derived by MB.

In this part, the result of MB data fitting is described, and the relative height of each peak in the variability power spectrum is given in Table 3.

The fitting is done in accordance with two principles: the power spectrum should be closer to the observed one; the flares in the light curve should have a duty cycle of about 0.1, which is revealed in the folded light curve. It should be mentioned that, in principle, the relative height of the flare places strong constraints on the model, but it is impossible to derive this from the theoretic light curve, as depends on certain currently unknown parameters, e.g. the intrinsic

brightness of the spot.

The fitting starts with deciding on the number of the small spots in the orbit where the bright spot is located. This parameter can be reached by looking at the number of the peaks in the observed variability power spectrum. It is proved that 3 is an ideal number, capable of producing five main peaks in the power spectrum. Then we have to determine the possible range of the inclination and the range of the radial orbit. All those orbits with an inclination angle smaller than the critical value $80^o$ can be rejected (see also Chapter 2). Thus the inclination range is limited to $80^o$ to $90^o$, which can be further reduced by the requirement of the observed duty cycle of the flare in the order of 0.1. The range of the radius can be simply set by the duty cycle. What is essential but difficult is to find out the spots distribution in the orbit and the ratios of their brightness.

The three faint spots happen to be in the same orbit as the bright spot during the EXOSAT observation of 1985/289. The four spots are labeled as 1 (the brightest) 2,3,4, as in Fig. 4.9. Hundreds of trials which scan the possible parameter space have picked out one case closest to the observational data, as illustrated in Fig.4.10. Fig. 4.10 shows the theoretical power spectrum for four spots in the orbit of $r = 6r_s$, with the inclination angle of $i = 85^o$. Spot 1 has relative brightness 1.5, and the rest 0.35. At the moment of $t = 0$, the four spots are at $\phi_s = 0.51, 1.34, 3.18, 5.26$ respectively. In the power spectrum "+" represents the observed relative height of the corresponding peak.

The power spectrum fits the observational data well. The largest error occurs at the second harmonics which is $\leq 10\%$. The fitting of Fig. 4.10 is so strict that even a minute change in parameter will lead to a big error. Fig. 4.11 shows an example in which all other parameters are the same as in Fig. 4.10, except for the

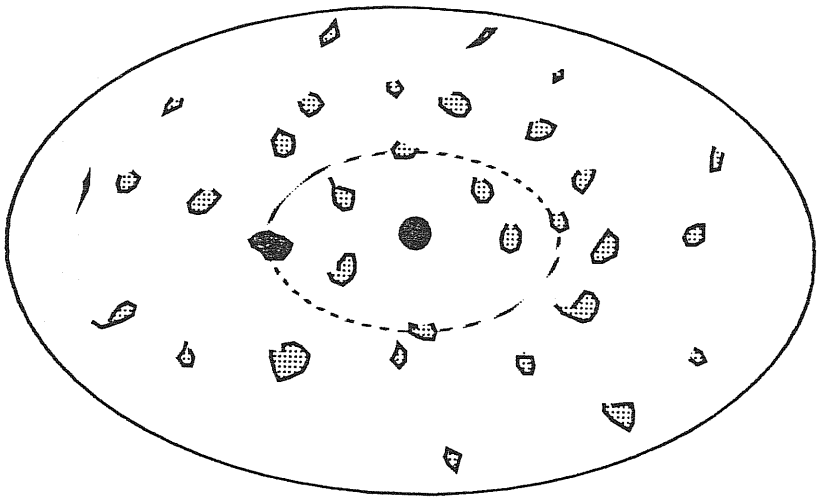

**Figure 4.9:** The geometry of NGC6814. Three faint spots happen to be in the same orbit as the bright spot during the observation 1985/289.

inclination angle which is $83^o$.

It follows from the above discussion that the best parameters for the model are $i = 85^o$ $r = 6r_s$. If we assume a Keplarian disk, with the observed period

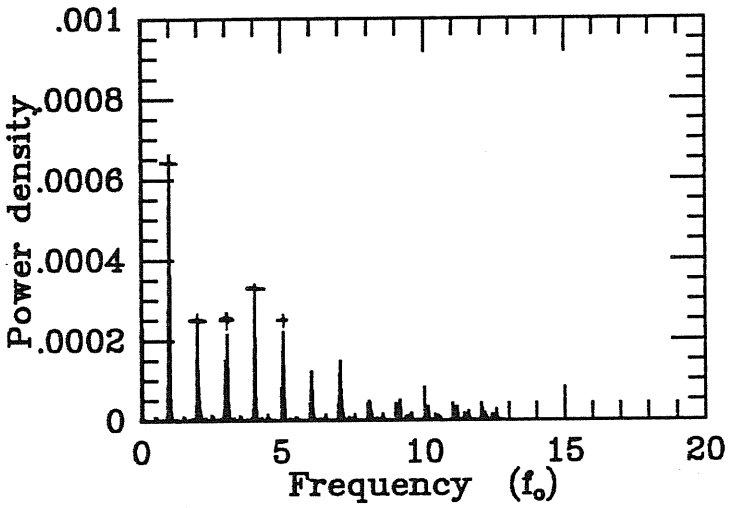


**Figure 4.10:** The power spectrum for four spots with the inclination angle $i = 85^o$..

$p_o = 12000$ sec, then we will get the central black hole with

$$M = 9.3 \times 10^6 M_\odot.$$

Its corresponding gravitational radius is $1.4 \times 10^{12} cm$ and its light crossing time 47 sec.

### 4.2.3 Discussions

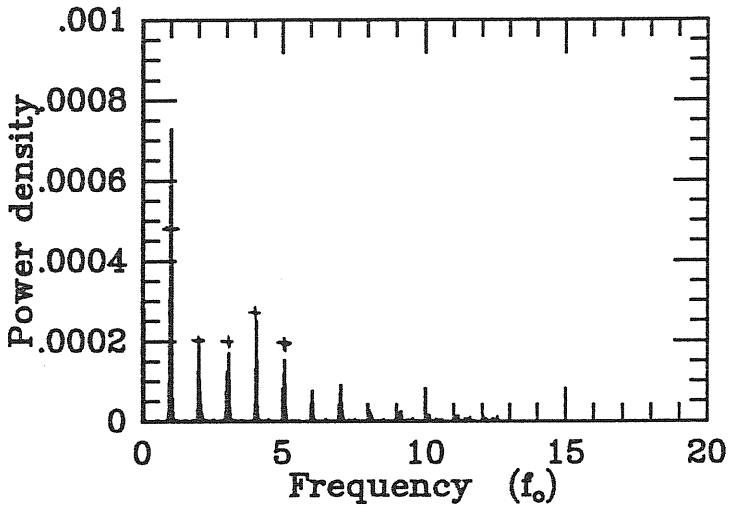


**Figure 4.11:** The power spectrum for four spots with inclination angle $i = 83^o$..

So far, we have presented by means of two different models: the"one bright" orbiting spot model, and the "1+$^3$" spots model. The "one-spot" model fitting is based on the observational data analyzed by Fiore, Massaro and Barone, while the "1+$^3$" spots model fitting employs the observational data analyzed by MB. Surprisingly, the results of the two fittings are consistent. This implies that the observed signal of EXOSAT observation has some basic property, despite the difference displayed in the data analyzed by the two different groups. The first fitting yields an accurate value for the inclination angle, and the second fitting gives both

the inclination and the orbit of the bright spot. The best results from the fitting are: the orbit of the bright spot has an inclination angle of

$$i \sim 85^o,$$

and its radius is

$$r \sim 6r_s,$$

which gives the mass of the central black hole

$$M \sim 9 \times 10^6 M_\odot.$$

Here it is worth mentioning that the three faint spots in $1^{+3}$ model may be three small vortexes created by the motion of the bright spot. Part of our future work will involve the fitting of the more complicated model to the data analyzed by Fiore,et al.

**a) The inclination angle**

The large inclination angle suggested by the model does not contradict the fact that the NGC 6814 host galaxy is seen nearly pole-on because of the smaller $H_I$ line width (Heckman, Balick, and Sullivan, 1978). There is no reason for assuming an alignment between the planes of the host galaxy and the central accretion disk (Abramowicz, 1992). In fact, the most recent observational evidence (based on the measured directions of the ionizing cones) points against such an alignment (Wilson, 1991). According to the unified scheme for Seyfert galaxies, Seyfert type 1 has its central accretion disks seen nearly pole-on, while Seyfert type 2 has the central disks nearly edge-on. The validity of the unified scheme has recently been seriously questioned (Wilson, 1991). However, it would be intearesting in this context to quote Sekiguchi and Menzies (1990) who found that the Seyfert type of

NGC 6814 was varying between 1.0 and 1.9, being close to 1.8 in 1985 when the *EXOSAT* 1985/289 observation was made.

It is important to note that for NGC 6814 the power spectrum of the featureless noise has a power index $\beta \sim 1.0$ (Fiore, Massaro and Barone 1991a, 1991b), which is in agreement with the orbiting model assuming a large inclination angle (see Chapter 3).

**b) The iron line**

The models interprete the variability of the intensity of the iron line as a direct consequence of the orbital motion of the spots, that is, the line is formed near the spots which are the carriers of the X-ray sources.

One problem for the model could be the upper limit of $0.4 \pm 0.4$ keV to the observed line width ($FWHM$) obtained by Kunieda *et al.* (1990). The line profile integrated over the whole period is $FWHM > 1$ keV. This seems to be in conflict with the observations. However, it is important to note that the real line profile is complex and very far from Gaussian, and that the observational limit on the line width was derived under the assumptions of a Gaussian profile. A discrepancy of this kind is ameliorated if the occultations are long enough, as the line width depends also on the duration of the eclipse.

**c) About the disk self-eclipse**

The sharp fall in the intensity observed by *Ginga* and the flare with rapid growth and decay observed by EXOSAT suggest that the bright spot may be periodically occulted by the more distant parts of the disk, and that eclipses may be very important to an accurate fitting of the variability data.

Note that although possible occultations introduce new free parameters to the model, the inclination angle is still directly restricted by observations. This

is because both the gravitational lensing and the occultations are symmetric with respect to the orbital phase $\varphi = \pi$. The gravitational lensing dominates at high inclination angles, while the Doppler effects prevail at low inclination angles. The light curves strongly influenced by the occultations at high inclination angles must therefore be symmetric, and those influenced by the occultations at low inclination angles must be asymmetric close to their maxima (see Figure 4.12). The lensing induced light curve always has its maximum at the center (a little bit away to the right due to the time delay effect), but the Doppler induced light curve always has the maximum at the right and the minimum at left. Comparing this with the *EXOSAT* folded light curve (Figure 4.8), qualitatively, we may conclude that models with the assumed occultations at large inclination angles are preferred, since the observed the flares are symmetric.

**d) What moves on the orbit ?**

The simple picture we draw leaves open the question of the true nature of the postulated orbiting objects and the source of their energy. There seems to be many candidates, but any candidate must satisfy the following two conditions:

(1) the orbiting object can produce hard X-rays or is at least a carrier of the hard X-ray source;

(2) the periodicity must be stable, with the lowest limit $T = 5$ years.

Here, we briefly describe one possibility suggested by Abramowicz, Lanza, Spiegel and Szuszkiewicz (1992). The periodic X-ray flares of NGC 6814 may be attributed to the orbital motion of very strong and long-lived vortexes. Such objects are not material; they are a form of excitation. The general radiation mechanism of a vortex is that the diminished pressure in the vortex core draws in radiation from the deep disk and allows it to escape in a collimated beam

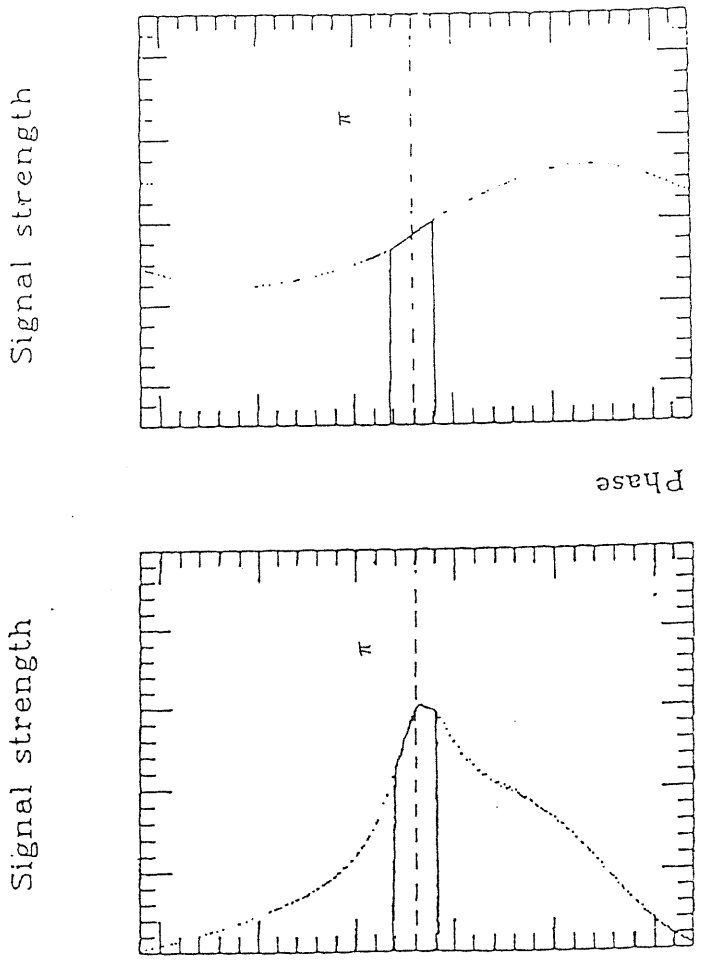


**Figure 4.12:** Light curves strongly influenced by long occultations: (a) at high inclination angles; (b) at low inclination angles

whose flux may exceed the Eddington limit locally. The longevity required by observations may be due either because of a solid body support or because of a subtle fluid dynamical process to produce it intrinsically. In the first case, it is

assumed that a small black hole moves along the circular orbit inside the accretion disk and stabilizes the position of the vortex. In the second case, the vortex is assumed to be similar to Jupiter's Great Red Spot or the analogous magnetic spot complexes seen in rapidly rotating RS CVn stars. The longevity of such vortexes is well established observationally, but the mechanism for forming such structures is not yet completely understood.

It is worth mentioning that even if the bright object is a White Dwarf or a neutron star, Six Schwarzschild radius is large enough to prevents the star from being disrupted by the tidal force. The Roche limit of the black hole with $10^7 M_\odot$ is $\sim 3 \times 10^8$ cm (Hills, 1975) for a neutron star (with mean density of $\sim 10^{15}$ g cm$^{-3}$), and is $7 \times 10^{10} cm$ for a White Dwarf (with mean density of $\sim 10^8$ g cm$^{-3}$), both being much less than Six Schwarzschild radius.

## 4.3 A comparison of different models of NGC 6814

### 4.3.1 Four possible models

Up to now, four different models have been proposed to explain the observed quasi-periodic variability in NGC 6814. They can be further classified in terms of the intrinsic process of the system and the apparent effects due to the rotation and geometry of the system.

Except for the orbiting spot model, no other models have ever undergone similar fitting. They have been suggested only as possibilities. They are described in very general terms and rely on many free parameters, which can be changed *ad*

*hoc.*

The four models are shown schematically in Figure 4.13. In the first and the second models, the observed periodicity is *real.* It may be attributed to some intrinsic periodic process in the source as a result of the orbital motion (e.g. periodic collisions) and the disk oscillation. In the remaining two models, the periodicity is *apparent.* It stems from the modulation of the observed radiation due to geometric and kinematical effects of the orbital motion ( e.g. occultations, Doppler effects) of "a light" and "a screen".

*a) Collision model*

A star (or a small black hole) moves along the central black hole on an orbit across the accretion disk. Periodic collisions of the star with the disk produce periodic flares of the X-ray radiation. However, both the Lense-Thirring precession of the plane of the orbit and the orbital momentum changes due to the collisions will make the orbit coplanar with the disk on a relatively short timescale (Syer, Clarke and Rees 1991). A star on a non-circular orbit in the plane of the disk may locally produce (quasi-periodic) changes in the accretion rate which may appear as X-ray flares. However, the orbit will be quickly circularized (Syer, Clarke and Rees, 1991). Because the physics of the star-disk interaction depends on many factors which can hardly receive due consideration, the shape of the light curve cannot be calculated within this model.

*b) Accretion disk pulsation*

Another type of intrinsic process, which may give rise to short term variability of NGC 6814, is propagating modes or shock waves. The acoustic waves are amplified by the non-conservative effects such as viscous stress and viscous heating. It was found that the oscillation with frequency $\sim 10^{-4}$ Hz could be excited near

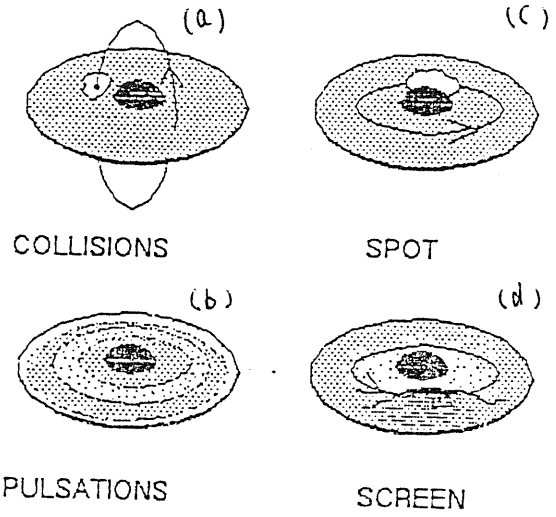


**Figure 4.13:** Four types of the model: (a) Collision model, (b) Accretion disk pulsation, (c) Orbiting spot model, (d) Orbiting screen.

the inner edge of the disk, and that the shock wave propagates there inwards and outwards quasi-periodically. The light curve was presented but the flares had no fixed shape during time evolution. This model was proposed by Honma, Matsumoto and Kato (1992) and separately by Wallinder (1991).

*c) Orbiting spot model*

A single bright spot (or a few spots) is present on the surface of the inner part of the accretion disk orbiting a supermassive black hole. The observed X-radiation from the spot is modulated either by the Doppler effect, by the gravitational focusing of light by the central black hole, or by the occultations of the spot by a more distant part of the disk. A specific light curve depends on the brightness and shape of the spot (or spots), its orbital radius, inclination of the orbit, the shape of the disk, and the mass and angular momentum of the central black hole. When these parameters are assumed, the shape of the light curve can be directly calculated. In its simplest version, the model consists of a single, very small and bright spot orbiting a nonrotating black hole along a circular orbit. It depends on *two* free parameters: the radius of the orbit $r$, and the inclination angle of the orbit. Because the number of the free parameters is so small, fitting the calculated light curve to the data is a meaningful procedure.

*d) Orbiting screen*

A local and non-axially-symmetric elevation of the surface ("the screen") is present somewhere in the outer part of the accretion disk, at a grazing angle to the line of sight. The screen takes part in the disk orbital motion and thus periodically obscures from the view the bright inner part of the disk. The resulting light curve depends on the shape, rotation and brightness of the disk and can be directly calculated when these functions are given. The model was first proposed by C. Done, K. Koyama, H. Kunieda, G. Madejski, R. Mushotzky, and T.J. Turner (1991).

To make a choice between different models one should examine, above all, those predictions which depend as little as possible on the dissipative processes

which is not yet well-understood. This is made practically possible only by fitting the calculated features of the model to the short-term observational data: variability of the X-ray continuum and its closely related variability of the fluorescent iron line and the character of the line itself.

### 4.3.2 The comparison of different models

The characteristics of NGC 6814 are mainly displayed in its light curve and line profile. The prediction about any particular model of NGC 6814 should be consistent with the observational data. For this reason, here we give a rough comparison of the the models. Table 3 presents the predictions on four different models shown in Fig. 4.13. The comparison is made in terms of the variability of the light curve, the shape of the light curve, the correlated variability of the line and the continuum, and natural width of the line profile.

It should be noted that the phase-invariant/variant of the centroid of the iron line may be an important parameter for the comparison of different models. Since current observations are not accurate enough to offer any convincing results about it, it is not listed in the table. Needless to say, the following description is biased to our point of view.

The four models may all explain the periodic phenomenon in NGC 6814, although the light curve of model (a) is still uncertain. In the "hot spot" model (c) the hard X-ray source is imbedded inside the "cold" accreting matter, the iron line is expected to form near the X-ray sources, and the variation of the fluorescent iron is therefore correlated with the X-ray continuum. Since the hard X-ray source is so close to the accreting matter, any delay of the variations between the iron line

Table 3. The predictions about different models

| Models | (a) | (b) | (c) | (d) |
|---|---|---|---|---|
| Light curve | periodic; unknown shape. | periodic; non-fixed shape | periodic fixed; symmetric. | periodic; dips, fixed. |
| Line–continuum correlated? | unclear, | unclear, | Yes; with zero delay | unclear |
| Nature width | may be explained | may be explained | can be explained by disk eclipse | may be explained by a thick disk |

flux and X-ray continuum, if exists, is expected to be very small. Model (a) and model (b) can easily account for the narrow width of the line profile by adjusting the inclination of the system so that the Doppler broadening weakens. If the data obtained by Ginga is absolutely correct, model (b) with a thin disk should be rejected, because this highly inclined system tends to make the line width much larger than the observed value. For this reason, this model can be applied only to a relatively thick accretion disk. For model (c), Doppler broadening gives line width $\sim$ 1.4 KeV (Abramowicz, 1992), but this value can be greatly reduced by the disk self-eclipse. A further comparison can be found in Appendix C.

So far, no light curves with disk self-eclipse and their power spectra have

been fitted with the observational data. All of the results presented here are still preliminary.

Part of the work presented in this chapter is adapted from
Abramowicz et al 1991,1992.

# Chapter 5

# Correlated soft and hard X-ray variability of NGC 5548

## 5.1 Introduction

NGC 5548 is a low luminosity ($L_x \sim 4.5 \times 10^{43}$ erg s$^{-1}$) and a close-by Seyfert I galaxy (z=0.016), which was observed extensively at all wavelengths (e.g. Wilson and Ulvestad 1982, Edelson and Malkan 1986, Taylor et al. 1988, Turner and Pounds 1989, Clavel et al. 1991). It is one of the few AGNs for which the correlation of short–term variability in different energy bands and that of the variability between lines and continuum emission have been investigated in some detail (Kaastra and Barr 1989, Walter and Courvoisier 1990, Nandra et al. 1991, Clavel et al. 1991, Peterson et al. 1991, Clavel et al 1992 ). This is a powerful tool for constraining emission models. The source was extensively studied in X-rays with various missions (Tananbaum et al. 1978, Cooke et al 1978, Rothschild et al. 1979, Mushotzky et al. 1980, Taylor et al. 1988, Nandra et al. 1991 and references therein). In particular, it was observed twelve times with the EXOSAT satellite in the period 1984–1986 for a total exposure time of more than 200 hours (see Table 1). Because of the long orbital period and wide spectral

range (0.05-50 KeV) covered by EXOSAT, these observations are particularly well suited for studying correlated variability in the X-ray band, even in timescales of hours or less. Large variability among the various epochs and within each epoch was clearly seen. Analysis of the variability has been performed by many. Branduardi-Raymont (1988) showed that the source is softer when it is brighter, a property common to a number of Seyfert Galaxies. Variability on timescales of hours was studied by Kaastra and Barr (1989), who looked for delays between the variation at soft and medium X-ray variability, suggesting that soft X-rays lead by $\sim 4600 \pm 1200$ seconds. This result, if comfirmed, would have profound theoretical implications, favoring models where the medium energy X-rays are produced by Compton scattering off the UV, soft X-ray photons by electrons in a hot corona (e.g. Kaastra and Barr 1989, Maraschi and Molendi 1991 ). Walter and Courvoisier (1990) reexamined the same data with a different procedure and confirmed the Kaastra and Barr results. Some confirmation was given also in the Nandra et al. (1991) paper.

Recently, by using cross-correlation technique, Tagliaferri et al. (1991) have searched for delays within the X-ray band in the EXOSAT data of the BL Lac object PKS 2155-304 and found a number of effects that can reproduce a spurious final net delay. Because of the importance of the findings of Kaastra and Barr (1989), we reconsidered the EXOSAT observations of NGC 5548 using the same techniques adopted for the analysis of PKS 2155-304.

In section 2, after a brief description of the instrumentation and observational procedure of EXOSAT, we describe the light curves and the method used for a cross correlation function (CCF) analysis in different X-ray energy bands. The results are presented in section 3 and are compared with previous analyses in

section 4, where some implications on models are also mentioned.

## 5.2 EXOSAT light curves and cross-correlation analysis

The data considered here have been obtained through the EXOSAT database. They refer to two experiments: the low energy imaging telescope (LE) and the medium energy detector (ME). The ME experiment consisted of an array of 8 collimated proportional counters sensitive to the energy band 1-50 KeV (Turner et al. 1981). In order to measure the background the ME was generally operated with half of the detector always pointed at the target, and half at a nearby source-free region. In the course of the observation, usually lasting 3–4 hours, the two halves were interchanged, a procedure indicated as *array swap*. The LE telescope was used with a Channel Multiplier Array (CMA) at the focal plane. The CMA was sensitive to the 0.05-2.0 keV energy band and had no intrinsic energy resolution (de Korte et al. 1981), however, a set of filters with different spectral transmission could be interposed in front of the detector.

A list of EXOSAT observations of NGC 5548 is reported in Table 1, where the first column gives the observing date and a letter identifying each observation, the second column gives the ME exposure time, the third column gives a quality flag (QF) for the ME * data, the fourth gives the number of array swaps, the fifth gives the average 1-8 keV ME count rates and columns six to eight give the exposure

* The data products stored in the EXOSAT database have been given a quality flag ranging from 0 to 5 (0=unusable, 5=excellent). Data with quality flag between 3 and 5 are to be considered of sufficiently good quality to be acceptable for scientific analysis (see The EXOSAT Database System: available database).

**Table 1**

| Date | ME exp. | QF | No. | $cts\ \ s^{-1}$ | AlP | Bor | 3Lex |
|---|---|---|---|---|---|---|---|
| | *s* | | | | *s* | *s* | *s* |
| 84/032(A) | 17010 | 3 | 0 | 3.32±0.18 | 1902 | 7153 | 3202 |
| 84/062(B) | 32630 | 4 | 0 | 4.44±0.04 | 3483 | 3679 | 2763 |
| 84/141(C) | 36540 | 1 | 0 | 3.96±0.05 | 8391 | 14996 | 7111 |
| 84/193(D) | 59430 | 4 | 3 | 2.88±0.03 | 11872 | 26488 | 11053 |
| 85/014(E) | 22100 | 2 | 1 | 4.27±0.04 | 3847 | 10625 | 4219 |
| 85/062(F) | 26800 | 3 | 1 | 3.65±0.04 | 4434 | 11413 | 4605 |
| 85/159(G) | 25750 | 3 | 1 | 1.43±0.05 | 6675 | 9915 | 3824 |
| 85/173(H) | 17020 | 4 | 2 | 3.03±0.05 | 4252 | 6672 | 3311 |
| 85/186(I) | 23370 | 4 | 1 | 1.82±0.04 | 3613 | 10963 | 3095 |
| 85/195(J) | 19020 | 4 | 1 | 1.35±0.05 | 4040 | | 2622 |
| 86/019(K) | 59860 | 4 | 3 | 4.97±0.02 | | 3469 | 39037 |
| 86/062(L) | 83830 | 3 | 6 | 3.82±0.02 | 2392 | 4017 | 69809 |

times in the Aluminium/Parylene (AlP), Boron (Bor) and thin-Lexan (3Lex) LE filters.

In order to study the delay between the various bands, we have correlated the LE light curves (0.05-2 keV) with the ME light curve (1-8 KeV, no source signal is observed at higher energies); this is indicated as ME/LE correlation. We have also correlated the 1-3 keV to the 3-8 keV bands (ME/ME correlation); this subdivision of the ME range gives NGC 5548 comparable count rates in the two bands. In our analysis we have considered all observations with the ME quality factor $\geq 3$, which excludes observations C and E. For the LE we used only the light curves obtained with the 3Lex filter. For the ME/LE analysis, only two of

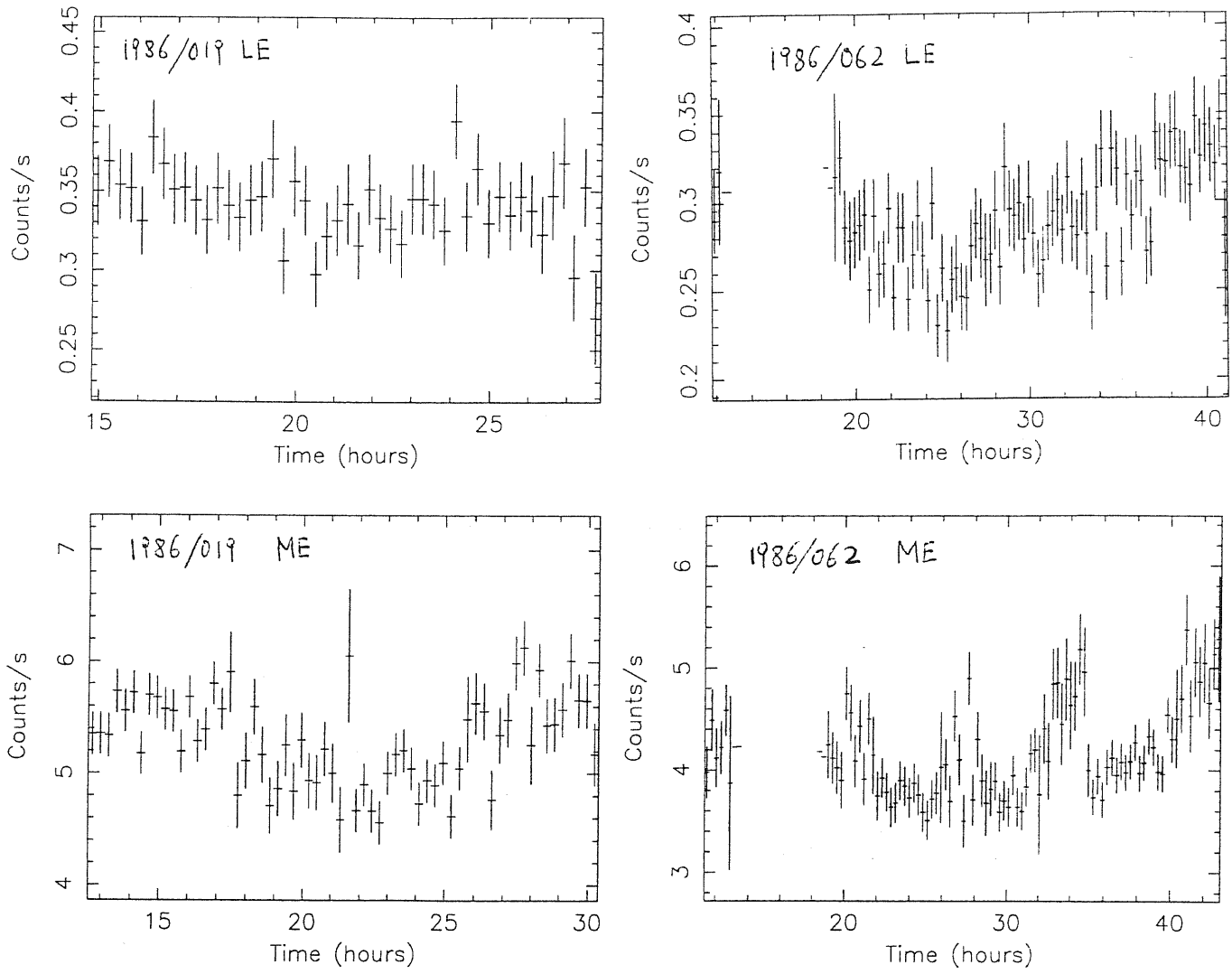


**Figure 5.1.** The ME and LE light curves of 1986/062 and 1986/019 with bin time 1000 s.

the twelve observations are long enough and satisfy data quality requirement: the

observations K and L. In fact, these observations were rather long and the 3Lex filter was used for most of the observing time. In Fig. 5.1 we report the LE and ME light curves for these two observations. Both LE and ME flux of the two observations show variability on a time scale of a few hours with an amplitude of several tenths. The variation of LE and that of ME flux are correlated but they are not perfect. The big gaps seen in the LE and ME light curve are due to the detectors off the source. Observation B and D are also rather long, but the LE light curves are broken in different filters and are therefore not suitable for a ME/LE CCF analysis. We used observations B, D,F, G, H, I for the ME/ME CCF analysis.

Following the analysis of PKS 2155-304 (Tagliaferri et al. 1991) we have identified a number of effects that may affect the CCF. They are briefly summarized here(for a longer discussion, see Taliaferri et al, 1991). The start and end time of LE and ME light curves normally differ from a few minutes to tens of minutes, and one should make sure that the two light curves considered are simultaneous, disregarding parts of the data that are not. Another source of discontinuity is the array swap procedure. This in fact implies that the ME light curves are interrupted by gaps of typical duration of 15 minutes. Although these durations are short with respect to the rest of the light curves, the effect on the CCF can be serious. The best procedure appeared to substitute the gaps with the running average of the light curve calculated over a duration of 1 hour. The array swaps leave also some uncertainties in the background subtraction that are difficult to eliminate. This may be evaluated up to $\pm 0.5\ cts\ s^{-1}$. Such a correction may make the matching smoother between the various segments of the light curves, and, if this proves to affect the CCF by an amount comparable to the eventual net result,

then this result should be considered with precaution.

In our analysis we have used the CCF algorithm contained in the Xronos package (Stella and Angelini, 1991). To derive quantitative information on the possible delays between the variations in the soft and hard X-ray light curves, we fitted the CCF with a constant plus a Gaussian function and determined the position of the Gaussian peak. The uncertainty is at 90% confidence level.

## 5.3 Results

The CC analysis of observation L was performed in two different ways both for the ME/LE and ME/ME correlation. We first considered the entire LE and ME light curves, with the gaps due to the ME array swaps bridged by running average. Then, we divided the light curve into 3 segments, each segment containing only one array swap. The CCF was calculated for each segment and then the average of the 3 CCFs was made. This treatment effectively removed two gaps from the data used in the CCF analysis.

The results of the analysis of the ME/LE and ME/ME correlations are shown respectively in Fig. 5.2 and

**Table 2a**

| Ob.(L) | Bin(s) | ME-LE | Range (s) | ME-ME | Range (s) |
|---|---|---|---|---|---|
| Total | 960 | -1840 s | -3890 1110 | -2410 | -3880 -1080 |
| Seg. 1 | 960 | ? | | ? | |
| Seg. 2 | 960 | 2780 s | 1210 4360 | -1170s | -2270 -110 |
| Seg. 3 | 960 | -3300 s | -4580 -2090 | -200 s | -1660 1120 |
| Averaged | 960 | +900 s | -260 2040 | -450 s | -1580 670 |

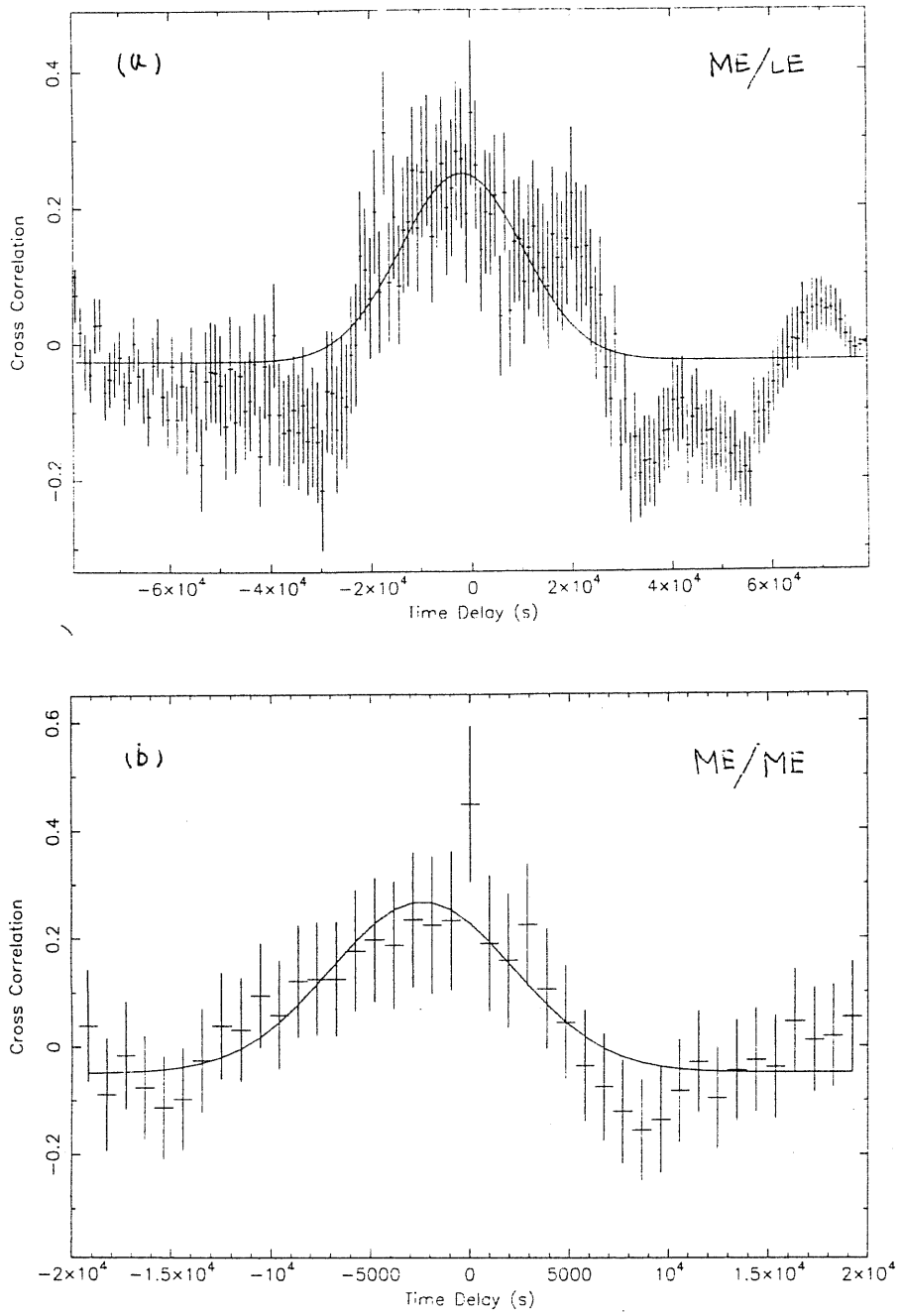


**Figure 5.2a, 5.2b.** The cross correlation functions (CCF) of observation (L) with bin time 960 s (total) (a) and (b) the CCFs of ME/LE and ME/ME.

Table 2a (the sign convention of Gaussian peak is that a lead of softer energies with respect to harder ones is represented as negative).

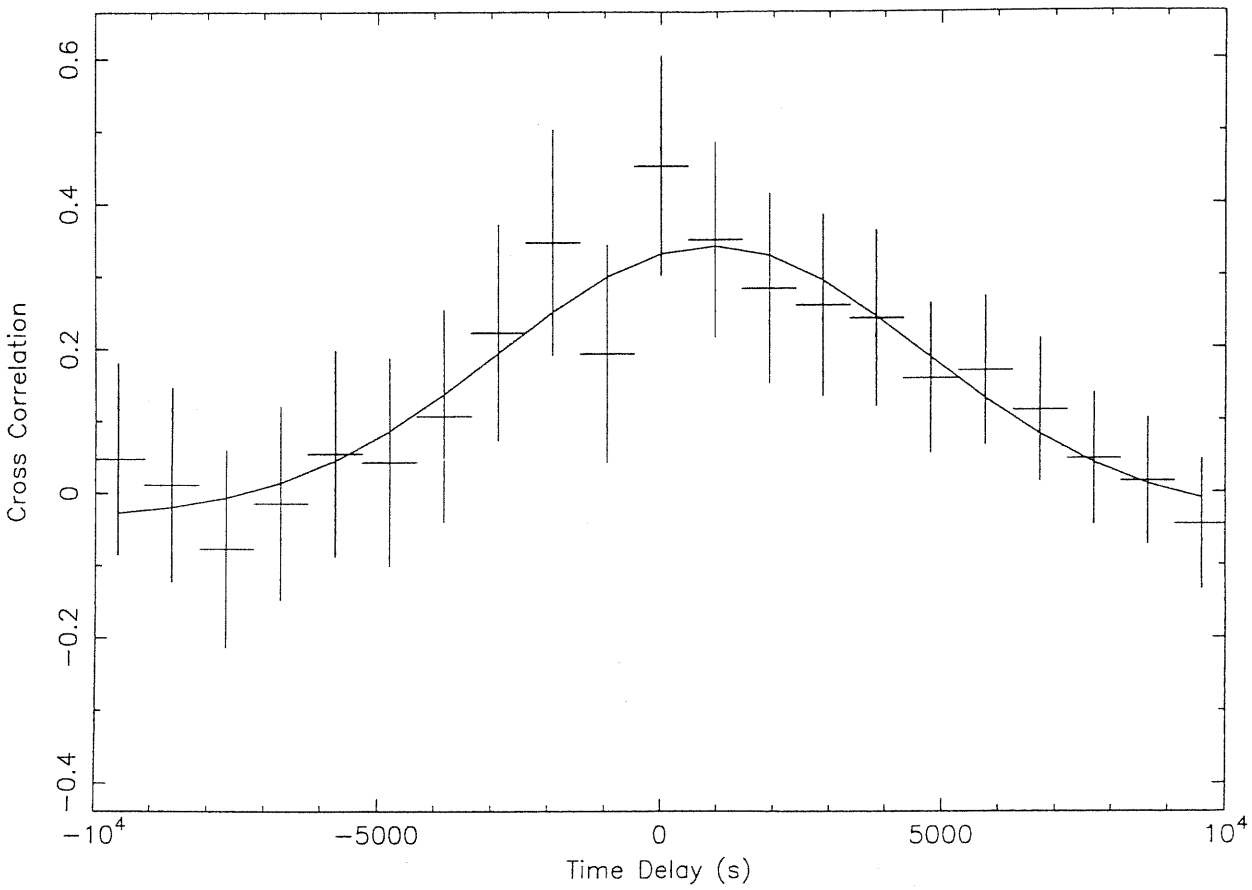


**Figure 5.2c.** The averaged ME/LE cross correlation functions (CCF) of observation (L) with bin time 960 s.

The first column refers to the type of the data we used, column 2 the bin

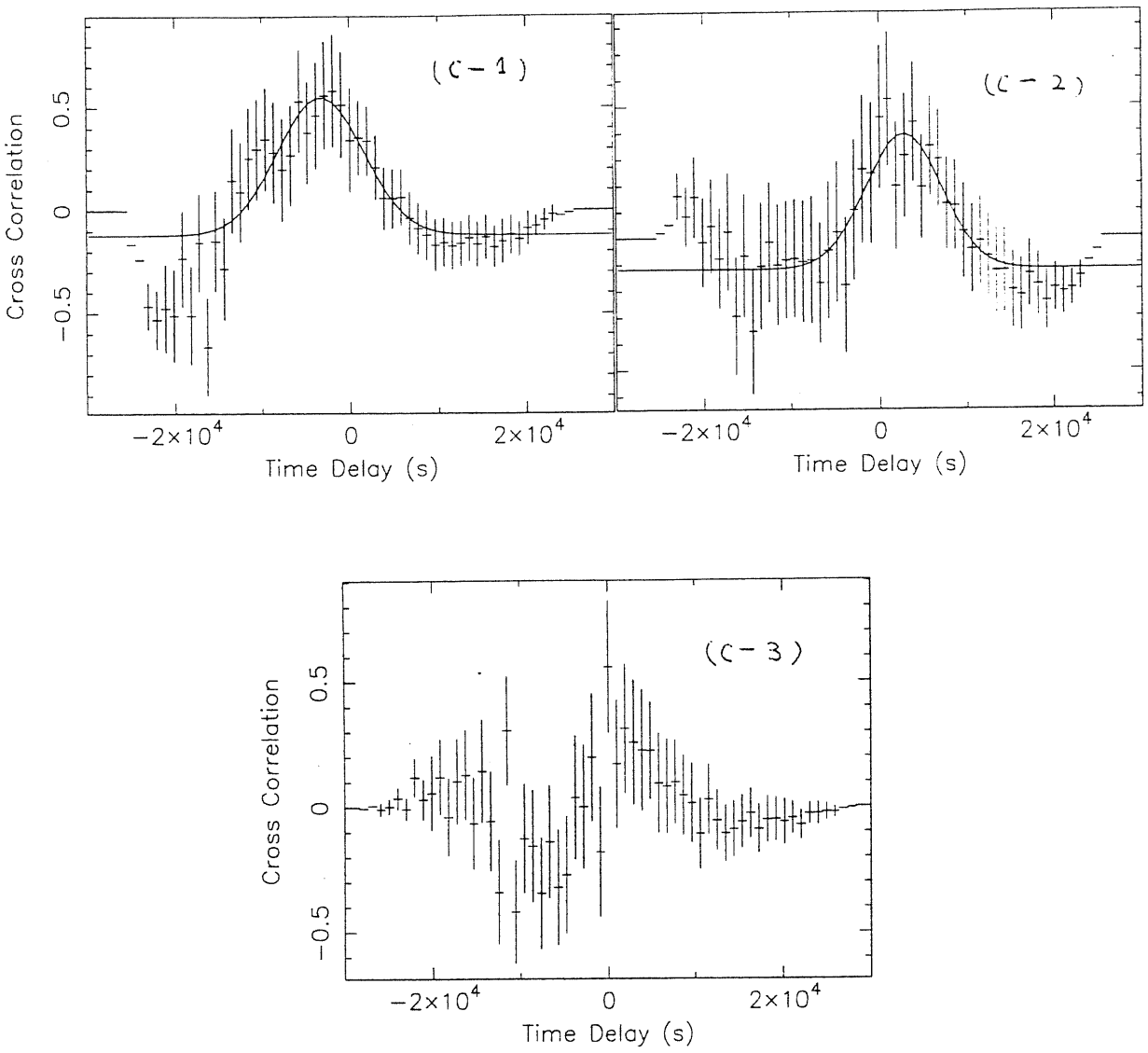


**Figure 5.2c–1,5.2c–2,5.2c–3.** The ME/LE cross correlation functions (CCF) of observation (L) with bin time 960 s for diferent frames.

time of the CCFs, columns 3 and 5 the location of the Gaussian peak for the correlation of ME/LE and ME/ME. Columns 4 and 6 refer to 90% confidence

**Table 2b**

| Obs. | Bin(s) | ME-LE | Range (s) | ME1-ME2 | Range (s) |
|---|---|---|---|---|---|
| K | 1080 | 260 s | -2670 2990 | -790 | -2120 5380 |
| B | 1000 | | | -2280 | -3180 1350 |
| F | 1000 | | | +200 | -2600 2980 |
| G | 1000 | | | +3450 | 2100 5400 |
| H | 1000 | | | +1900 | -200 4500 |
| I | 1000 | | | -2380 | -3700 1143 |

ranges of Gaussian peaks.

In the treatment of the entire set of data, both CCF of ME/LE and that of ME/ME show a delay less than one hour ( Fig. 5.2a, Fig. 5.2b).

In the segments treatment, CCFs of ME/LE show both a positive and a negative delay, with one CCF being ambiguous but suggesting strongly a positive delay (Fig. 5.2c–1,5.2c–2, 5.2c–3). For the correlation of ME/ME, apart from one case that is ambiguous, the other two cases show a negative delay less than half an hour (Fig. 5.2d–1,5.2d–2,5.2d–3). In the averaged case, the correlations of both ME/LE and ME/ME show no convincing delay (Fig. 5.2c)( the delays are smaller than the bin time used), which are different from that of the cases in the entire set of data.

For observations K, B, F, G, H, I, because of the short duration of the segments between array swaps, we considered only the cross correlation of the entire light curves with the data gaps bridged by running average. The results are shown in Table 2b and in Figs. 5.3 and 5.4. In the observation K, the ME/ME correlation gives a Gaussian peak at -800 s but with a large range of uncertainty. Its CCF of ME/LE is consistent with no delay (Fig. 5.3, Table 2b). Observations B and I

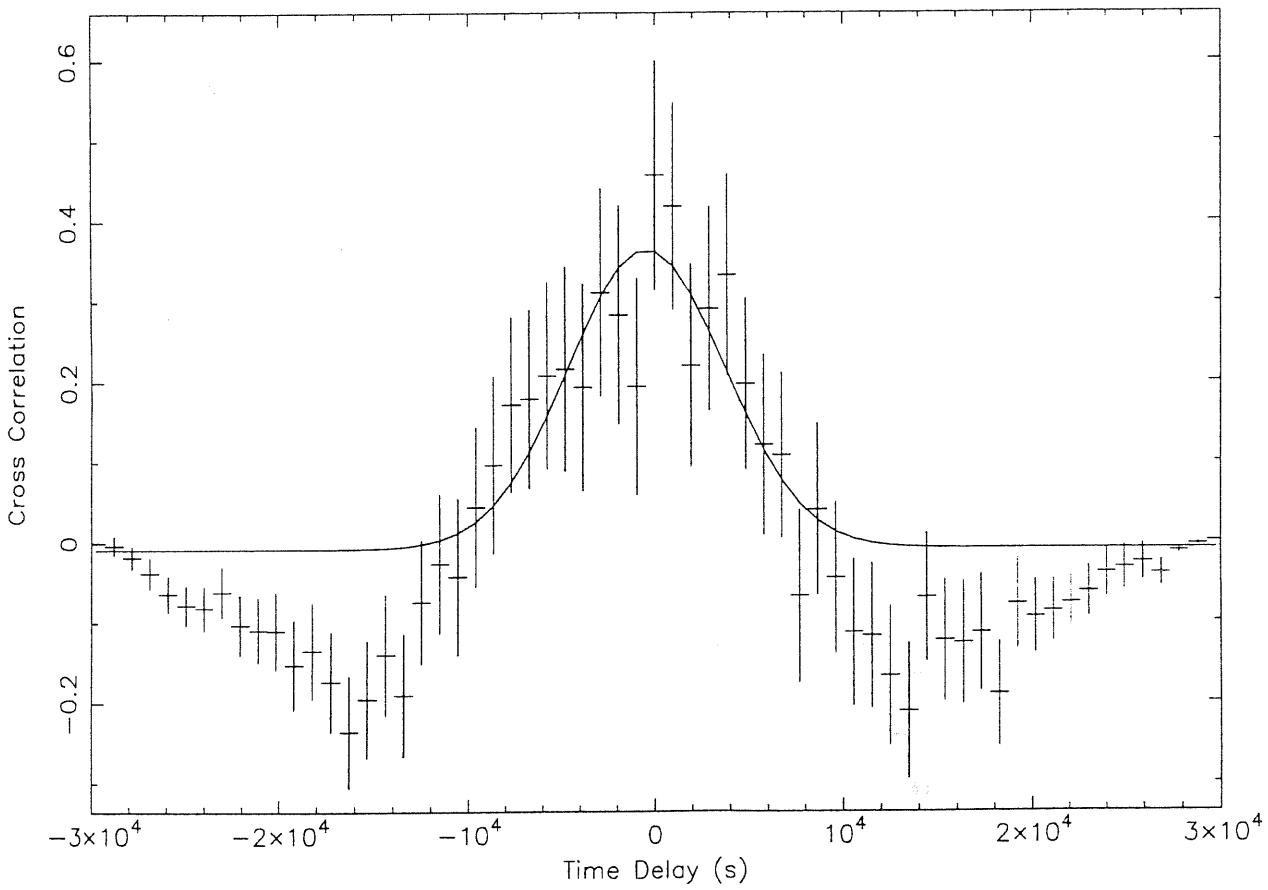


**Figure 5.2d.** The averaged ME/ME cross correlation functions (CCF) of observation (L) with bin time 960 s.

yield a ME/ME CCF with peak value -2300 s and -2400 s delay (Fig. 5.4a, 5.4e), while the observations G and H show a ME/ME CCF with +3500 s and +1900 s delay (Fig. 5.4c, 5.4d). Due to the poor signal-to-noise ratio, the cross-correlation

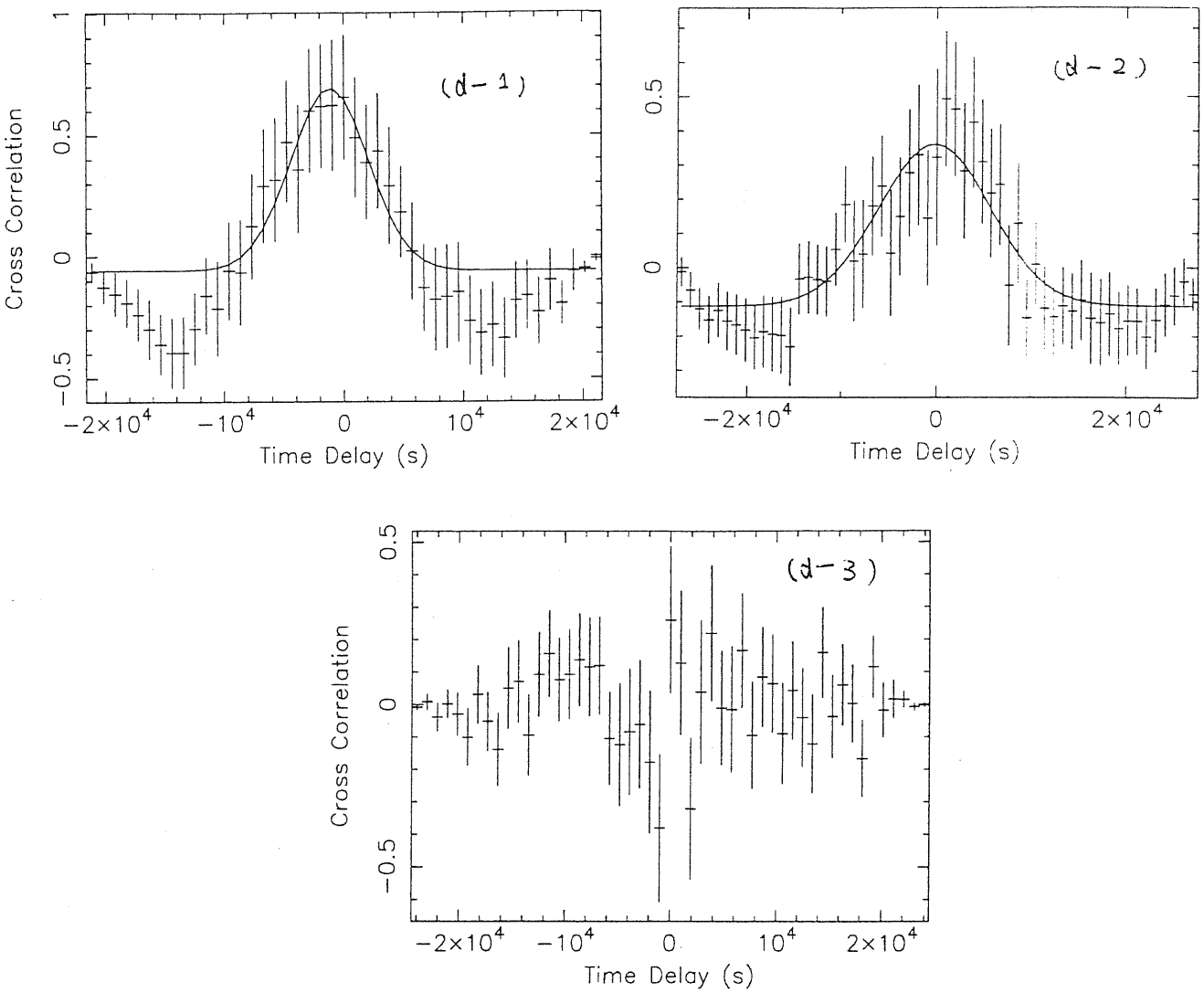


**Figure 5.2d–1,5.2d–2,5.2d–3.** The ME/LE cross correlation functions (CCF) of observation (L) with bin time 960 s for diferent frames.

of observations A, D and J cannot reveal any information about the delay between (1-3 KeV) and (3-8 keV) light curves.

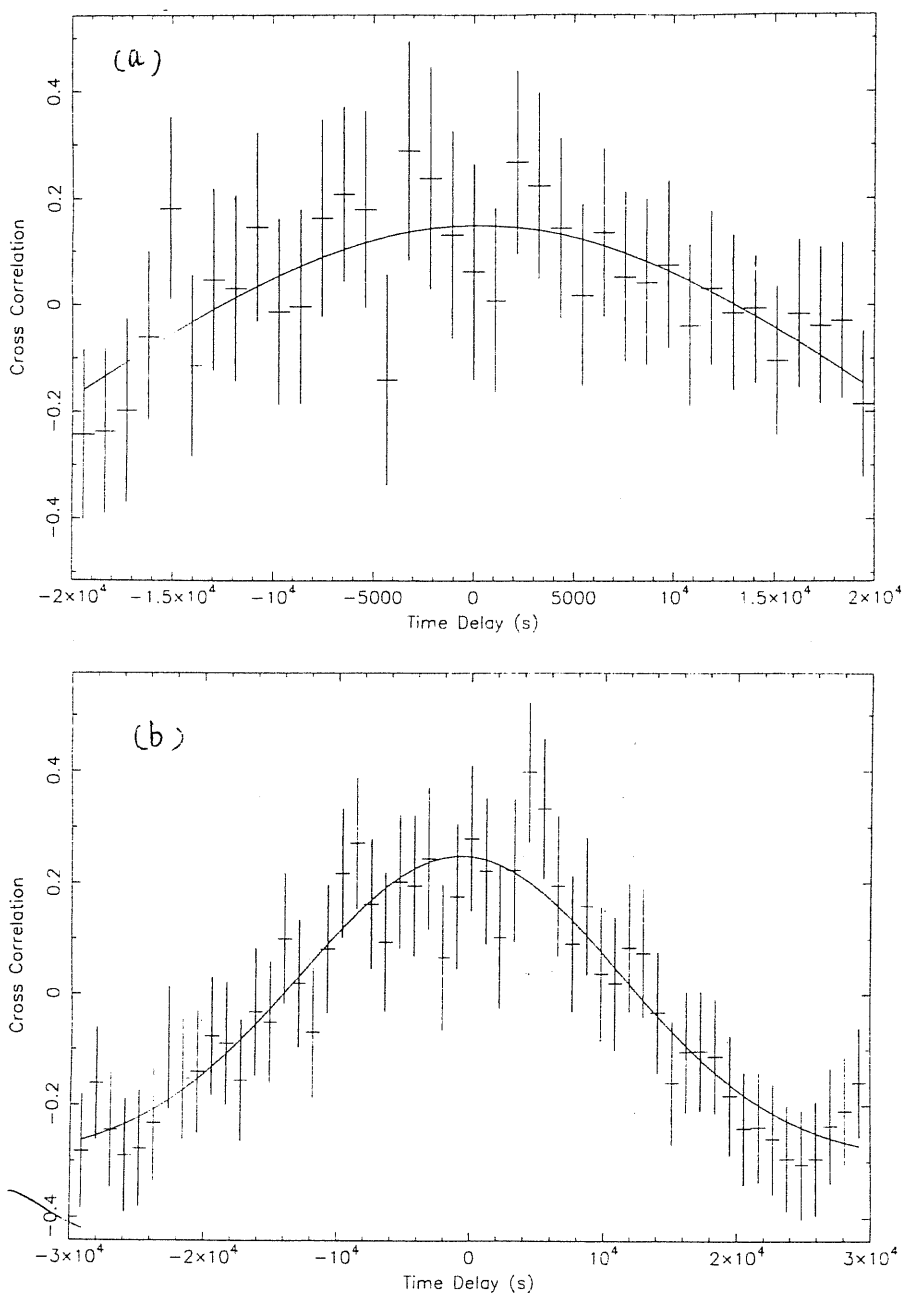


**Figure 5.3.** The CCFs of observation (K) with bin time 1080 s. (a) the CCF of ME/ME. (b) the CCF of ME/LE.

## 5.4 Discussion

The ME/LE, and ME/ME CCFs of observation L considered all together yield a result which, at a confidence level of 90%, is consistent with both negative delay and a zero delay. The CCFs seem to confirm the lag of higher energies with respect to lower ones (about half an hour) in the single treatment. However, the delays are absent from the average of the three segments.

In our opinion, the difference of the results from the two analyses of observation L (full light curve against average of various segments) strongly reflects the spurious origin of the effect, indicating that it may caused by the particular treatment of data gaps in array swaps. Examining our data, we have found that delays of thousand seconds can appear if non strictly simultaneous parts of the LE and ME light curves are considered. Such spurious effects occur also if the backgroud level by a constant as small as 0.5 cts/s is modified. Such a modification may in fact render the CCF more symmetric. The appearance of the positive and negative delay in the short observations, in our opinion, confirms that the time lags obtained by the CCF may have no physical meaning, but are spurious in nature.

Our analysis casts some doubts on the basic result of Kaastra and Barr of a lead of soft X-ray with respect to medium energy. The delay of ME flux with respect to the LE flux may not be intrinsic to the source. It should be mentioned that Kaastra and Barr derived the result by calculating classical correlation function, while Walter and Courvoisier confirmed this by using discrete correlation techniques developed by Edelson and Krolik (1988). However, both groups considered only the total light curve, without any subdivision in segments, and they did not consider the correlation between (1–3 KeV) and (3–8 KeV). Moreover, they did not specify either how the gaps were taken into account.

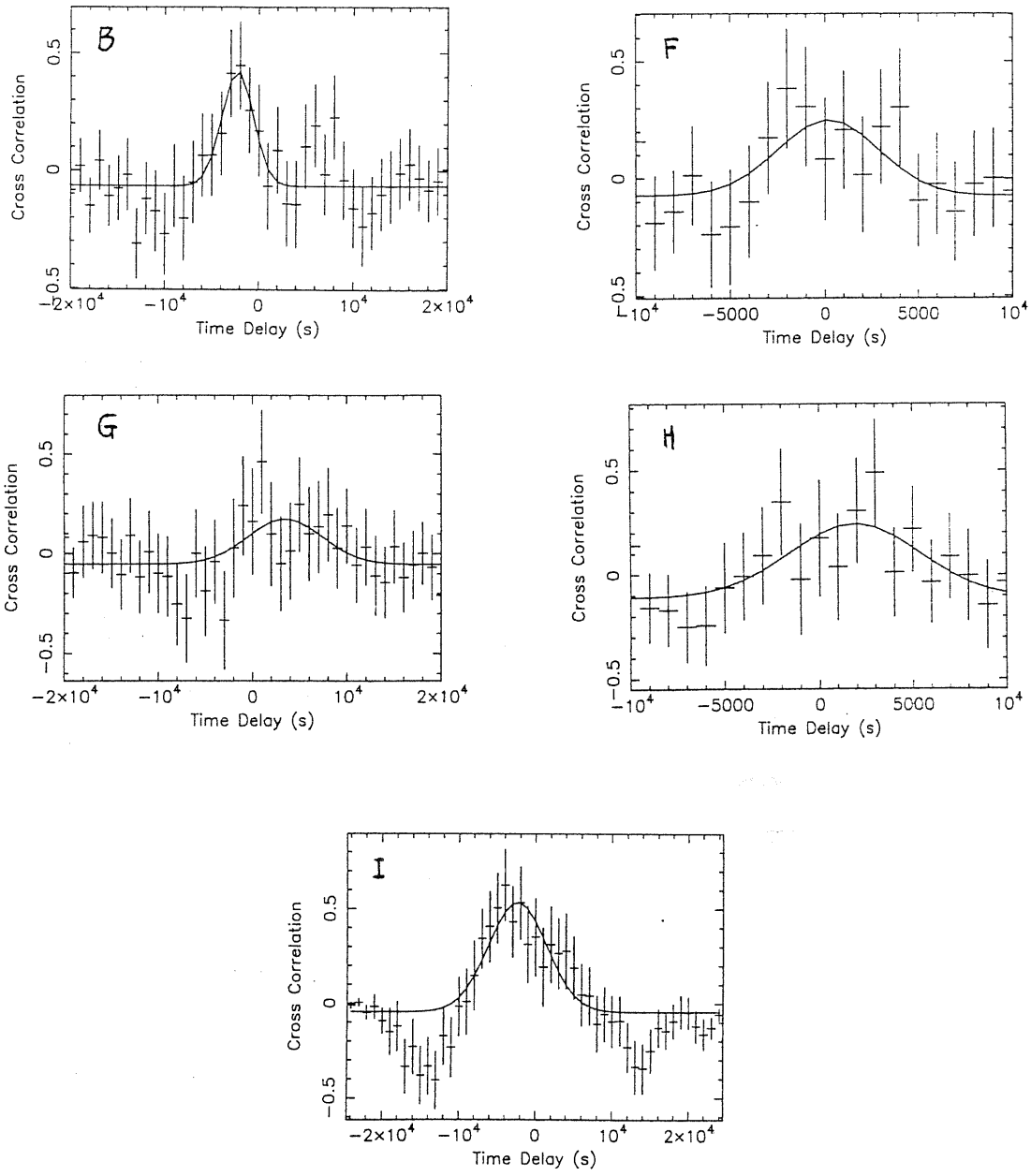


**Figure 5.4.** The CCFs of ME/ME for observation B,F,G,H,I with bin time 1000 s.

The Comptonization model in a hot corona quoted previously in the intro-

duction does not appear to have a direct support from the CCF analysis of the EXOSAT data.

The geometry configuration of AGN, especially the relative location of X-ray source to the reflecting medium has not yet been well defined. Current multi-frequency studies suggest that the primary X-ray sources in NGC 5548 are very close to the dense and cold accreting gas. The phenomenon may be accounted for by the "clumpy" disk model (Fabian and George, 1990, George and Fabian, Pounds and Stewart, 1990 and Clavel et al 1992), in which, the X-ray emitting medium is partially embedded inside magnetically confined blobs of dense and cool gas and the observed UV and soft X-rays contain at least two components; one is from the thermal reprocessing of X-rays and the other from the thermal emission generated by the viscous processes inside the disk. Within the model, the delay between hard and soft X-rays variations are expected to be less than several hundred seconds (corresponding to a distance of several Schwarzschild radii).

(The work is done in collaboration with Treves, Tagliaferri, and Stella)

# Chapter 6

# The Conclusion

In this dissertation, we have presented a detailed study of the "hot spot" model and obtained the result as expected. The *rotation* effect does introduce rapid variability in the light curve and affect the variability power spectrum in the frequency range of $10^{-5} \sim 10^{-3}$ Hz which is related to the orbital frequency of spots. The observed short term time variability is attributed both to the intrinsic property of the disk such as clumps created by the instabilities, the magnetic flares, and to the rotation induced effects such as Doppler effect, gravitational lensing, and accretion disk self-eclipse. Both mechanisms are, in general (if inclination $i \neq 0$), strongly coupled.

The *power-law* variability power spectrum may be accounted for by spots distributed widely on the surface of an accretion disk.

The *statistics* of spots, which may be derived from the accretion disk theory, plays an important part in the model. The number density per unit radius $n(r)$, the life time of spot $\tau(r)$, the brightness $I(r)$, and the rotation law of the disk all control the slope of the power spectrum.

The *inclination angle* of the observer is an important parameter for the observed variability. It plays the role of a "magnifier" (through Doppler effect and gravitational lensing ) that amplifies the intrinsic variability due to the disk itself. Once the statistics of a spot is given, a large inclination angle will introduce a

large variability amplitude, and therefore flattens the variability power spectrum. However, this does not necessarily mean that those sources with large variability amplitude must have large inclination angles, as the observed variability depends also on the intrinsic variability described by the spots statistics.

A detailed fitting of this model with a real source has not yet been carried out, due to the current lack of well-defined parameters. Obviously, both mathematic restrictions on the parameters and theoretical studies on the statistic of spots are needed.

When a few long life time spots occur in a narrow range of the accretion disk surface, the light curve shows periodic flares (for $i \neq 0$), resulting in a *multi-peaked* variability power spectrum. The power distribution among the peaks is associated with the radial coordinate of the orbit, the inclination of the system, the angular distribution of the spots and the geometry of the disk.

This model has been applied to a concrete source. It is suggested that the periodic flares observed in EXOSAT 1985/289 X-ray light curve of the Seyfert galaxy NGC 6814 result from the general relativistic lensing of light emitted by a bright spot ( a vortex, a magnetic flux tube, or something else) orbiting a super massive black hole. The proposed parameters for this source are

$$r \sim 6r_s,$$

$$i \sim 85^o,$$

$$M \sim 9 \times 10^6 M_\odot,$$

where $r$ is the orbit radius of the spot, $i$ the inclination angle of the orbit, and $M$ the central mass of the black hole. The model can be very important, if proved to

be correct. The relative short period $\sim$ 12000 sec indicates the relativistic rotation and thus provides direct observational evidence for the active galactic nuclei paradigm based on a central black hole and a relativistically rotating accretion disk.

Note that since the variability of BL Lac object is thought to be associated with the ejected material from the central part, the model does not apply to that class of objects.

Our analysis of EXOSAT data of Seyfert galaxy NGC 5548 does not show any convincing delay of hard X-ray variation with respect to the soft one. This seems favoring the "clumpy" disk model in which the hard X-ray sources are embedded inside the cold accreting matter.

# Appendix A

## Calculation of the power spectrum

In this appendix, we will use the definition

$$v_i = v \sin i, \tag{A1}$$

for the projected orbital speed of a spot. The light curve of a spot can be represented as

$$u(t) = (1 - v_i \sin \phi_s)^{\pm} E(\phi_s) G(t), \tag{A2}$$

where $I_o$ has been factored out and

$$\phi_s = \Omega_s t + \phi_o + v_i(\cos \phi_o - \cos \phi_s). \tag{A3}$$

Here, we use $E(\phi_s)$ to represent the eclipse,

$$E(\phi_s) = \begin{cases} 1, & |\phi_s - 2n\pi| > \phi_e; \\ 0, & \text{otherwise.} \end{cases} \qquad n = 0, \pm 1, 2 \tag{A4}$$

G(t) is the evolution envelope of the spot intensity due to the intrinsic variability; and we assume that spot has an equal probability of being produced at any orbital position $\phi_o$.

In terms of Fourier transforms of $u(t)$, we can write down the power spectrum for $u(t)$ due to a spot at radius $r$,

$$p(r;\omega) = \frac{1}{4\pi} \int_0^{2\pi} d\phi_o \int_{-\infty}^{+\infty} dt \int_{-\infty}^{+\infty} dt'$$

$$\times(1 - v_i \sin\phi_s)^4(1 - v_i \sin\phi'_s)^4$$

$$\times E(\phi_s)E(\phi'_s)(G(t)G(t')e^{-i\omega(t-t')}. \qquad (A5)$$

To evaluate (A5), we first make a Fourier series expansion of $E(\phi_s)$

$$E(\phi_s) = \sum_n b_n e^{in\phi_s}. \qquad (A6)$$

We also write, for the sake of compactness,

$$(1 - v_i \sin\phi_s)^4 = \sum_{k=0}^{4} \binom{4}{k}(-v_i)^k \sin^k \phi_s, \qquad (A7)$$

$$\sin^k \phi_s = (\frac{1}{2i})^k (e^{i\phi_s} - e^{-i\phi_s})^k$$

$$= \frac{e^{ik\phi_s}}{(2i)^k} \sum_{j=0}^{k} \binom{k}{j}(-1)^j e^{-2ij\phi_s}. \qquad (A8)$$

The orbital position $\phi_s$ may be solved from (A3) by an iterative method,

$$\phi_s^{(0)} = \Omega_s t + \phi_0$$

$$\phi_s^{(1)} = \phi_s^{(0)} + v_i(\cos\phi_0 - cos\phi_s^{(0)}).$$

$$\phi_s^{(2)} = \phi_s^{(0)} + v_i(\cos\phi_o - \cos\phi_s^{(1)}),$$

...

and stopping at the first step. The truncation error for $u(t)$ is

$$\frac{\Delta u}{u} = \frac{4v_i|\sin\phi_s - \sin\phi_s^{(1)}|}{|1 - v_i \sin\phi_s|}$$

$$= \frac{8v_i \left|\cos\frac{\phi_s+\phi_s^{(1)}}{2} \sin\left(\frac{v_i(\cos\phi_s - \cos\phi_s^{(1)})}{2}\right)\right|}{|1 - v_i \sin\phi_s|}$$

$$= \frac{8v_i \left|\cos\frac{\phi_s+\phi_s^{(1)}}{2} \sin\left(v_i \sin\frac{\phi_s+\phi_s^{(1)}}{2} \sin(\frac{v_i(\cos\phi_s-\cos\phi_s^{(1)})}{2})\right)\right|}{|1-v_i\sin\phi_s|}$$

$$= .... \qquad (A9)$$

It is clear that this error approaches zero more quickly than any power of $v_i$ for small $v_i$, which is the case for both neutron star and Schwarzschild black hole system. For $\phi_s \approx \phi_s^{(1)}$, we make a further expansion,

$$e^{-in(n+k-2j)v_i\cos(\Omega_s t+\phi_o)} = \sum_{p=0}^{\infty}\sum_{s=0}^{p}\frac{1}{(2p)!!}\binom{p}{s}$$

$$\times[-i(n+k-2j)v_i]^p e^{i(p-2s)(\Omega_s t+\phi_o)}. \qquad (A10)$$

Similar expansions are made for $(1-v_i\sin\phi_s')^{\frac{1}{4}}$ and $E(\phi_s')$ with the following changes in indices,

$$n \to n', \quad k \to m, \quad p \to q, \quad r \to s, \quad l \to j.$$

Of the three integrals in (A5), we integrate first over $\phi_o$ with the aid of integral representation of the $n^{th}$ order Bessel function

$$J_n(x) = \frac{1}{2\pi i^n}\int_0^{2\pi} e^{ix\cos\psi - in\psi}d\psi$$

and the final result is

$$p(r;\omega) = \sum \alpha_N(v_i)^M J_N(Kv_i)G_{\omega-N_1\Omega_s}G'_{\omega+N_2\Omega_s}. \qquad (A11)$$

Here one should expand the abbreviations $\sum, N, M, K, N_1, N_2$ as follows:

$$\sum \to \sum_{k=0,m=0}^{4}\sum_{j=0}^{k}\sum_{n=-\infty,n'=-\infty}^{\infty}\sum_{q=0,p=0}^{\infty}\sum_{s=0}^{p}\sum_{r=0}^{q}\sum_{l=0}^{m}$$

$$\alpha_N \to \binom{4}{k}\binom{k}{j}\binom{4}{m}\binom{m}{l}\binom{p}{s}\binom{q}{r}b_n b'_n$$

$$\times \frac{(n+k-2j)^p (n'+m-2l)^q (-1)^{p+q+s+r}}{2^{k+m+p+q} p! q! i^{n+n'}}$$

$$N_1 \equiv 2j - k - p + 2s - n$$

$$N_2 \equiv 2l - m - q + 2r - n',$$

$$N = N_1 + N_2$$

$$K \equiv k + m + n + n' - 2(j-l),$$

$$M \equiv k + m + p + q.$$

Corrected to order $v_i^3$ Eq. (A11) becomes

$$p(r;\omega) = 3(3+4v_i^2)\frac{\sin^2\frac{\omega\tau}{2}}{\omega^2} + 4v_i^2\Big(\frac{\sin^2\frac{(\omega-\Omega_s)\tau}{2}}{(\omega-\Omega)^2}$$

$$+\frac{\sin^2\frac{(\omega+\Omega_s)\tau}{2}}{(\omega+\Omega)^2} - (\cos\frac{\Omega_s\tau}{2})\frac{\sin\frac{\omega\tau}{2}\sin\frac{(\omega-\Omega_s)\tau}{2}}{\omega(\omega-\Omega_s)}$$

$$-(\cos\frac{\Omega_s\tau}{2})\frac{\sin\frac{\omega\tau}{2}\sin\frac{(\omega+\Omega_s)\tau}{2}}{\omega(\omega+\Omega_s)}\Big) + O(v_i^4). \qquad (A12)$$

# Appendix B

# A spot orbiting around an extreme Reissner-Nordstrom black hole

To appear in *G. R. G.*

This appendix examines the effects of an extreme Reissner-Nordstrom black hole on the flux radiated by a hot spot corotating with a thin accretion disk around the hole. Here we consider an uncharged source of radiation (hot spot), therefore, only the gravitational field of the hole affects the motion of the source. The case of charged sources of radiation influenced by the electromagnetic field of the hole is discussed elsewhere (Bao and Stuchlik 1992).

## 6.1 The radiation from the spot

The redshift factor $g$ is defined by formula (2.3). Note that the factor $g$ is related to the redshift by $g^{-1} = 1 + z$.

In spherical coordinates and geometric units ($G = c = 1$) the line element of the extreme Reissner-Nordstrom geometry is given by

$$ds^2 = -\left(1 - \frac{M}{r}\right)^2 dt^2 + \left(1 - \frac{M}{r}\right)^{-2} dr^2 + r^2(d\theta^2 + \sin^2\theta d\phi^2). \qquad (B1)$$

(The charge parameter equals the mass parameter, $e = M$, and the inner and outer horizons coincide at $r_h = M$.)

The geodesic motion of test particles (rest mass $m > 0$) and photons ($m = 0$) is determined by the constants of motion $m$, $E$ (energy at infinity), $L$ (angular momentum at infinity), and $\Phi$ (axial component of the angular momentum at infinity) through equations of motion,

$$p^r \equiv \frac{dr}{dw} = \pm\frac{1}{r^2}\bar{R}^{1/2}, \tag{B2}$$

$$p^\theta \equiv \frac{d\theta}{dw} = \pm\frac{1}{r^2}W^{1/2}, \tag{B3}$$

$$p^\phi \equiv \frac{d\phi}{dw} = \frac{\Phi}{r^2\sin^2\theta}, \tag{B4}$$

$$p^t \equiv \frac{dt}{dw} = \frac{r^2E}{\Delta}, \tag{B5}$$

where

$$\bar{R} = E^2r^4 - \Delta(m^2r^2 + L^2), \tag{B6}$$

$$W = L^2 - \frac{\Phi^2}{\sin^2\theta}, \tag{B7}$$

$$\Delta = (r - M)^2. \tag{B8}$$

The affine parameter $w$ is related to the proper time of test particles through $\tau = mw$ .

Due to the spherical symmetry of the geometry (B1), for any test particle or photon, the coordinate system can be chosen in such a way that its motion will be confined to the equatorial plane ($\theta = \pi/2, \frac{d\theta}{dw} = 0, L = \Phi$). Here, accordingly, the coordinates are chosen in such a manner that the disk (with the spot) will be located in the equatorial plane, however, the radiated photons will generally be confined to the other "central" planes.

For the motion of test particles in the equatorial plane, eq.(B2) gives

$$\left(\frac{dr}{d\tau}\right)^2 = \gamma^2 - \frac{\Delta}{r^2}\left(1 + \frac{l^2}{r^2}\right), \tag{B9}$$

where $\gamma$ is specific energy $l$ the specific angular momentum. Therefore, the radial motion is determined by the effective potential

$$V_{eff} = \frac{\Delta}{r^2}\left(1 + \frac{l^2}{r^2}\right). \qquad (B10)$$

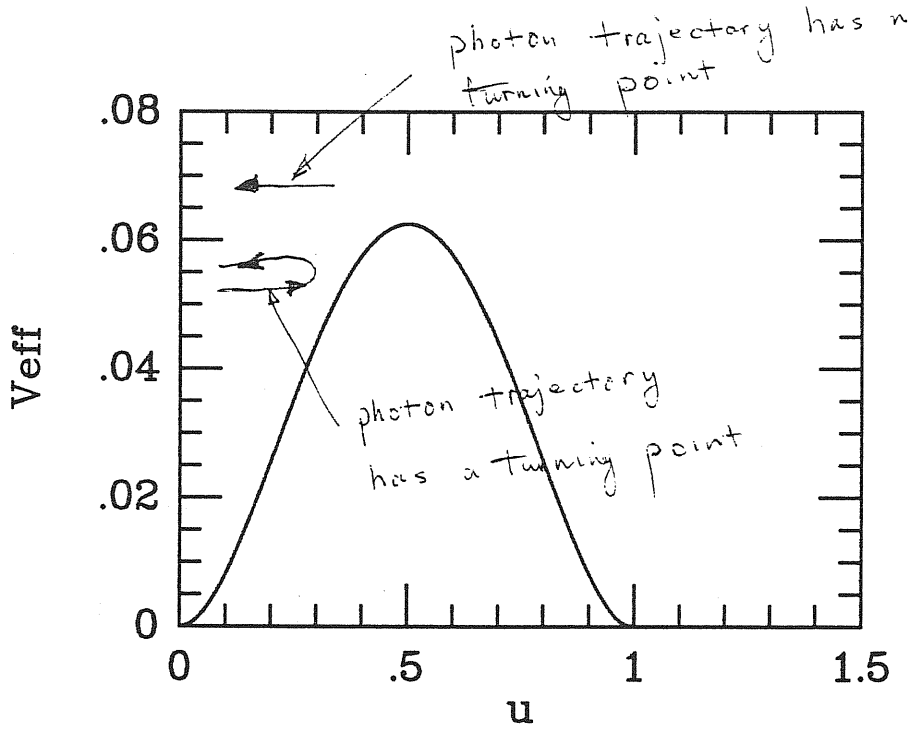


**Fig. B1** The effective-potential diagram for a photon moving around extreme Reissner–Nordstrom black hole.

A particle in a circular orbit (determined by $\frac{\partial V_{eff}}{\partial r} = 0$) at given $r = r_c$ must have constants of motion

$$l_c = \frac{M^{1/2} r}{(r - 2M)^{1/2}}, \qquad (B11)$$

$$\gamma_c = \frac{(r-M)^{3/2}}{r(r-2M)^{1/2}}. \qquad (B12)$$

The angular velocity $\Omega = \frac{d\phi}{dt}$ is for these Keplerian orbits given by

$$\Omega = \left(1 - \frac{M}{r}\right)^{1/2} \left(\frac{M}{r^3}\right)^{1/2}. \qquad (B13)$$

The circular orbits can exist at $r \geq 2M$. At $r{=}r_{cpo}{=}2M$ circular photon orbit is located. Both $l_c$ and $\gamma_c$ diverge at $r = 2M$, however, the motion of photons is governed by another constant of motion - the impact parameter, which is defined as

$$B = \frac{l}{E}. \qquad (B14)$$

For non-equatorial motion of photons, its azimuthal component is

$$B_\phi = \frac{\Phi}{E}. \qquad (B14a)$$

The critical value of the impact parameter corresponding to the photon circular orbit is

$$B_c = 4M. \qquad (B15)$$

The marginally stable circular geodesic orbit (determined by condition $\frac{\partial^2 V_{eff}}{\partial r^2}{=}0$) is located at $r_{ms} = 4M$, it has the specific energy $\gamma_{ms} = \frac{3}{4}(\frac{3}{2})^{(1/2)} = 0.9186$ and the specific angular momentum $l_{ms} = 2\sqrt{2}M$.

Since the 4-velocity of the observer is $u^i_{obs} = \delta^i_t$, the 4-velocity of the spot is

$$u^i_{em} = \frac{(\delta^i_t + \Omega\delta^i_\phi)}{\sqrt{(1-\frac{M}{r})^2 - \Omega^2 r^2}},$$

and the 4-momenta $p_{obs}$ and $p_{em}$ of the photon are determined by (B2)-(B8). We now arrive at the following formula for the redshift factor:

$$g = \frac{\sqrt{(1-\frac{M}{r})^2 - \Omega_K^2 r^2}}{1 - \Omega B_\phi}. \qquad (B16)$$

Clearly, $B_\phi$ is a constant of motion for a given special photon but a variable on the whole, and it changes periodically as the spot moves around the hole. When the spot moves towards the observer, the factor $g$ is amplified and the measured frequency is blueshifted, whereas when the spot recedes from the observer, the frequency is redshifted.

As the method derived in last section, we use the same way to calculate the impact parameter $B$. Combining (B2) and (B4), we find the equation of the photon trajectory to be

$$\left(\frac{du}{d\phi}\right)^2 = \frac{1}{B^2} - u^2(1-u)^2. \qquad (B17)$$

To simplify the computations, we assume that $M = 1$ and introduce a new variable

$$u = \frac{1}{r}. \qquad (B18)$$

The effective potential

$$V_{eff} = u^2(1-u)^2 \qquad (B19)$$

determines the motion of photons in the "equatorial" plane. Its maximum is located at $u = u_c = 1/2$, corresponding to the photon circular orbit, where $V_{eff_{max}} = 1/B_c^2 = 1/16$. If $B^2 < B_c^2$, there are no turning points of the radial motion . For $B^2 > B_c^2$ two turning points exist. The first is at $r_t > 2$ — a photon is repelled there to infinity, and the second is at $r_t < 2$ — a photon is repelled there into the hole.

Using substitution

$$z = u(1-u) \qquad (B20)$$

we arrive at the formula

$$d\psi = \pm\frac{dz}{2}\left[\left(z - \frac{1}{B}\right)\left(z - \frac{1}{4}\right)\left(z + \frac{1}{B}\right)\right]^{-1/2} \qquad (B21)$$

which can easily be reduced to standard elliptic integrals.[1] Considering hot spots moving along stable circular orbits, i.e., at $r_s > 4$ ( $u_s < 1/4$ ), we must distinguish (assuming $B > 0$) the cases $B > 4$ and $B < 4$. In the case $B > 4$, we have to distinguish the photon trajectory with the turning point and that without the turning point. The results can be summarized as follows:

A) $B < B_c$

The deflection angle is determined by

$$\psi_\infty = \left(\frac{B}{2}\right)^{1/2} [F(\eta_{a1}, k_a) - F(\eta_{a2}, k_a)], \tag{B22}$$

where $F(\eta, k)$ are standard elliptic integrals of the 1-st kind, with

$$k_a = \frac{1}{2}\left(2 - \frac{B}{2}\right)^{1/2},$$

$$\eta_{a1} = arcsin\left[\frac{4(1 + Bz_s)}{4 + B}\right]^{1/2},$$

$$\eta_{a1} = arcsin\left[\frac{4}{4 + B}\right]^{1/2}, \tag{B23}$$

and

$$z_s = u_s(1 - u_s). \tag{B24}$$

B) $B > B_c$, with the turning point

Now the deflection angle is given by

$$\psi_\infty = \left(\frac{4B}{4 + B}\right)^{1/2} [2K(k_b) - F(\eta_{b1}, k_b) - F(\eta_{b2}, k_b)], \tag{B25}$$

$$k_b = 2\left(\frac{2}{4 + B}\right)^{1/2},$$

$$\eta_{b1} = arcsin[\frac{1}{2}(1 + Bz_s)]^{1/2},$$

$$\eta_{b2} = arcsin[1/2]^{1/2}, \qquad (B26)$$

$K(k)$ is the complete elliptic integral of the 1-st kind.

C) $B > B_c$ , without the turning point

In this case the deflection angle is

$$\psi_\infty = \left(\frac{4B}{4+B}\right)^{1/2} [F(\eta_{b1}, k_b) - F(\eta_{b2}, k_b)]. \qquad (B27)$$

As assumed in Schwarzschild case, here we consider only photons whose trajectories do not cross the equatorial plane.

Now, for each photon, we have to go back to the "right" coordinate system with the accretion disk in its equatorial plane. Again we can write the deflection angle as

$$\cos\phi_\infty = \sin\theta_o \cos\phi_s,$$

and solid angle as

$$\triangle\Pi = \frac{B}{d^2} \left|\frac{\partial(B,\phi')}{\partial(r_s,\phi_s)}\right| dr_s d\phi_s.$$

The Jacobian contains only $(\frac{\partial B}{\partial r_s})$ and $(\frac{\partial \phi'}{\partial \phi_s})$, we arrive at

$$\triangle\Pi = \frac{B}{d^2}\frac{\partial B}{\partial r}\frac{\partial \phi'}{\partial \phi_s}\Delta r_s \Delta\phi_s,$$

where

$$\frac{\partial\phi'}{\partial\phi} = \frac{\cos\theta_o}{1-\sin\theta_o^2\cos\phi_s^2},$$

and $(\frac{\partial B}{\partial r})$ can be derived as

$$\frac{\partial r}{\partial B} = \frac{\sqrt{\frac{1}{B^2} - u_s^2(1-u_s)^2}}{u_s^2 B^3} \int_0^{u_s} \frac{du}{\sqrt{(\frac{1}{B^2} - u^2(1-u)^2)^3}}. \qquad (B28)$$

For a given observer ($\theta = \theta_o, \phi = \phi_o = 0$) we can numerically solve $B(\phi_s, r_s)$ relation and therefore obtain $B_\phi(\phi_s, r_s)$, for through the geometry (see Fig.1 again) the relation

$$B_\phi = B \sin\theta'$$

still holds. The angle $\theta'$ depends on $\phi_s$ and $\theta_o$ :

$$\sin\theta' = -\frac{\sin\phi_s \tan\theta_o}{\sqrt{1+\sin^2\phi_s \tan^2\theta_o}}.$$

As we discussed before, after knowing the relation $B = B(\phi_s, r_s)$, we can determine the solid angle $\Delta\Pi(\phi_s, r_s)$, the redshift factor $g(\phi_s, r_s)$, and finally the flux $F(\phi_s, r_s)$. The calculation of $\Delta\Pi, g$, and $F$ is done numerically. The results are illustrated in Fig.B1 and Fig.B2, which show these quantities as a function of the azimuthal angle of the spot $\phi_s$ for several values of the radius $r_s$ and the viewing angle of the observer $\theta_o$.

## 6.2 Discussion and conclusion

Fig. B2 shows the light curves, the redshift factor and the solid angle for different viewing angles of $\theta_o$. Cases A,B, C,D refer to the inclination angles $\theta_o = 20^o, 40^o, 60^o, 80^o$. The solid angle has a peak at the angular position $\pi$. As the inclination increases, the peak goes sharper . The peaks are created by the gravitational focusing effect when the spot is exactly behind the hole. The redshift factor has larger variation when the viewing angle increases. One distinctive feature is that the changes of the blueshift are greater than those of the redshift for the same curve, which is more pronounced if the veiwing angle is larger. The changes of the light curves are similar to those of the solid angle, but they are

asymmetric. When $\theta_o = 20^o$, the curve is similar to that in special relativity which is close to the sinusoidal shape. As the $\theta_o$ increases, the position of the peaks becomes closer to $\pi$, which means that the focusing effect dominates the signal.

Fig. B3 shows the light curves, the redshift factor, and the solid angle for different spot positions $r_s = 12M, 20M, 40M$. Cases A,B,C refer to them respectively. Due to the gravitational focusing, the solid angle has a sharp peak at the $\pi$. As the radius of the orbit of the spot $r_s$ decreases, the peak becomes higher but not sharper (Cf. Fig. B1). The variation of the curves giving the red shift factor decreases with $r_s$. This is simply caused by the fact that closer orbits have greater orbital velocity. There is a tendency that maxima go away from $\pi$ with increasing $r_s$. The light curves have a peak near $\pi$ which is not symmetric, because both the symmetric solid angle and asymmetric redshift factor contribute. The peak is getting higher with the radius $r_s$ increasing because of the reduction of the effective emitting area. It shifts closer to $\pi$ with the increase of $r_s$, because the contribution of the redshift factor is surpressed with growing efficiency by the contribution of the solid angle.

It is noticed that in many calculations, no turning point in the photon's trajectory has been found, except for very large viewing angles ( $\theta_o > 85^o$). In this case, the turning point occurs for photons emitted by the spot close to the angular position $\phi_s = \pi$. This is quite different from the Schwarzschild case where orbits with a turning point can appear in a relatively wide range of angles $\phi_s$ near $\phi_s = \pi$.

To test the situation in the strong field near the hole, we consider also the orbit with $r_s = 5M$. We have found that (at given $\theta_o = 60^o$) no photons can

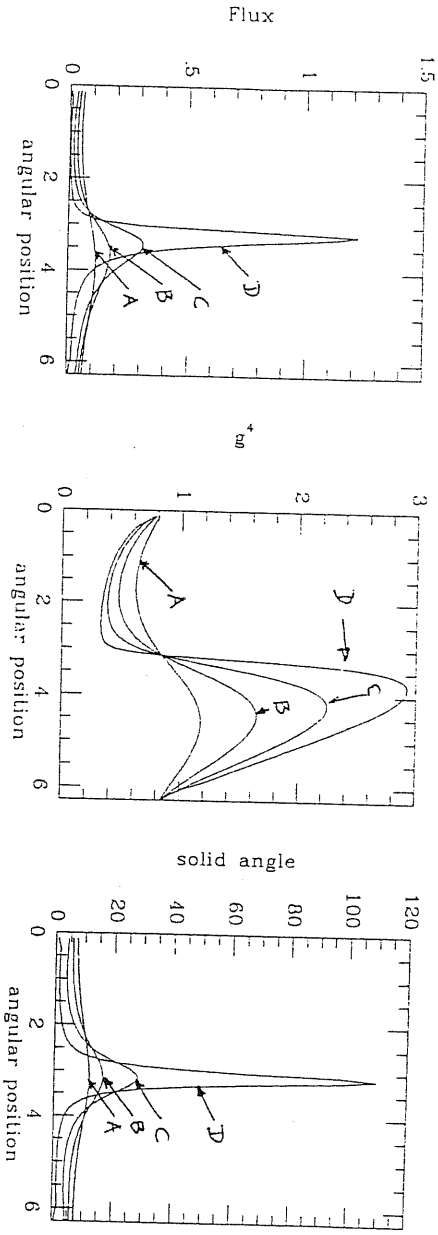


**Figure B2.** The light curves, the redshift factor, and the solid angle against the spot orbit position. The spot is located at $r_s = 12M$. Cases A, B, C, D refer to the inclination angle $\theta_o = 20^o, 40^o, 60^o, 80^o$. The units for light curves and solid angle are arbitrary.

reach the observer if the spot is moving behind the hole at $\phi_s$ going from $158^o$ to $202^o$. For the inward directed photons are captured by the hole if the impact parameter is smaller than $B_c$, and the photons with the impact parameter greater than $B_c$ cross the equatorial plane wherein they are absorbed by the accretion disk. Therefore, the spot orbiting the extreme hole on circular orbits close to the marginally stable orbit can be *eclipsed by the hole* even for moderate inclination angles.

The work is done in collaboration with Z. Stuchlik

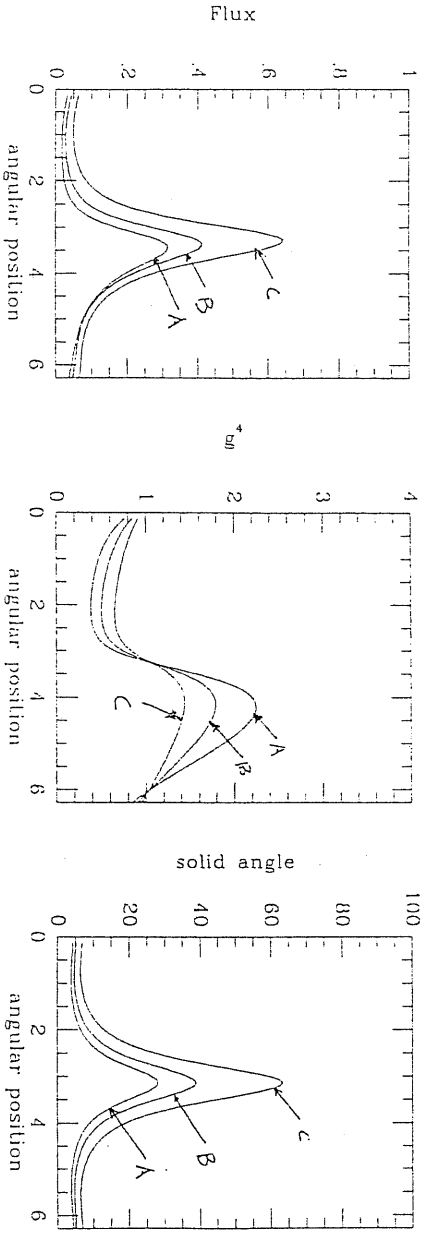


**Figure B3.** The light curves, the redshift factor, and the solid angle against the spot orbit position. The viewing angle of the observer is $\theta_o = 60^o$. Cases A, B, C refer to different spot positions $r_s = 12M, 20M, 40M$ respectively.The units for solid angle and light curves are arbitrary.

# Appendix C

## Similarity of the Variability Patterns in the Exosat and Ginga Folded Light Curves of the Seyfert Galaxy NGC 6814

According to the bright spots model, the brightness of each individual spot may change from period to period, but the positions (orbital phases) of the strong spots should remain fairly constant, although not exactly fixed, as they should reflect the $\dot{P}_0 \leq 10^{-5}$ period stability. Thus, there should be the same variability pattern defined by the strong spots in the *Exosat* and *Ginga* light curves — repeated major flares should occur at almost the same orbital phases independently of their varying amplitudes. As a consequence, phase differences between the major flares should be almost constant in time, *i.e* they should be constant with a similar accuracy as the period is constant in time. Other models do not have these properties. As there is no mechanism which could keep all these secondary effects in phase independently of their varying strength, for a long time there should be no pattern stability — the major flares (except one) *should not* occur always at the same phases. As a consequence, phase differences between the major flares should randomly vary when one compares moments of time remote enough.

We demonstrate in this section that the *Exosat* and *Ginga* data are consistent with a hypothesis that there is a remarkable stability of the phases of three major flares present in the NGC 6814 light curve. If this is confirmed by future *Rosat*

observations, we shall have the proof that the rotation of a stable pattern of spots indeed causes the periodic variability of NGC 6814, and therefore that the active galactic nuclei paradigm involving black holes and accretion disks is basically correct.

1.) The fits to Exosat and Ginga folded light curves

Figures C1 and C2 show the NGC 6814 light curves obtained by *Exosat* (Fiore *et al.*, 1992) and *Ginga* (Done *et al.*, 1992), both folded on the period $P_0 = 12\ 200$ sec. The *Exosat* folded light curve clearly shows one major flare and less clearly several smaller flares, while the *Ginga* light curve shows three major flares and several smaller ones.

We have fitted to both *Exosat* and *Ginga* data several theoretical light curves calculated from the bright spots model. The quality of the fit was assessed by the $\chi^2$ test calculated according to the formula,

$$\chi^2 = \frac{1}{k-n} \sum_{i=1}^{k} \left( \frac{I_{\rm O}(\varphi_i) - I_{\rm M}(\varphi_i)}{\sigma_{\rm O}(\varphi_i)} \right)^2 . \qquad (C1)$$

Here $\varphi_i$, $I_{\rm O}(\varphi_i)$, $\sigma_{\rm O}(\varphi_i)$ are the phases, intensities (measured in counts per second), and errors of the observed $k$ data points, $I_{\rm M}(\varphi_i)$ are the intensities calculated from the model, and $n = 3 \times N + 1$, where $N$ is the number of the spots in the model, and $n$ is the number of the free parameters.

First we found that if the orbital parameters are the same for both *Exosat* and *Ginga*, then the best fit model gives,

$$M = 9 \times 10^6 M_\odot, \qquad r = 6 r_G, \qquad \theta = 85^o. \qquad (C2)$$

We made fits with the orbital parameters (C2) fixed, but with several different numbers of spots and several different spot patterns. The best fits (minima of $\chi^2$

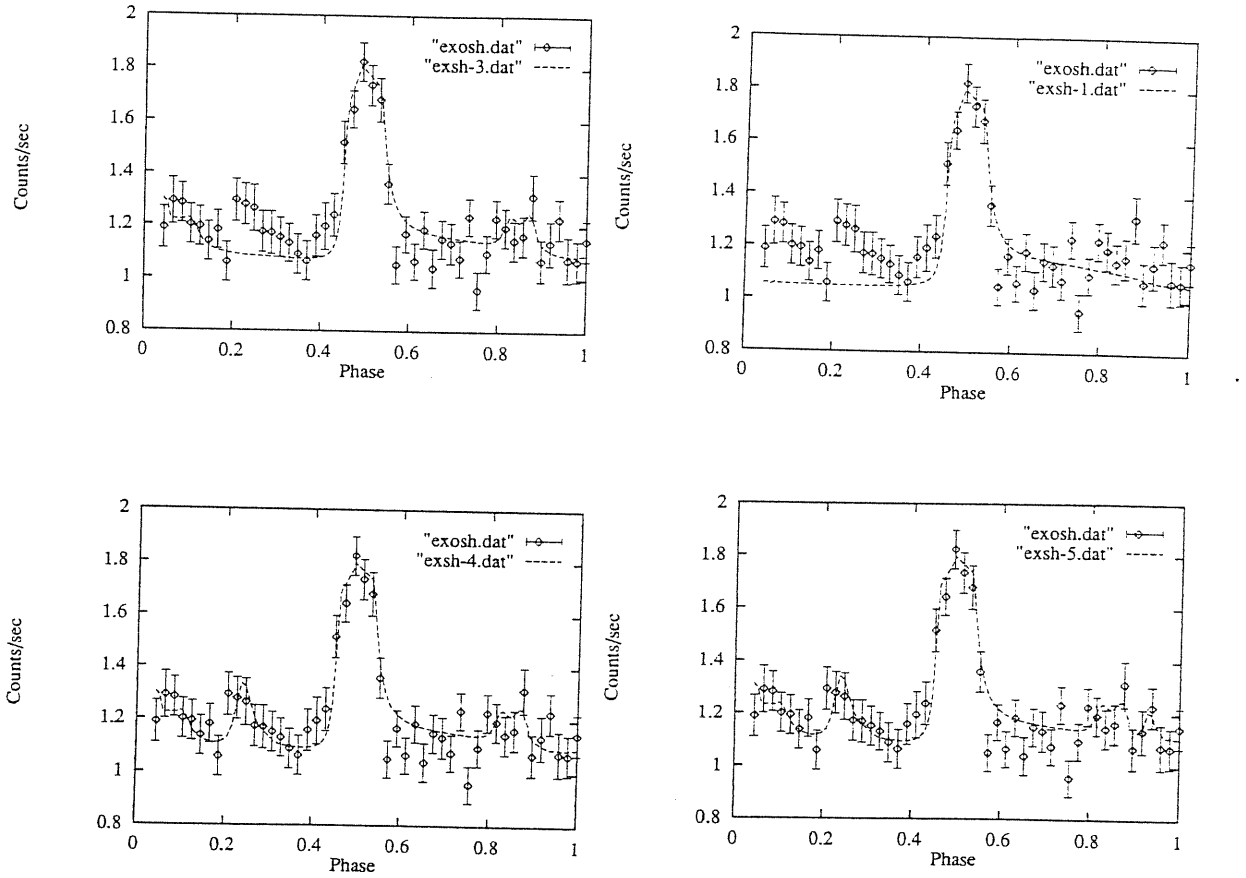


**Figure C1:** The best fits to the *Exosat* folded curve for the bright spot model with $N = 1,\ 3,\ 4,\ 5$ spots. The theoretical curves are shown by the broken lines. The *Exosat* data were collected during the "long look" 1984/289 with the duration of about two days and correspond to photon energies from 2 keV to 6 keV.

with respect to $\varphi_j$, $\Delta\varphi_j$, $I_j$, and with $n = 3 \times N + 1$) for several different numbers of spots are shown in Figure C1 for the *Exosat* fits and in Figure C2 for the *Ginga* fits. Figure C3 shows how the $\chi^2$ calculated from equation (C1) depends on the postulated number of spots. One concludes from these Figures that the fits of the models with 3 or more spots are very good. For *Exosat* data the best fit is given by the model with 4 spots, for *Ginga* the minimum of $\chi^2$ is very shallow and one can say that the best fit is given by models with 5, 6, or 7 spots.

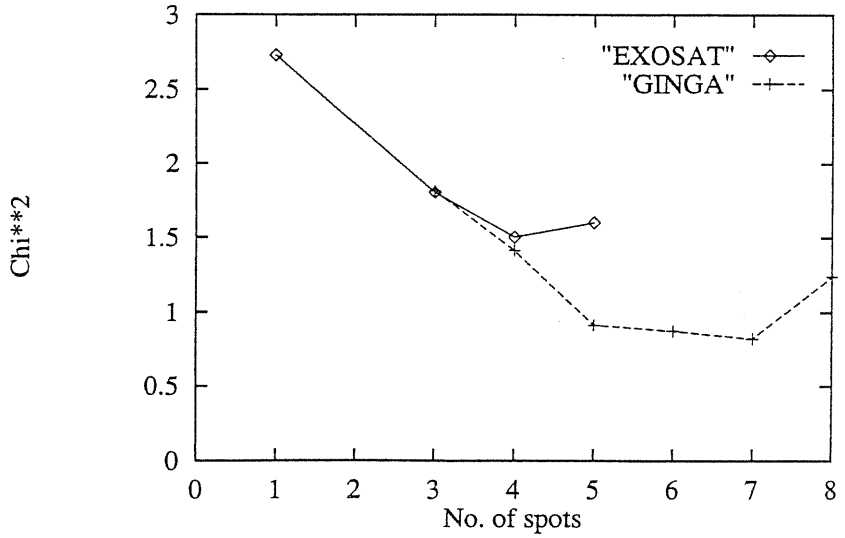


**Figure C3:** The $\chi^2$ values for the best fits to both *Exosat* and *Ginga* folded light curves with different numbers of spots.

Figure C4 shows the locations, sizes and intensities of the spots from the

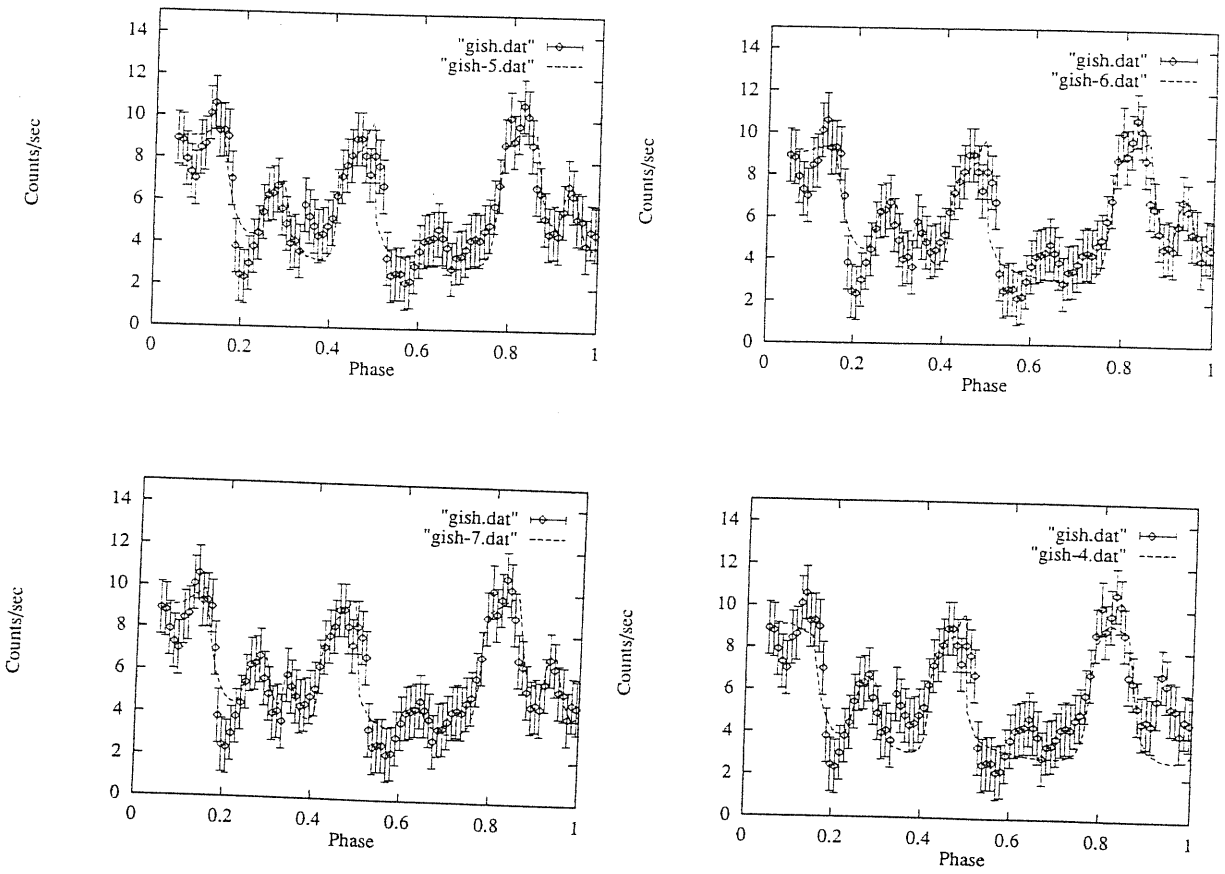


**Figure C2:** The best fits to the *Ginga* folded light curve for the bright spot model with $N = 4,\ 5,\ 6,\ 7$ spots. The theoretical curves are shown by the solid lines. The *Ginga* light curve corresponds to the total duration of about three days and photon energies from 2.24 keV to 5.69 keV.

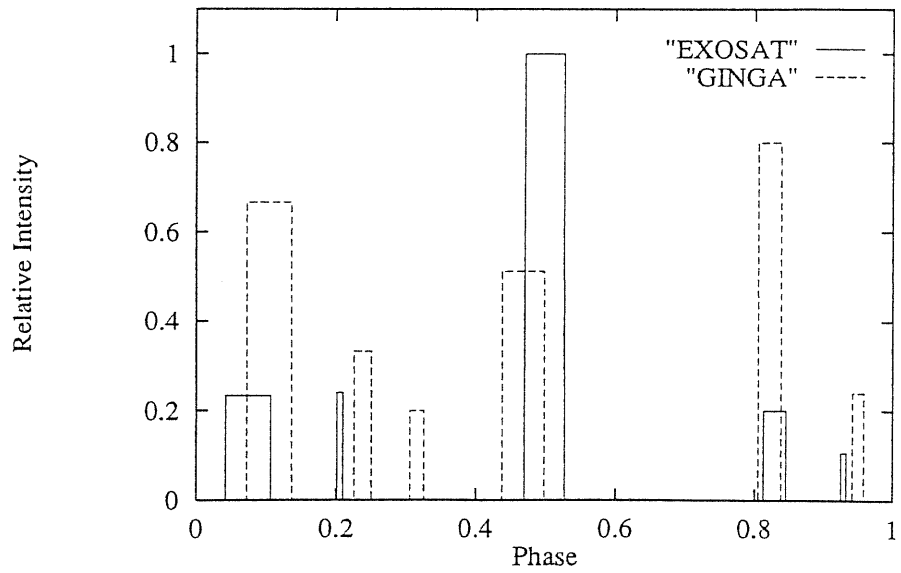


**Figure C4:** The spot patterns used in our model for *Exosat* and *Ginga* fits.

best fit models to *Exosat* and *Ginga* data. The spots are labelled by numbers proportional to the total energy radiated in the corresponding flare. It is easy to see that for both the *Exosat* and *Ginga* data three strong spots can be identified. One also notices that these three spots have very similar phases. The maximal phase difference between the corresponding *Exosat* and *Ginga* spots is $\Delta\varphi = 0.18$ (*i.e.* 10 degree). The question is what is the probability that this coincidence could occur by a pure chance. The simplest estimate of the probability that for two sets of $N$ ordered numbers between 0 and $2\pi$ the differences between corresponding numbers are less than $\Delta\varphi$ is $p_N(\Delta\varphi) \approx (\Delta\varphi/\pi)^N$. This gives $p_3(0.18) = 0.006$,

and thus one may conclude that the coincidence between the major three spots in the *Exosat* and *Ginga* light curves cannot occur by chance.

2.) The probability of coincidence of two N-spot patterns

In the real situation the location of the peaks of the flares in the *Exosat* and the *Ginga* light curves are not truly random, because if two flares are located too close to each other, they would be mistaken for one spot. This means that when the probability is calculated, the *Exosat* and *Ginga* distributions of spots should be compared only with those distributions in which all the spots in one set are separated from each other by more than a given minimal separation $\delta\varphi$. By increasing the minimal separation one increases the probability of the coincidence of the two sets of numbers. Thus, if in a real situation there are several flares separated by $\delta\varphi_0$ or more, one *overestimates* the probability by assuming $\delta\varphi = \delta\varphi_0$, because these flares could still be recognized as separate with a smaller separation constant. Figure C4 shows that all the spots in one set (either *Exosat* or *Ginga*) are separated by more than 0.8 radians. Therefore, the data are consistent with $\delta\varphi \leq 0.8$ (about 30 degree).

Note that in our discussion the absolute values of phases are, of course, irrelevant, because the phases of the spots are known only up to an arbitrary additive constant. Thus, a constant phase shift may be added to all the spots from one set to make better the phase coincidence with the spots in the second set.

In accordance with these remarks we have calculated the probability of the coincidence of the two spot patterns in the following way, which clearly *overestimates* the true probability. Let $x_j$ and $y_j$ for $j = 1, ..., N$ be two random sets of $N$ numbers which are ordered,

$$0 < x_1 < x_2 < ... < x_N < 2\pi, \quad 0 < y_1 < y_2 < ... < y_N < 2\pi, \qquad (C3)$$

and well separated,

$$|x_j - x_{j+1}| > \delta\varphi, \quad |y_j - y_{j+1}| > \delta\varphi, \tag{C4}$$

$$|x_1 + x_N - 2\pi| > \delta\varphi, \quad |y_1 + y_N - 2\pi| > \delta\varphi. \tag{C5}$$

Let us assume that the phases in the second set could be changed by a constant phase shift, $\varphi_0$,

$$z_j = y_j + \varphi_0, \tag{C6}$$

in such a way that the coincidence of numbers from the first set with those from the second, shifted, test is optimal.

We have calculated by Monte Carlo simulations the probability $p_N(\delta\varphi,\ \Delta\varphi)$ that for all $j = 1,\ ...,\ N$ the difference between the numbers in the first and the second (shifted) set are less than $\Delta\varphi$,

$$|x_j - z_j| < \Delta\varphi. \tag{C7}$$

Results of these calculations are presented in Figure C5.

From the fits discussed in this Section and presented in Figures C1, C2, C3, C4, we obtained the probability for $3 \leq N \leq 5$, $\delta\varphi \leq 30$ degrees, and $\Delta\varphi \leq 10$ degrees. As can be seen from Figure C5, this corresponds to the upper limit of the probability that such a coincidence could occur by chance, $p_N(\delta\varphi,\ \Delta\varphi) < 0.04$. Because the probability is small, we conclude that the coincidence between phases of the peaks in the *Exosat* and *Ginga* light curves is real and reflects an important intrinsic property of the source.

Figure C6 shows the vectors corresponding to shifts from the *Exosat* to *Ginga* positions of the spots. The Figure suggests that the spot pattern undergoes systematic rather than chaotic changes. Such a behavior might be connected with some important property of the orbiting objects.

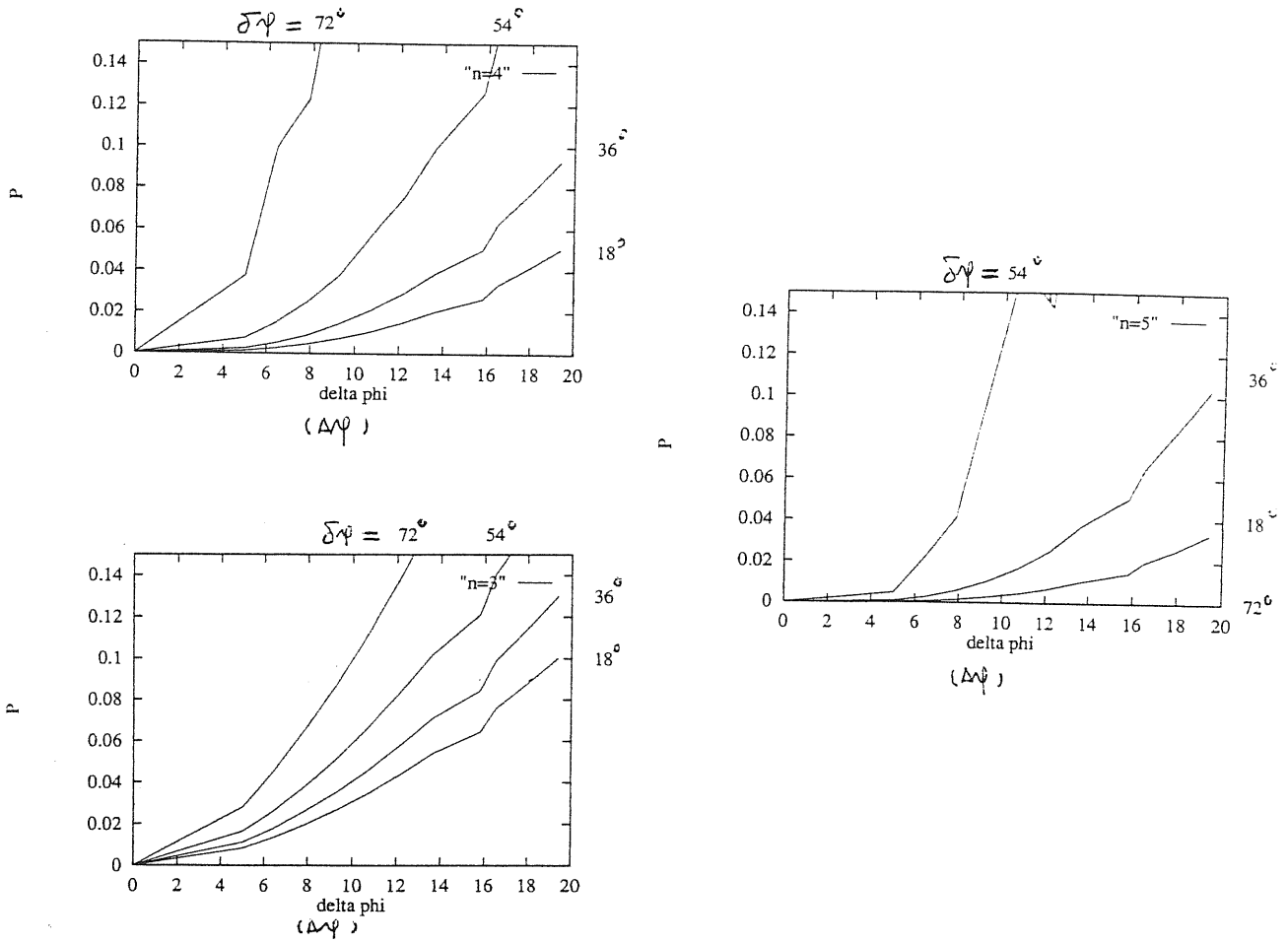


**Figure C5:** Probability $p_N(\delta\varphi,\ \Delta\varphi)$ that two sets of $N$ numbers between 0 and $2\pi$ separated by at least $\delta\varphi$ coincide with accuracy at least $\Delta\varphi$. Both $\delta\varphi$ and $\Delta\varphi$ are given in degrees.

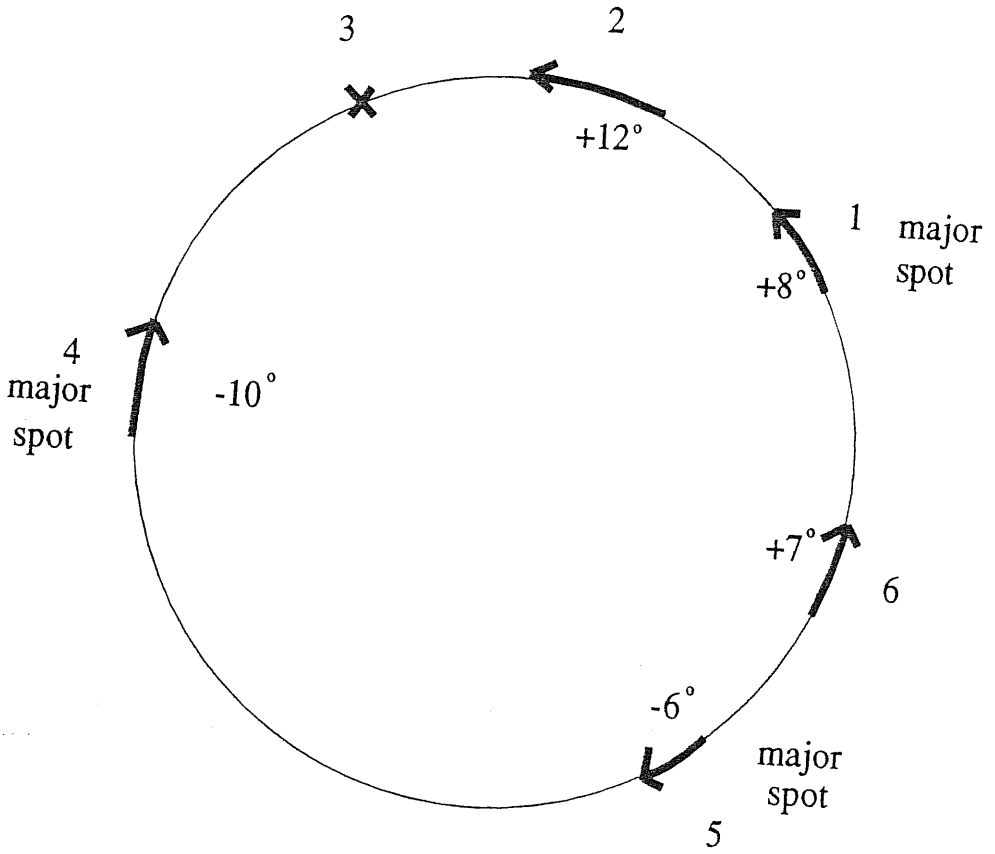


**Figure C6:** Shifts in the spots locations from *Exosat* to 6 years later *Ginga* positions. The shift vectors are exaggerated for clarity. They are labelled with the numbers corresponding to the values of the shifts $(\varphi_E - \varphi_G)$.

## 4. Conclusion

We demonstrated in terms of the $\chi^2$ test that the quality of the fits of the light curves calculated according to the bright spots model to the folded light curves constructed from the data collected by *Exosat* and *Ginga* is very good. In addition, we found that the variability patterns present in the *Exosat* and *Ginga* folded light curves are remarkably similar — the corresponding peaks differ in phase by less than 10 degrees and the probability that this coincidence occurs by chance is less

than 4%. Such a coincidence is expected in the bright spots model, but not in the alternative models. Thus, we conclude that a detailed quantitative analysis of the data directly based on well understood effects of rotation ( excluding poorly understood physics) underlies validity of the bright spots model.

If the stability of the variability pattern (and systematic effects in the shifts) in the *Exosat* and *Ginga* data is confirmed by the *Rosat* observations, the probability that in all three cases the coincidence occurs by a pure chance would be negligibly small and the long awaited unquestionable proof of the correctness of the active galactic nuclei paradigm will be finally at hand.

The work is done in collaberation with

Abramowicz, Lanza, and Karas

# Bibliography


1. Abramowicz M.A., Szuszkiewicz E., 1989, in *Big Bang, Active Galactic Nuclei and Supernovae*, eds. Hayakawa S. and Sato K., Universal Academic Press, Tokyo
2. Abramowicz, M.A. and Piran, T. 1980, *Ap. J. Lett.*, **247**, L7
3. Abramowicz, M., Bao, G., Lanza, A., Zhang, X-H., 1989 in *Proceedings of the 23rd ESLAB symposium*, eds. Hunt, J. and Battrick, B.
4. Abramowicz, M., Bao, G., Lanza, A., Zhang, X-H., 1991, *Astron. Astrophys.*,**245**, 454
5. Abramowicz, M., Calvani, M., Nobili, L. 1980, *Ap. J* **242**,772
6. Abramowicz M.A., Lanza A., Spiegel E.A., and Szuszkiewicz 1991c, *Nature*, **356**, 41
7. Abramowicz, M., Bao, G., Fiore, F., Lanza, A., Massaro, E., Perola, G. C., Spiegel, E. A., Szuszkiewicz, E. 1991a, *Proceedings of Heidelberg Conference On Active Galactic Nuclei*, (will be published by Springer)
8. Abramowicz, M., Bao, G., Fiore, F., Lanza, A., Massaro, E., Perola, G. C., Spiegel, E. A., Szuszkiewicz, E. 1991b, *Nature*, (submitted)
9. Alloin D. et al., 1986, *Ap. J*, **308**, 23
10. Antipov, S.V., Nezlin E.N., Snezhkin E.N. and Trubnikov A.S. 1986, *Nature*, **323**, 238

11. Asaoka I. 1989,*Publ. Astron. Soc. Japan* ,**41**, 763

12. Awaki, H., Koyama, K., Inoue, H., Halpern, J. P. 1991, *Publ. Astron. Soc. Japan*, **43**, 195

13. Bao, G. 1992, *Astron. Astrophys.*, **257**, 594

14. Bao, G. 1991,*Proceedings of Heidelberg Conference On Active Galactic Nuclei*, (will be published by Springer),

15. Bao, G. and Stuchlik, Z., 1991a, *Ap. J*, (in press)

16. Bao, G. and Stuchlik, Z., 1991b, in preparation

17. Barr P., Clavel J., Giommi P., Mushotzky R.F., Madejeski G., 1986, in *Variability of Galactic and Extragalactic X-ray Sources*, ed. Treves A. Milano

18. Barr P., Mushotzky R. F., 1986, *Nature*

19. Bassani, L., Dean, A. J., and Sembay. S., 1983, *Astron. Astrophys*, **125**, 52

20. Bardeen J.M. and Petterson J.A. 1975, *Ap. J.*, **195**, L65

21. Bath G.T., Evans W.D. and Papaloizou J. 1974, *Mon. Not. Roy. astr. Soc.*, **167**, 7p

22. Begelman M., 1990, in *Variability of Active Galactic Nuclei* eds. H.R. Miller, P.j. Witta

23. Bendat J.S., Piersol A.G., 1971, *Random Data*, Wiley, New York, Chap.1

24. Bengtsson L. and Lighthill J. (eds.) 1982, *Intense Atmospheric Vortices*, (Springer-Verlag, Berlin)

25. Bicak, J., Stuchlik, Z., Balek, V., 1989, Bull. Astron. Inst. Czechoslov., **40**, 65

26. Blandford R.D., 1985 in *Active Galactic Nuclei*, ed. Dyson J.E., Manchester University Press

27. Branduardi-Raymont, G. 1988, in *IAU Symposium 134, Active Galactic Nuclei*, eds. D. O. Osterbrock and J. S. Miller (Dordrecht: Kluwer), P. 177

28. Burbidge G.R., Burbidge E.M., Sandage A., 1963, *Rev. Mod. Phys.*, **35**, 947

29. Casinelli J.P. 1985, in *The Origin of Nonradiative Heating in Hot Stars*, eds. A.B. Underhill and A.G. Michilitsianos, NASA, 2358, 3

30. Cavallo G. and Rees M.J., 1978, *Mon. Not. A. Astr. Soc.*, **183**, 359

31. Clavel, J. et al., 1991, *Ap. J.*, **366**, 64

32. Clavel, J. et al., 1992, *Ap. J.*, (in press)

33. Cooke, B. A. et al., 1978, *Mon. Not. R. astr. Soc. 128*, 439,

34. Chandrasekhar, S. 1960, *Radiation Transfer*, (NY: Dover)

35. Chakrabarti S.K., Wiita P.J., 1991, *ICTP Preprint*, **IC/90-476**

36. Chen, K., Halpern, J. P., Filippenko, A. V. 1989, *Ap. J*,**339**, 742

37. Cunningham, C. T., and Bardeen J.M. 1973, *Ap. J*, **183**, 237

48. Day c. B. R., Fabian, A. C., George, I. M., Kunieda, H., 1990 *MNRAS*, **247** 15p

39. De Korte, P. A. J., Bleeker, J. A. M., den Boggende, A. J. F., Branduardi-Raymont, G., Brinkman, A. C., Culhane, J. L., Gronenschild, E. H. B. M., Mason, I, Mckechnie, S. P., 1981, *Space Sci. Rev.*,**30**, 495

40. Done, C., Koyama, K., Kunieda, H., Madejski, G., Mushotzky, and Turner, T. J. 1990 in IAU Colloquium No. 129 *Structure and Emission properties of accretion discs*, Paris, France

41. Done C., Koyama K., Kunieda H., Madejski G., Mushotzky R., and Turner T.J. 1990, in *Contributions to the 28th Yamada Conference on Frontiers of X-Ray Astronomy*, Nagoya

42. Done et al 1991, preprint

43. Done C. 1991, in *Proceedings of the Maryland Conference, Testing the AGN Paradigm*, College Park, MD

44. Dowling T.E. and Spiegel E.A. 1990, in *Nonlinear Astrophysics*, eds. R. Buchler and S. Gottesman, *N.Y. Acad. Sci.*, **617**, 190

45. Edelson, R. A., Krolik. J. H., 1988, *Ap. J*, **333**, 646

46. Edelson, R. A., and Malkan, M. A., 1986, **Ap. J.**, **308**, 59

47. Elliot, J. L., Shapiro, S. L., 1974, *Ap. J.*, **192**, L3

58. Fabian A. C., 1979, *Proc. Roy. Soc.*, **366**, 499

49. Fabian, A. C., Rees, M., Stella, L., White, N. E. 1989,*MNRAS*, **238**, 729

50. Fabian, A. C., George, I. M., 1990 in *Iron Line Diagnostics in X-ray Sources*, p169, eds. Treves, A., Perola, G. C., Stella, L.

51. Fiore F., Massaro E., Perola G.C., Piro L., 1989, *Ap. J*, **347**, 171

52. Fiore F., Massaro E., and Barone P. 1991a, *Astron. & Astrophys.*, submitted

53. Fiore F., Massaro E., and Barone P. 1991b, *Proceedings of the Heidelberg 1991 Conference on Physics of Active Galactic Nuclei*

54. George, I. M., Fabian, A. C., 1991, *MNRAS*, **249**, 352

55. Gies D.R., Bolton C.T., 1986, *Ap. J*, **304**, 371

56. Grobner, W. and Hofreiter, N., 1975, *Integraltafel, erster teil, Unbestimmte Integrale*, Springer Verlag, Wien-New York

57. George, I. M., Fabian, A. C., 1991, *Mon. Not. R. astr. Soc*, **249**, 352

58. George, I. M., Nandra, K., Fabian, A. C., 1990, *MNRAS*, **242**, 28

59. Hawley, J., 1987, *MNRAS*, **225**, 677

60. Heckman, T. M., Balick, B. and Sullivan, W. T. III 1978, *Ap. J.*, **224**, 745

61. Hills. J. G., 1975, *Nature*, **254**, 295

62. Honma, F., Matsumoto, R., Kato, S., 1992, preprint

63. Hopfinger E.J. and Browand F.K. 1982, *Nature*, **295**, 393

64. Ingersoll, A.P. 1990, *Science*, **248**, 308

65. Jaroszynski, M., Abramowicz, M. and Paczynski, B. 1980, *Acta Astron.*, **30**, 1

66. Kaastra J. S., and Barr, P., 1989, *Astron. Astrophys.*, **226**, 59

67. Karas, V., Bao, G., 1992, *Astron. Astrophys.*, **257**, 531

68. Kato, S., 1989, *Publ. Astron. Soc. Japan*, **41**, 745

69. Kato, S., 1990, *Publ. Astron. Soc. Japan*, **42**, 99

70. Kojima, Y. 1991,*Mon. Not. R. astr. Soc.*, **250**, 629

71. Kozlowski, M.,Jaroszynski, M. and Abramowicz, M. 1978, *Astron. Astrophys.*, **63**, 209

72. Kunieda, H., Turner, T. J., Awaki, H., Koyama, K. Mushotzky, R., and Tsusaka, Y., 1990, *Nature*, **345**, 786

73. Landau L.D. and Lifshitz E.M. 1975, *The Classical Theory of Fields*, (Pergamon Press, Oxford)

74. Laor, A. 1991, *Ap. J*, **376**, 90

75. Lawrence, A., Pounds, K. A., Watson, M. G. and Elvis, M. S., 1985. *Mon. Not. R. astr. Soc.*, **217**, 685

76. Lawrence, A., Watson, M. G. Pounds, K. A., and Elvis, M. S., 1987. *Nature*, **325**, 694

77. Lawrence A, 1986 in *Variability of Galactic and Extragalactic X-ray Sources*, ed. Treves A., Milano

78. Lehto H., 1990, in *Variability of Active Galactic Nuclei*, eds. H.R. Miller and P.J. Wiita

79. Lightman A.P., 1974, *Ap. J* **194**, 419 and 429

80. Lightman A.P., Eardley D.M., 1974, *Ap. J*, **187**, L1-L3

81. Marshall, F. E., Holt, S. S., Mushotzky, R. F., Becker, R. H., 1983, *Ap. J*, **269**, 131

82. Matt. G., Perola, G. C., Piro, L, 1991 *Astron. Astrophys.* **247**, 25

83. Makishima K., 1988, in *Physics of Neutron Stars and Black Holes*, ed. Y. Tanaka, University Academy Press, Tokyo, 175

84. Marshall N., Warwick R.S., Pounds K.A., 1981, *Mon. Not. R. Astr. Soc.*, **194**, 987

85. Maraschi and Molendi, 1991 *Ap. J*

86. McHardy I.M., 1985, *Space Science Reviews*, **40**, 559

87. McHardy I.M. and Czerny B., 1987, *Nature*, **325**, 696

88. McHardy I., 1989, in *Proceedings of the 23rd ESLAB Symposium*, eds. J.Hunt, B. Battrick, European Space Agency, The Netherlands, 1111

89. Mason, K. O. 1989, in *Proceedings of the 23rd ESLAB Symposium*, p. 113, eds. Hunt, J., and Battrick, B.

90. Milgrom, M. 1978, *Astron. Astrophys.*,**208**, 191

91. Misner, C.W., Thorne, K.S., and Wheeler, J.A. 1973, *Gravitation*, W.H. Freeman, San Francisco,

92. Mittaz, J. P. D., and Branduardi-Raymont, G. 1989, *Mon. Not. astr. Soc*, **238**, 1029

93. Mushotzky, R. F. et al, 1980, *AP. J*, **235**, 377

94. Nandra, K., Pounds, K. A., Stewart, G. C., 1990 in *Conf. on Iron Line Diagnostics in X-ray Sources (Varenna)* , p177, eds. Treves, A., Perola, G. C., Stella, L. (Berlin: Springer- Verlag)

95. Nandra K. et al, 1991, *Mon. Not. R. astr. Soc.*, 1991, **248**, 760

96. Nandra, K., Pounds, K. A., Stewart, G. C., Fabian, A. C., Rees, M. J., 1989, *Mon. Not. R. astr. Soc.*, **236**, 39P

97. Nolan P.L., Gruber D.E., Matterson J.L., Peterson L.E., Rothschild R.E., Doty J.P., Levine A.M., Lewin W.H.G., Primini F.A., 1981, *Ap. J*, **246**, 494

98. Paczynski, B., Wiita, P. 1980, *Astron. Astrophys.*, **88**, 23

99. Parmar, A. N. and White, N. E. 1988 in *X-ray Astronomy with EXOSAT*, P. 147 eds. Pallavicini, R. and White, N. E.

100. Perola G.C.et al., 1986, *Ap. J*, **306**, 508

101. Phinney, E. S. 1983, Ph. D. thesis, Cambridge University

102. Pounds K.A., McHardy I., 1988, in *Physics of Neutron Stars and Black Holes*, ed. Tanaka, University Academy Press, Tokyo, 285

103. Pounds, K. A., Nandra, K., Stewart, G. C., George, I. M., Leighly, K., 1989, *Mon. Not. R. astr. Soc.*, **240**, 769

104. Pounds, K. A., Nandra, K., Stewart, G. C., George, I. M., Fabian, A. C., 1990, *Nature*, **344**, 132

105. Pounds K.A. and Turner T.J., 1986, in *Variability of Galactic and Extragalactic X-ray Sources*, ed. Treves A., Milano

106. Pounds K. A., Turner T. J., Warwick R. S., 1986,*Mon. Not. R. astr. Soc.*, **221**, 7p

107. Pringle J.E., 1981, *ARA & A*, **19**, 137

108. Pringle J.E., Rees M.J., Pacholczyk A.G., 1973, *A & A*, **29**, 179

109. Rees M.J., 1984, *ARA & A*, **22**, 471

110. Rice S.O.,1954, in *Noise and Stochastic Processes*,ed. Wax, N. ( Dover, London)

111. Rothschild, R. E. et al., 1979, In *X-ray astronomy*, Pergamom oxford,

112. Roberto G.A., McHardy I.M., 1989, in *Proceedings of the 23rd ESLAB Symposium*, eds. Hunt J. and Battrick B., ESA Publication Division, ESTEC, Nordwijk, the Netherlands

113. Robinson I., Schild A., Schucking E. (eds), 1964, in *Proceedings of Tex Conf. Relative Astrophys., 1st.*, Chicago University Press

114. Sekiguchi K. and Menzies J.W. 1990, *Mon. Not. Roy. astr. Soc.*, **245**, 66

115. Shakura N.I., Sunyaev R.A., 1973, *A & A*, **24**, 337

116. Shakura N.I., Sunyaev R.A., 1976, *Mon. Not. R. astr. Soc.*, **175**, 613

117. Sommeria J., Meyers S.D. and Swinney H.L. 1988, *Nature* **331**, 689

118. Stella, L., and Angelini, L., 1991, Milan preprint series in Astrophysics N. 91

119. Stella, L., Compana, S. 1991, in *Conf. on Iron Line Diagnostics in X-ray Sources (Varenna)*, ed. A. Treves (Berlin: Springer- Verlag)

120. Stuchlik, Z., Bao, G., 1992, *G. R. G.*, (in press)

121. Sulentic, J. W., Calvani, M., Marziani, P., Zheng, W.1990,*Ap. J* , **355**, L15

122. Sunyaev R.A., 1973, *Sov.Astron. AJ*, **16**, 941

123. Syer D., Clarke C.J., and Rees M.J. 1991, *Mon. Not. Roy. astr. Soc.*, **205**, 505

124. Szuszkiewicz, E., 1989, Ph. D thesis, SISSA

125. Szuszkiewicz, E., 1991, private communications

126. Tagliaferri, G., Stella, L., Maraschi, L., Treves, A., Gelotti, A,,1991, *Ap. J*, **380**, 78

127. Tennant A., Mushotzky R.F., Boldt E., Swank J., 1981 *Ap. J*, **264**, 92

128. Tennant A., Mushotzky R.F., 1983, *Ap. J*, **264**, 92

129. Tennant, A. F., Mushotzky, R. F., Boldt, E. A., Swank, J. H., 1981, *Ap. J*, **251**, 15

130. Tannanbaum, H. et al., 1978, *Ap. J*, **223**, 74

131. Taylor, B. G. et al.,1988, *Space Science Rev.*, **240**, 833

132. Turner, T. J., and Pounds, K., 1989, *Mon. Not. R. astr. Soc., 204*, 833

133. Treves, A., Maraschi, L., Abramowicz, M., 1988, *PASP*, **100**, 427

134. Treves, A. (ed), 1987, *Variability of Galactic and Extragalactic X-Ray Sources*, Associazione per l'Avanzamento dell'Astronomia, Milano-Bologna

135. Tuominen I., Moss D., and Rüdriger G. (eds) 1991, *The Sun and Cool Stars, Activity, Magnetism, Dynamos*, (Springer-Verlag, Berlin)

136. Wandel, A., Liang, E. P. 1991, *Ap. J*, (in press)

137. Walter, R., Courvoisier, T. J.-L., *Astron. Astrophys.*, **246**, 494

138. Walinder F. H. 1991, *MNRAS*, **253**, 184

139. Walinder F. H., Kato, S., Abramowicz, M., 1992, submitted to *Astron. Astrophys.*

140. Walter, R. Courvoisier, T. J.-L., 1990 *Astron. Astrophys.* , **246**, 494

141. White, N. E., Peacock, A., Hasinger, G., Mason, K. O., Manson, K. O., Manzo, G., Taylor, B. G., Branduardi–Raymont, G., 1986, *Mon. Not. R. astr. Soc.*, **218**, 129

142. White, N. E., Peacock, A.,1988, in *X-ray Astronomy with EXOSAT*, eds. Pallavicini, R., White, N. E., p. 7

143. Wilson, A. S., Ulvestad, J. S., 1982, *Ap. J.*,**260**, 56

144. Wiita P.J., Miller H.R., Carini M.T., Rosen A., 1990, in *IAU Colloquium 129, Structure and Emissio Properties of Accretion Disks*, eds. J.P. Lasota et al. (in press)

145. Wiita, P. J., Miller, H. R., 1990, preprint

146. Wiita, P. J., Miller, H. R., 1990, *Comments Astrophys.* **15**, 41

147. Wilson A.S., Ward M.J., Ayon D.J., Elvis M., Meurs E.J.A., 1979, *MNSAS*, **187**, 109

148. Wilson A.S., 1991, *Proceedings of the Heidelberg 1991 Conference on Physics of Active Galactic Nuclei*

149. Zhang, X-H., Bao, G., 1991, *Astron. Astrophys.*, **246**, 21